NTNU

Norwegian University of
Science and Technology

Seismic Inversion for Identification of Soil Stiffness and Damping for Offshore Wind Turbines

Michael Andrew Armstrong

Wind Energy
Submission date: August 2016
Supervisor: Torgeir Moan, IMT
Co-supervisor: Andrei Metrikine, TU Delft, CiTG
Gudmund Eiksund, BAT
Pim Versteijlen, Siemens Wind Power Nederland

Norwegian University of Science and Technology
Department of Marine Technology

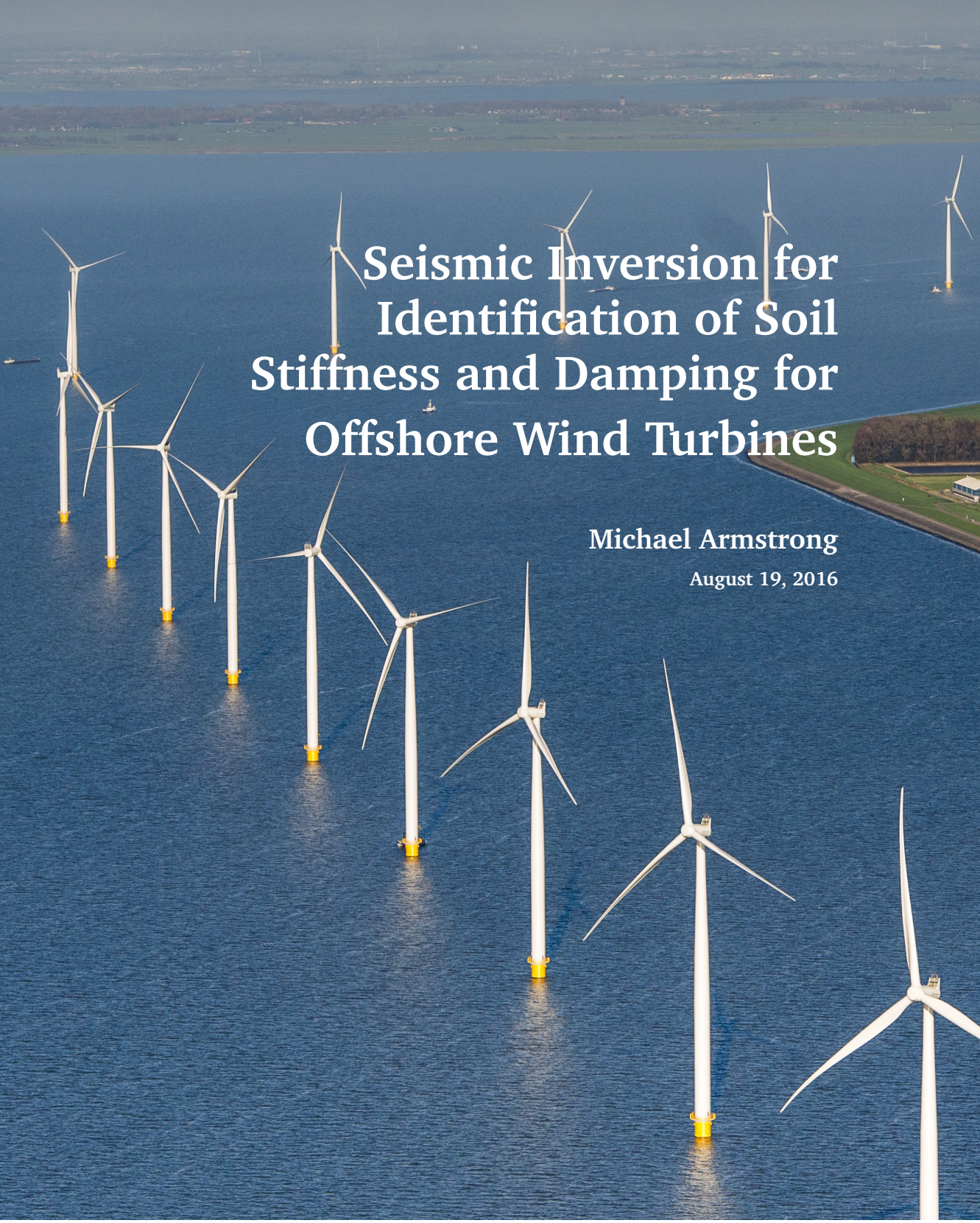

Seismic Inversion for Identification of Soil Stiffness and Damping for Offshore Wind Turbines

Michael Armstrong

August 19, 2016

TU Delft Delft University of Technology

SIEMENS

NTNU

Seismic Inversion for Identification of Near-Surface Soil Properties for Offshore Wind Turbines

Master of Science Thesis

Author:	Michael Armstrong	
Committee:	Ir. W.G. Versteijlen	TU Delft, Siemens Wind Power
	Dr. Ir. K.N. van Dalen	TU Delft
	Prof. Dr. A.V. Metrikine	TU Delft - Chairman
	Dr. Ir. D. J. Verschuur	TU Delft
	Prof. Dr. G.R. Eiksund	NTNU

August 19, 2016

- CONFIDENTIAL -

Summary

Non-invasive in-situ measurements can determine the soil properties in an undisturbed way, providing a more accurate characterization of the soil stiffness and damping. This report focuses on the multichannel analysis of surface waves (MASW) technique. The measured dispersion of a propagating seismic wave is used to characterize the variation of small-strain soil stiffness with depth while a modified half-bandwidth method is used to estimate the intrinsic soil damping variation with depth. Both require solving an inversion problem with a global optimization strategy.

The equations governing wave propagation in layered visco-elastic media are used to form a analytic forward model. Sensitivity studies are performed and it is found that for a soil damping ratio below 10%, the migration of the real part of the wavenumber is minor. Therefore, a decoupled approach is used, where the soil stiffness is estimated first, followed by an estimation of the soil damping. The modal dispersion curves are shown to be very sensitive to the shear wave velocity of the soil, especially in the near surface layers. This is desirable as this sensitivity allows for a more accurate inversion. Additionally, there is a high sensitivity to the layer thickness of the model and it is shown that the discretization of the model, especially near the surface, has a large impact on the predicted modal dispersion curves.

To estimate the stiffness profile, modal inversion is performed with a genetic algorithm. The misfit function is based on the determinant of the secular function, including a determinant normalization. Synthetic inversions were first applied to verify that the technique is successful. Surface wave data from the Westermeerwind offshore wind farm is analyzed and several estimates are made for the stiffness profile versus depth using different inversion settings. It is shown that these estimates agree well with a seismic cone penetration test (SCPT) estimate for the same site. An inversion is also performed on a set of measurements taken at the North-Sea Gjøa site. It is shown that the inversion is in good agreement with the published predictions for the stiffness at this site.

The damping profile is inverted based on a modified half-power bandwidth method. A wavelet compression is used to select a smart set of root locations which leads to an efficient and balanced inversion. Synthetic inversions show that the method is successful in estimating the soil damping profile. The damping inversion technique is very promising and the next step should be taken to apply this to the measured data from the Gjøa and IJsselmeer sites.

Acknowledgements

If I have seen further, it is by standing on the shoulders of giants. **-Isaac Newton**

First, thanks Mom and Dad, for always believing in me and giving me the mindset and confidence to attack challenging problems. Pim, you promised me a challenging but rewarding project and this project has surely exceeded my initial expectations on both regards. Thank you for your steadfast availability and the help you gave every step of the way. To Karel, thank you for the many meetings we had to discuss the challenges, the direction to take and the numerous discussions on visco-elastic wave propagation theory. It was incredibly helpful to be able to not only understand the theory, but then to bring it back to a physical understanding. Eric, thank you for the helpful meetings and discussions, especially with regards to processing the data and performing the Radon transformation. Andrei, thank you for making time and being able to dig straight to the critical points to help me set the right direction. Gudmund, thanks for being so flexible and understanding with my project and supervising me from long distance.

To my colleagues at Siemens wind power, thank you for providing a welcoming, intellectual and fun environment which surely helped my inspiration on a daily basis. To Corine and Ingmar, thank you for your hard work, building the foundation from which I could continue.

Finally, thanks to the DISSTINCT team, for giving me the opportunity to work with the data from the IJsselmeer. To Maarten Vanneste and NGI, many thanks for being so open and allowing me to work on the Gjøa data.

Michael Armstrong
Delft, August 2016

Contents

Nomenclature

Latin symbols

c	Velocity	ms^{-1}
C_p	Pressure or P-wave velocity	ms^{-1}
C_s	Shear or S-wave velocity	ms^{-1}
E	Elastic modulus	Nm^2
f	Frequency	Hz
$\bar{f}_{ext}$	External source vector (in wave equation)	N
k	Wavenumber	$radm^{-1}$
k	Wavenumber (shown in plots)	m^{-1}
M	Coefficient matrix	
Q	Quality factor	
u	Displacement	m
x	Scalar x	
$\bar{x}$	Vector x	
x_{ij}	Matrix X component ij	
$x_{i,j}$	Vector x compoent i, derivative wrt j	
$\tilde{x}$	x transformed with Fourier transform	
x^{H_0}	x transformed with Hankel transform	

Greek symbols

ϵ	Strain
ζ	Material damping
γ	Shear Strain

λ	Lamé's first constant	Nm^{-2}
λ	Wavelength	m
μ	Shear modulus, Lamé's second constant	Nm^{-2}
ρ	Density	kgm^{-3}
ρ_l	Water density	kgm^{-3}
σ	Stress	Nm^{-2}
ν	Poisson ratio	
ϕ	Elastic dilational potential	m^2s^{-1}
ψ	Elastic rotational potential	m^2s^{-1}
ω	Circular frequency	$rads^{-1}$
τ	Shear stress	Nm^{-2}

Abbreviations

CG	Conjugate gradient minimization
CPT	Cone penetration test
FW	Full waveform method
LCOE	Levelised Cost of Energy
MASW	Multi-channel analysis of surface waves
MSW	Modal surface wave method
SCPT	Seismic cone penetration test
p-wave	Pressure wave
s-wave	Shear wave
SH	Shear horizontally polarized
SV	Shear vertically polarized
SSI	Soil Structure Interaction
thk_j	Thickness of layer j
pFM	Probability of full mutation
pSM	Probability of small mutation
N_{gen}	Number of generations in genetic inversion
N_{Pop}	Number of candidates in genetic population
N_{Dad}	Number of parents in genetic population
N_{Con}	Number of contestants in genetic population

Chapter 1

Introduction

1.1 Background

Improved understanding and modelling of soil-structure interaction could lead to a 7.5% [7] to 33% [22] reduction in the cost of the support structure in coming years. The TKI Wind Op Zee consortium has predicted a 40% decrease in the cost of offshore wind from 2010 to 2020 [7]. Efficient design by improved modelling would directly contribute to 1.1% levelized cost of energy (LCOE) reduction while partially contributing to another 4.9% and possibly more if the effect of risk reduction by improved modelling is considered. Regardless of the exact amount of potential savings, research in soil-structure interaction (SSI) will contribute to LCOE reduction. The current API methods for determining soil properties are heavily empirical, and soil properties are determined from limited simple parameters. Hence, a key factor in improving the SSI based design methods will be to have an accurate estimate of the soil characteristics. The small-strain stiffness is essential as it is important for the eigenfrequency, dynamic loading and fatigue lifetime. Current methods of cone penetration testing (CPT) and borehole sampling are testing failure at large strains or are likely to disturb the sample.

This research focuses on one possible avenue which may contribute to a reduction in LCOE. Multi-channel analysis of surface waves (MASW) is a promising technique to enlighten soil characteristics, a key component for accurate SSI modelling which is one of the most uncertain areas of offshore wind turbine design. Measurements of propagating seismic waves will be analysed to estimate the stiffness and damping properties of the soil. This is a direct non-invasive measurement and

also has the advantage that it is not related to a point sample but rather seismic investigation will average over the measurement area.

The overall goal of the thesis is to demonstrate effective methods to determine the soil stiffness and damping profiles in the $0 - 50m$ range, which is of interest for the design of offshore wind turbines. This MSc thesis builds on two previous MSc theses [34] and [4] and aims to overcome the issues encountered therein.

1.2 Measurement Techniques

The section on Measurement Techniques is largely based on Chapter 6 of the Geotechnical Earthquake Engineering texbook by S. Kramer [13]

There are many different ways in which the dynamic soil properties can be measured, each with its own set of advantages and disadvantages. These measurement techniques may be broadly separated into small strain or large strain measurements and may occur in the field, in situ, or in the laboratory. Soil exhibits nonlinear behaviour with respect to strain level and it is important to determine the dynamic soil properties in a way which is representative of the real loading conditions and the engineering model chosen. "*The stiffness and damping characteristics of cyclically loaded soils are critical to the evaluation of many geotechnical earthquake engineering problems.*"[13]. Other properties such as Poisson's Ratio and density tend to fall within a relatively narrow range and therefore have less influence on the solution.

For offshore wind turbines, small and large strain properties may be of interest depending on the load that is considered. Ultimate limit state loadcases may develop large strains which could be modelled with secant stiffness while fatigue driven designs may be more concerned with having accurate small strain or nonlinear stiffness especially to correctly predict the amplitude of stress cycles over the entire lifetime. Stated another way, the large strain stiffness are lower and if one secant stiffness is used for models, then the small strain cycles could be predicted by a softer response than actually occurs with a more realistic non-linear stiffness. The industry trend is towards larger turbines which are more often design driven by fatigue limit states. Hence, it is increasingly important to predict lifetime responses and fatigue with high accuracy.

1.2.1 Laboratory Testing

Only a brief overview of lab tests are given since this is beyond the scope of this project. Borehole sampling is used to retrieve samples which are tested in the lab.

This can produce accurate results with high certainty properties. However, some disadvantages include:

- Costly to conduct
- Process of sampling disturbs soil
- Samples are obtained at a point and spatial variability can only be estimated with sampling at many locations, which would be very costly

Low strain tests are usually below 0.001% strain and the properties are assumed to be linear elastic in this range. Low strain tests include the Resonant Column Test, Pulse test and Piezo Bender Element test which all aim to determine the wave propagation velocities through different means. High strain tests include cyclic triaxial test and cyclic direct simple shear test. It could be very useful to compare the stiffness and damping properties obtained by seismic inversion approach to those obtained by laboratory tests on samples from the same site if a suitable location is found.

1.2.2 Seismic Reflection Test

This is perhaps conceptually the simplest seismic wave test. A source and receiver placed a known distance apart on the seabed is required. Direct and reflected arrival times are measured for the P-waves and S-waves. The created seismic wave will travel until it reaches an abrupt change in impedance, where a portion of the energy will be reflected back to the surface. This method usually focuses on the P-wave reflections, using a source which is rich in P-wave content. It is more suitable for large scale or deep stratigraphy and not for determining properties of shallow layers. Sloping layers can makes this technique more difficult in practise and location correction or migration of reflection data must be performed. Furthermore, for smaller distances or shallower layers the reflected wave may arrive while the direct wave is still being measured and this makes it difficult to separate.

1.2.3 Seismic Refraction Test

This is similar to the seismic reflection test but uses the first wave arrival time. As the source-receiver distance increases, the waves that are detected first will transition from direct waves to reflected waves, which have travelled through deeper faster layers. This is seen as changes of slope on the distance-time arrival diagram. It only works for soil deposits where the stiffness or wave speed is increasing with depth and would not be useable when soft layers underlie a stiffer layer. For sloping layers

there is the issue of apparent velocities differing from the true velocity and a dip angle must be determined by reverse profiling. Modern techniques extend this test to create a tomographic profile of the soil.

1.2.4 Suspension Logging Test

A probe which contains a source at the tip and two geophone receivers near the top is inserted into a borehole. An impulse pressure wave is generated which travels through the drilling fluid and creates an S-wave and P-wave which runs up the bore hole walls. The velocity of the wave can be accurately determined by the two geophones over a small and precisely located distance. The polarity can be reversed to distinguish P and S waves. Uncertainties may arise due interaction between the wave, walls and drill fluid and difficulty defining the actual motion of the wave travelling in the soil as it may be a surface wave similar to a Rayleigh wave, which has a different and slower speed than corresponding P or S waves.

1.2.5 Cone Penetration Tests

Cone penetration testing (CPT) is one of the most commonly used methods to determine soil properties in the field. The test is simple to conduct and is performed rapidly and relatively inexpensively. However, the tip resistance versus depth data must be interpreted into the properties of interest which in practise means that empirical relations to the tip resistance are used. This method is not sufficiently accurate to determine dynamic soil properties, although it remains very useful to determine the layering and density of the soil. Additional sensors are increasingly added to gather more data, which will be discussed later on.

1.2.6 Seismic Cone Penetration Test

The seismic cone penetration test (SCPT) adds a geophone receiver to the standard CPT probe. The CPT test is stopped while a source at the surface produces an impulse seismic wave. This measures the almost vertical propagation of the waves in the soil. There is some refraction due to the horizontal offset, which must be accounted for. This method has been used to demonstrate that stiffness parameters varying with depth can be determined and that when used in a 3D FEM model that there are significant differences from the design approach specified by the standards [30]. The author shows that for a variety of assumptions about the variation of the soil type that the deflections calculated from the FEM method are lower than the design

code approach and that the FEM results can be translated into an equivalent 1D stiffness model [31].

1.2.7 Cross and Down hole tests

Cross hole seismic tests requires multiple boreholes and measures the time taken for a source impulse to travel along a horizontal level to the receivers in the other boreholes. This directly measures the speed along a layer. However, it can be difficult to coordinate the advancement of the probes in all the boreholes at the same rate. Additionally, there is some uncertainty about the transfer function between the sensors in the boreholes and the waves.

Down hole or up hole measurements only require one borehole and use a source close to the borehole but on the seabed surface. The receiver is in the probe tip for downhole configuration, which is very similar to the SCPT test, except that it takes place in a borehole. An additional disadvantage is that there is uncertainty in the transfer function between the body wave and the sensor due to the interaction at the wall and with the drill fluid.

1.2.8 Spectral Analysis of Surface Waves

A source creates an impulse seismic wave that travels through the water as an acoustic wave and through the soil as a P, S, Rayleigh (or Scholte) and Love waves. The response is measured by a geophone or an array of geophones on the seabed. With an array this test is called a Multi-channel Analysis of Surface Waves (MASW) test. The recorded sensor readings, which are in the space-time domain, can be converted into a dispersion diagram, which is in phase velocity-frequency or wavenumber-frequency domains. The dispersive character of the site is related to the variation of the elastic body wave velocities with depth. This test is a recent development with researchers pioneering it in the 1980s and early 1990s [13]. The author of Geotechnical Earthquake Engineering calls it *"one of the most significant recent advances in shallow seismic exploration."* In principle, the soil stiffness and damping vs depth can be determined from the MASW measurements. However, this process is not as straight-forward as other methods and requires an inversion process to determine what the most likely soil properties are. Due to the possibility of complex layering with stiffness inversions, the solution of the inversion problem may have many local minima and a global search technique must be used. The MASW method is the dynamic soil property identification method which this research project aims to demonstrate is viable.

1.3 Review of Previous Work

1.3.1 First MSc at Siemens Wind Power

C. E. de Winter [34] established the theoretical basis for the modelling propagating soil waves in continuum. She made some studies to choose the measurement set up and compared different methods for the forward modelling approach. She used finite difference modelling to compare various source-receiver combinations including active or passive sources and vertical or horizontal receiver arrays. Practically vertical arrays are hard to re-locate and also horizontal arrays are able to measure geometric dispersion which is sensitive to the subsurface stratification. The use of an active source is preferred since signature and timing of the source is known. It is possible to use a passive source if a source independent objective function can be formulated, as demonstrated [4]. Finite difference, modal surface wave (MSW) method and full waveform (FW) methods are compared and it was recommended to use full-waveform modelling due to the possibility for automatizing the entire process. The modal inversion method typically requires an experienced geophysical engineer in order to ensure that the correct modal curves are chosen. The finite difference method is not guaranteed to match the analytic models, due to discretization. Hence, the analytic methods were chosen. The modal surface wave method requires a small wavenumber stepsize of $0.00024m^{-1}$ to avoid the calculation 'missing' modes.

Both the modal surface wave and full waveform inversion methods were developed and tested. The modal surface wave method uses an objective function that is related to the distance between the theoretical dispersion curves and the measured dispersion curves. While the full waveform inversion compares the correlation of the theoretical and measured 2D f-k spectra. The inversion method is then an optimization problem to minimize this error/objective function, or maximize the suitability of a candidate soil profile. The global optimization strategy of using a genetic algorithm is chosen for the inversion process since the problem is non-linear and expected to have many local minima. The conjugate gradient scheme can be included in a hybrid approach to refine the final candidate to the best solution. Corine verifies that the genetic algorithm is able to determine the soil profile with good accuracy for a synthetic case. Also, the effect of incorrect a-priori knowledge is tested, since the inversion only determines the shear stiffness and assumes that the layer density, thickness and P-wave velocity are already known. It shows that errors in the assumed parameters do affect the ability of the inversion to find the correct shear wave velocity profile, but since only limited cases were tested, it is not possible to generalize the results. The shallow layers are seen to have a big impact on the dis-

persion used for the inversion and the algorithm is able to estimate these shallow layers with the highest certainty and smallest standard deviation. Shallow layers are felt by all waves, while deeper layers are only felt by low frequency long wavelength content. A 5% uncertainty in the properties seems to result in a maximum error of 12%in the best inversion result although most results have an error smaller than 5%. Corine then uses the finite difference model to generate synethic data, which is used for an inversion. The error is higher and the inversion is not as good as the algorithm is theoretically able to produce, but the profile and important contrasts are able to be successfully visualized.

1.3.2 Second MSc at Siemens Wind Power

I. Bolderink [4] built on the work of Corine and applied the full waveform inversion process to actual measured data from the IJsselmeer. In the theoretical part of his his work, the objective function is modified to make it source independent, although it is not entirely independent due to the need of a stabilization factor. The impact of space domain truncation was included into the full waveform inversion process by performing windowing on the theoretical model through an FFT algorithm which is faster than the convolution method. A synthetic inversion is performed for the pressure wave velocity and shows that the genetic algorithm can be used for determining the pressure wave velocity profile if the shear wave velocity profile and other parameters are already known. For the in-situ measurements, several measurement set-ups are considered for practial reasons and in the end a 48m array with a 1m sensor spacing is used. During the actual measurements, the position of the array is fixed, centred above the turbine location, while the source is moved in order to concatenate multiple datasets and create a virtual measurement array with a longer virtual length to improve resolution in the wavenumber domain. Due to some hardware damages, only the hydrophone data was useable. Also, the accuracy of the positioning system was low and so the shots had to be corrected for an angular error of approximately 15 degrees. The locations were aligned using the direct arrival time of the pressure wave in water. A sparse Radon transformation is used to clean up the data and remove noise as the measured data becomes constructed by linear and parabolic events. The dispersion record is improved by using RMS scaling on the data to increase the influence of the far-field data by scaling the amplitudes to the same RMS value at every spatial array location. The shot record is also windowed with a tukey window in order to reduce the visible sidelobing and increase the clarity of the energy distribution in the spectra. In the end, the visible response is in the range of 0-0.1 m^{-1} wavenumber and $0 - 30Hz$.

An initial estimate is made for the soil profile based on the interpretation of the

CPT measurements and the report by Fugro. A model with a water layer, 8 soil layers and a halfspace is used. The full waveform method initially resulted in an unsuccessful inversion with a very low suitability and poor match obtained. Allowing a larger search range and specifying a high halfspace velocity improved the suitability. However, the estimate was not considered to be reliable. In the end, the best match that could be obtained with the full waveform method was a suitability of 0.49 and a corresponding spectral response which visually has a quite low correlation with the measured response spectra. The effect of the damping profile is thought to have a large impact on the visibility in the response spectra, perhaps as important or more important even than the windowing effect of the limited length of the measurement array. Hence, a good estimate of the damping profile may be required as part of a successful full waveform inversion.

1.4 Problem Definition

The research objective of this thesis aims to answer two questions:

"*Can modal waveform inversion reliably estimate the soil stiffness profile from surface wave measurements? How can the soil damping profile be estimated from surface wave measurements?*"

Theoretically, the multi-channel analysis of surface waves can be used to retrieve the stiffness and damping properties of near surface layers. So far the research at Siemens has focused on estimation of the stiffness. However, a prediction of the soil damping would be of great value for the design of offshore wind turbines. Hence, this thesis would like to be able to estimate the damping. Typically, an accurate stiffness profile is required in order to estimate the material damping, and so this thesis will also focus on the stiffness inversion.

It is thought that the low success rate of the full waveform inversion is caused by the high dependency of the full waveform spectra on the damping. It is possible that a damping independent inversion method would be more successful. Therefore, this research will focus on using the modal waveform inversion method to first estimate the stiffness profile and then subsequently the damping profile may be estimated. Although the modal dispersion curves are not completely independent of the damping, we can assume that they are independent for relatively low amounts of damping. This is analogous to a single degree of freedom system where the resonant natural frequency differs from the undamped natural frequency. This decoupling assumption and the sensitivity of the modal dispersion curves to damping is discussed

later in Section 4.1.

The attenuation of the surface waves is due to both geometric and material damping. The soil damping we wish to estimate is the material damping. To separate the geometric damping from the total damping, an accurate stiffness profile is required. Hence, once the stiffness is estimated, then the analysis can be performed to assess the contribution of the material damping to the total attenuation of the surface waves. Different techniques exist for estimating the damping profile, and this thesis will have to develop a method which is appropriate for estimating the internal soil damping.

Chapter 2

Theory and Derivations

The derivations in this chapter have all been worked through by the author, but have existed for many years and can be found in many reference materials. The three reference materials [8], [34] and [1] were used as the main guides for the author.

In general, there are four important types of propagating waves which occur in soil systems considered to be linear elastic and isotropic [19] [13] [8]. There are two body waves, P-waves and S-waves, which occur far from boundaries. The P-wave also known as compressional or pressure wave is associated with longitudinal particle motion where the soil undergoes a local compression and elongation in the direction of travel as the wave passes. The S-wave or shear wave is associated with particle motion in the transverse direction to the direction of motion of the wave. This creates shear strain and shear stresses in the soil and hence the name. Any shear wave motion can be decomposed into the horizontal and vertically polarized components or SH and SV type waves. The figure 2.1 shows a visual representation of the P-wave and S-wave, while the figure 2.2 shows the SH and SV components.

There are two waves, Rayleigh and Love waves, which occur at a free surface of the soil. There is actually another wave type which occurs when there is a fluid-soil interface, the Scholte wave, although its characteristics and motions are similar to the Rayleigh wave and sometimes waves on the seabed are still referred to as Rayleigh waves. The Rayleigh wave is a combination of the SV and P-waves interacting at the surface. This creates and elliptical particle motion. It is called a surface wave because this type of behaviour can only occur at the surface and the amplitude of particle motions decay exponentially away from the surface. The Rayleigh or Scholte wave motion is different to the motion of water waves because the parti-

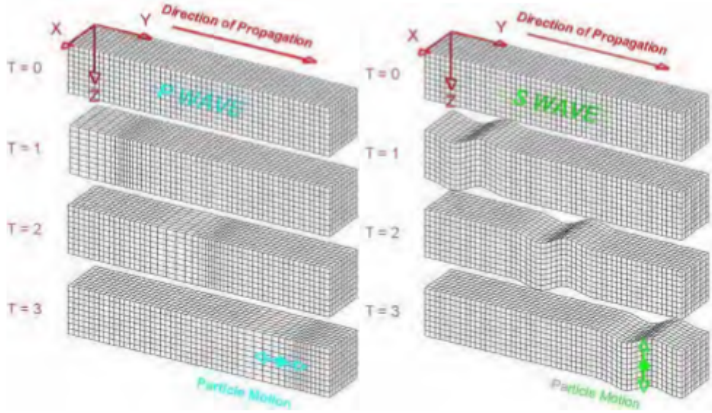

(a) Pressure wave (b) Shear wave

Figure 2.1: Particle motion in body waves.

Figure 2.2: Generic orthogonally polarized waves.

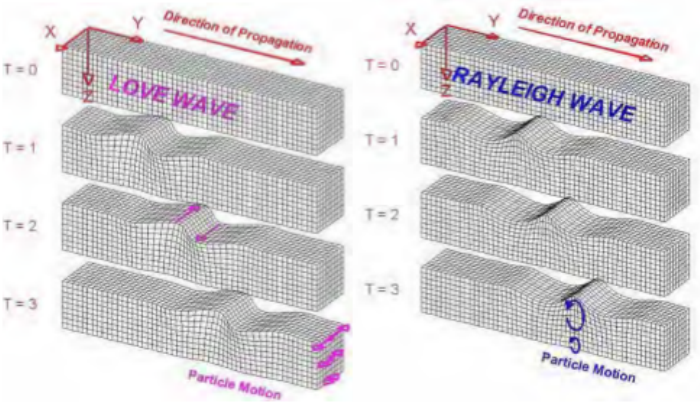

Figure 2.3: Particle motion in surface waves.

cle motion traces an ellipse in the opposite direction to what occurs in water waves. This retrograde motion is due to the shear stresses which cannot occur in water. The other wave is the Love wave which is a combination of the SH and P-waves and results in the ground moving side to side instead of up and down. The Love wave is not considered in this thesis, the motions are out of the 2D plane which is used to characterize the soil via the measurement array. It cannot be generated with an airgun source and must be generated by a hammer and beam or another source which imparts shear stress on the soil [19] [13]. A project by NGI in deep waters successfully used a custom made suction bucket source and actuator in order to generate source waves in a very controlled manner. This showed that it is possible to use mutltimodal Love and Scholte wave joint inversion to aid in the characterization of the site and it is advantageous to be able to use multiple wave types [29]. Figure 2.3 shows the particle motion for surface waves.

Since a surface array will be used to record measurements, it is expected that the Rayleigh waves will be the most visible and the most important in characterizing the soil. Rayleigh waves contain the most energy [19] and are dispersive in character in non-homogeneous media. Dispersion means that the wave speed is dependent on the wavelength. Figure 2.4 shows the decay of particle motion at a certain depth away from the surface. It can be normalized by the wavelength and after ~ 1.5 wavelengths the amplitude is quite small. Therefore, the longer wavelength waves will 'feel' deeper into the soil and their velocity is influenced by the stiffness of these

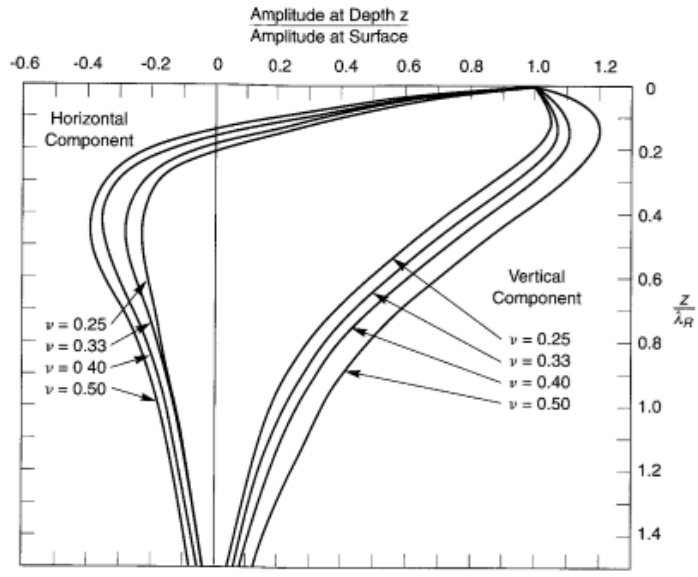

Figure 2.4: Variation of Rayleigh wave amplitude with depth [13].

deeper layers while short wavelength waves will have their speed governed by the shallower layers of soil. This is the principle that makes inversion possible.

In acoustic media, which cannot develop shear stresses since it has no shear stiffness, S-waves cannot exist. Therefore, only compressional or pressure type waves exist.

2.1 Elastic Wave Equation

It is assumed that soil can be modelled as a continuum with certain macroscopic properties and that we can formulate governing equations for soil systems based on classical physical laws, such as Newton's second law.

The derivation consists of combining 3 relations in 3 dimensions. In order to keep the derivation succinct the more compact Einstein index notation is used. The kinematic equation gives the relationship between strain and displacements. The constitutive equation gives the relationship between stress and strain. The equilibrium equation is formulated to satisfy Newton's 2nd Law between stresses and

accelerations.

2.1.1 Kinematic Equation

The deformation of a control volume is considered to determine the relationship between displacements and strains. If we consider the deformation of a control volume where u represents deformations:

$$\epsilon_{11} = \frac{\Delta u_1}{\Delta x_1} = \frac{du_1}{dx_1} = u_{1,1} \tag{2.1}$$

$$\epsilon_{12} = \frac{1}{2}(\frac{\Delta u_1}{\Delta x_2} + \frac{\Delta u_2}{\Delta x_1}) = \frac{1}{2}(\frac{du_1}{dx_2} + \frac{du_2}{dx_1}) = \frac{1}{2}(u_{1,2} + u_{2,1}) = \epsilon_{21} \tag{2.2}$$

In 3 dimensions all the strain components form a second order tensor. However, this tensor is symmetric and there are only 6 independent strain components, which we will make use of later. In index notation note that the "," is signifying the derivative with respect to the terms which come after it. The strains are then given by:

$$\epsilon_{ij} = \frac{1}{2}(u_{i,j} + u_{j,i}) \tag{2.3}$$

2.1.2 Constitutive Equation

In general the stiffness depends on the strain level. For example, Figure 2.5 shows how the shear stiffness varies with strain level. Seismic waves induce a small strain

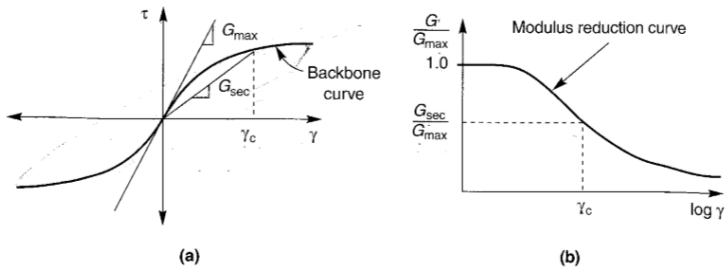

Figure 2.5: Secant stiffness and G_{max} reduction[13].

as they propagate, mostly below $3 * 10^{-4}$ [13]. As such we can assume that the

stiffness is constant and the material is linear elastic. We also assume it is isotropic, with properties being direction independent. Then without external sources Hooke's law for normal stresses in an isotropic solid can be written as:

$$\begin{pmatrix} \epsilon_{xx} \\ \epsilon_{yy} \\ \epsilon_{zz} \end{pmatrix} = \frac{1}{E} \begin{pmatrix} 1 & -\nu & -\nu \\ -\nu & 1 & -\nu \\ -\nu & -\nu & 1 \end{pmatrix} \begin{pmatrix} \sigma_{xx} \\ \sigma_{yy} \\ \sigma_{zz} \end{pmatrix}. \tag{2.4}$$

Where E the Young's modulus, or material stiffness. The poisson ratio ν gives the ratio of deformations in different directions. If a material has infinitely high volumetric stiffness then by volume conservation the poisson ratio is 0.5. The lower bound is usually take as 0 implying that range of values for poisson ratio is positive and compression in one coordinate direction will cause expansion in the other two directions.

$$\begin{aligned} E &= \frac{stress}{strain} &&= \frac{\sigma}{\epsilon} \\ \nu &= -\frac{transverse \quad strain}{longitudinal \quad strain} &&= -\frac{d\epsilon_{trans}}{d\epsilon_{axial}} \end{aligned}$$

The previous equation between stress and strain (Equation 2.4) can be inverted to express the stress in terms of strains:

$$\begin{pmatrix} \sigma_{xx} \\ \sigma_{yy} \\ \sigma_{zz} \end{pmatrix} = \begin{pmatrix} \lambda + 2\mu & \lambda & \lambda \\ \lambda & \lambda + 2\mu & \lambda \\ \lambda & \lambda & \lambda + 2\mu \end{pmatrix} \begin{pmatrix} \epsilon_{xx} \\ \epsilon_{yy} \\ \epsilon_{zz} \end{pmatrix}, \tag{2.5}$$

where λ and μ are again two elastic parameters, the Lamé coefficients, which can be written as functions of the Young's modulus and poisson's ratio via:

$$\lambda = \frac{\nu E}{(1-2\nu)(1+\nu)} \tag{2.6}$$

$$\mu = \frac{E}{2(1+\nu)}. \tag{2.7}$$

μ is also known as the shear modulus. In geotechnical engineering the shear modulus is often expressed as G. $\lambda + 2\mu$ is also recognized as the constrained modulus or oedometer modulus and often expressed as M or E_{oed}.

For shear stresses in an isotropic linear elastic medium they are related to the shear strain. Also the shear stresses and strains are symmetric.

$$\sigma_{ij} = \tau_{ij} = \mu\gamma_{ij} = 2\mu\epsilon_{ij} \text{ where } i \neq j \tag{2.8}$$

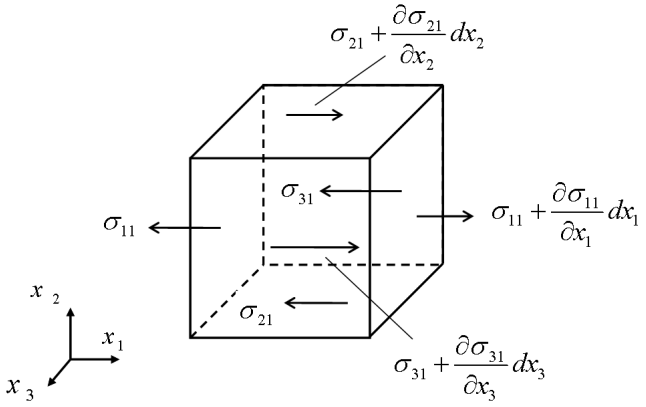

Figure 2.6: Control volume x_1 direction stresses [21].

It is easy to see that the shear stresses are only dependent on their respective shear strains:

$$\begin{pmatrix}\sigma_{xy}\\ \sigma_{xz}\\ \sigma_{yz}\end{pmatrix} = \begin{pmatrix}2\mu & 0 & 0\\ 0 & 2\mu & 0\\ 0 & 0 & 2\mu\end{pmatrix}\begin{pmatrix}\epsilon_{xy}\\ \epsilon_{xz}\\ \epsilon_{yz}\end{pmatrix}, \tag{2.9}$$

Written in compact Eistein notation both normal and shear stresses are expressed by this equation:

$$\sigma_{ij} = \lambda\epsilon_{kk}\delta_{ij} + 2\mu\epsilon_{ij} \tag{2.10}$$

where δ_{ij} the Kronecker delta.

2.1.3 Equilibrium Equation

Newton's second law is applied to a control volume and which leads to the equations below.

Considering the x_1 direction:

$$\rho\Delta x_1\Delta x_2\Delta x_3\frac{\partial^2 u_1}{\partial t^2} = (\frac{\partial\sigma_{11}}{dx_1}\Delta x_1)\Delta x_2\Delta x_3 + (\frac{\partial\sigma_{21}}{dx_2}\Delta x_2)\Delta x_1\Delta x_3 + (\frac{\partial\sigma_{31}}{dx_3}\Delta x_3)\Delta x_1\Delta x_2 \tag{2.11}$$

$$\rho \frac{\partial^2 u_1}{\partial t^2} = \frac{\partial \sigma_{11}}{\partial x_1} + \frac{\partial \sigma_{21}}{\partial x_2} + \frac{\partial \sigma_{31}}{\partial x_3} \tag{2.12}$$

For all 3 directions with index notation and summation convention:

$$\rho \ddot{u_i} = \sigma_{ji,j} \tag{2.13}$$

In summation convention, a term with a twice repeated index indicates summation over all the index numbers. In this equation j is the summation index which is summed from $1-3$, while the i index is simply enumerated $1-3$ to produce three separate equations.

2.1.4 3D Elastic Equation

By substituting the kinematic Equation 2.3 into the constitutive Equation 2.10 we can express the stresses in terms of displacements:

$$\sigma_{11} = \lambda(u_{1,1} + u_{2,2} + u_{3,3}) + 2\mu u_{1,1} \tag{2.14}$$

$$\sigma_{21} = \mu(u_{1,2} + u_{2,1}) \tag{2.15}$$

Or in general:

$$\sigma_{ij} = \lambda u_{k,k}\delta_{ij} + \mu(u_{i,j} + u_{j,i}) \tag{2.16}$$

Which can then be substituted into Equation 2.13 to determine the final general 3D elastic equation:

$$\rho \ddot{u_i} = \lambda u_{j,ji} + \mu(u_{i,jj} + u_{j,ij}) \tag{2.17}$$

If it is first grouped:

$$\rho \ddot{u_i} = (\lambda + \mu)u_{j,ij} + \mu u_{i,jj} \tag{2.18}$$

Then it can be expressed in vector form which may be more recognizable. The body force vector, $\bar{f}_{ext}$, is also included for completeness.

$$\rho \ddot{\bar{u}_i} = (\lambda + \mu)\nabla(\nabla \cdot \bar{u}) + \mu \nabla^2 \bar{u} + \bar{f}_{ext} \tag{2.19}$$

2.1.5 Acoustic Equation

The acoustic equation, which is assumed governs wave propagation in water as fluids do not develop shear stresses, can be obtained from the elastic equation. Simply, the acoustic medium has no shear stiffness and the acoustic equation is a subset of the elastic equation with $\mu = 0$.

$$\rho \ddot{\bar{u}_i} = \lambda \nabla \nabla \cdot \bar{u} + \bar{f} \tag{2.20}$$

2.2 2D Modal Surface Wave Equations

In the MASW test a line array will be used to measure the response as the produced wave propagates through the soil below the array. If source is aligned with the direction of the array then the wavefronts will always be normal to the array and we can consider a 2D slice acting through the array and the source. Very close to the source it will be spherical or cylindrical wavefront but some distance from the source the curvature of the wavefront will be very small and can be approximated as a planar wave. This is equivalent to a line source in a 3D space which would produce planar waves. The derivation of 2D surface waves in plane homogeneous medium is the simplest place to start for understanding the propagation of surface waves. It is assumed that the motion is all in the x_1 (horiztonal) and x_3 (vertical) direction and all derivatives with respect to the x_2 (out of page) direction are zero. This means Love waves will not be present in the solution, but the goal of this derivation is to prove the existence and nature of the Rayleigh waves.

We can use the Helmholtz decomposition [8] in order to decouple the elastic wave equation with the scalar potential ϕ and the vector potential ψ which separates the displacement into a rotation free part, u_p, and a divergence free part, u_s which will later be recognized as the pressure wave and shear wave components.

$$\bar{u} = \nabla\phi + \nabla \times \bar{\psi} = \bar{u}_p + \bar{u}_s \tag{2.21}$$

Where $\nabla \times \bar{u}_p = 0$ and $\nabla \cdot \bar{u}_s = 0$. It should also be noted that for the 2D scenario the $\nabla \times \bar{\psi}$ vector only contains rotation in the 2D plane and so there is only one axis of rotation, normal to the 2D plane. Hence $\bar{\psi}$ will be simplified to ψ which for the x_1, x_3 plane will be a scalar field associated with the x_2 direction vector. With substituting this Equation 2.21 into the governing wave Equation 2.19 we get:

$$\rho\partial_t^2(\nabla\phi + \nabla \times \bar{\psi}) = (\lambda + \mu)\nabla(\nabla \cdot (\nabla\phi + \nabla \times \bar{\psi})) + \mu\nabla^2(\nabla\phi + \nabla \times \bar{\psi}) \tag{2.22}$$

We must use several vector identities in order to rearrange this equation. The laplace operator can be interchanged with the gradient and curl operator.

$$\begin{aligned} \nabla \cdot (\nabla \times \psi) &= 0 \\ \nabla \cdot \nabla &= \nabla^2 \\ \nabla^2(\nabla\phi) &= \nabla(\nabla^2\phi) \\ \nabla^2(\nabla \times \psi) &= \nabla \times (\nabla^2\psi) \end{aligned} \tag{2.23}$$

Then Equation 2.22 can be separated into two equations which we can set both as equal to zero in order to find a solution:

$$\begin{aligned} \rho\partial_t^2\phi - (\lambda+2\mu)\nabla^2\phi = 0 \\ \rho\partial_t^2\psi - \mu\nabla^2\psi = 0 \end{aligned} \tag{2.24}$$

These equations can be seen to have the structure of a classic wave equation with second order time derivative and second order spatial derivatives. The wave velocities can also be identified.

$$\begin{aligned} \frac{1}{C_p^2}\partial_t^2\phi = \nabla^2\phi, \quad C_p = \sqrt{\frac{\lambda+2\mu}{\rho}} \\ \frac{1}{C_s^2}\partial_t^2\psi = \nabla^2\psi, \quad C_s = \sqrt{\frac{\mu}{\rho}} \end{aligned} \tag{2.25}$$

We recall that for 2D cartesian case the Laplace operator is:

$$\nabla^2 f = \frac{\partial^2 f}{\partial x_1^2} + \frac{\partial^2 f}{\partial x_3^2}$$

Then, we take these equations into the Fourier domain based on the definition of the forward Fourier transformation:

$$\tilde{\tilde{f}}(\kappa_1, x_3, \omega) = \int_{-\infty}^{\infty}\int_{-\infty}^{\infty} f(x_1, x_3, t)e^{i(\kappa_1 x_1 - \omega t)}dx_1 dt \tag{2.26}$$

which has the corresponding inverse definition:

$$f(x_1, x_3, t) = \frac{1}{(2\pi)^2}\int_{-\infty}^{\infty}\int_{-\infty}^{\infty} \tilde{\tilde{f}}(k_1, x_3, \omega)e^{-i(k_1 x_1 - \omega t)}dx_1 dt \tag{2.27}$$

Leading to the Fourier domain equations

$$\begin{aligned} -\frac{\omega^2}{C_p^2}\tilde{\tilde{\phi}} = -k_1^2\tilde{\tilde{\phi}} + \frac{d^2\tilde{\tilde{\phi}}}{dx_3^2} \\ -\frac{\omega^2}{C_s^2}\tilde{\tilde{\psi}} = -k_1^2\tilde{\tilde{\psi}} + \frac{d^2\tilde{\tilde{\psi}}}{dx_3^2} \end{aligned} \tag{2.28}$$

As seen by the choice of integration kernel for the fourier transformation, this corresponds to a solution which is a summation of components of harmonic propagating

waves of $e^{i(k_1 x_1 - \omega t)}$ in the time-space domain. Also we recognize two wavenumbers related to the shear and pressure body wave speeds C_s and C_p which are generally known:

$$k_p = \frac{\omega}{C_p} \quad k_s = \frac{\omega}{C_s} \tag{2.29}$$

It is then recognizable as two ODEs in x_3:

$$\begin{aligned} \frac{d^2\tilde{\tilde{\phi}}}{dx_3^2} + (k_p^2 - k_1^2)\tilde{\tilde{\phi}} = 0 \\ \frac{d^2\tilde{\tilde{\psi}}}{dx_3^2} + (k_s^2 - k_1^2)\tilde{\tilde{\psi}} = 0 \end{aligned} \tag{2.30}$$

Which are known to have solutions:

$$\begin{aligned} \tilde{\tilde{\phi}}(k_1, x_3, \omega) = Ae^{-q_p x_3} + Be^{q_p x_3}, \quad q_p = \sqrt{k_1^2 - k_p^2} > 0 \\ \tilde{\tilde{\psi}}(k_1, x_3, \omega) = Ce^{-q_s x_3} + De^{q_s x_3}, \quad q_s = \sqrt{k_1^2 - k_s^2} > 0 \end{aligned} \tag{2.31}$$

C_1 is the Rayleigh wavespeed, which for a isotropic halfspace we expect a single magnitude of wavespeed with positive and negative roots corresponding to a $+x_1$ and $-x_1$ propagating wave. The roots corresponding to the evanescent waves in the x_1 direction are not considered. For the x_3 direction we want a solution which does not propagate but rather decays, and therefore q_p and q_s must be real valued, hence $k_1 > k_s > k_p$ The unknown coefficients A,B,C,D and k_1 must be solved with boundary conditions. For a halfspace, since the solution must be finite at infinity we can immediately say that $B = D = 0$ since these terms are exponentially increasing. Additionally, the free-surface is stress free:

$$\sigma_{33}(x_1, x_3 = 0, t) = \sigma_{31}(x_1, x_3 = 0, t) = 0 \tag{2.32}$$

The displacements and stresses are expressed in terms of the potentials using Equations 2.21 and 2.16. The symbolic software Maple was used in order to verify these expressions.

Displacements:

$$\begin{aligned} u_1(x_1, x_3, t) = \partial_1\tilde{\tilde{\phi}} - \partial_3\tilde{\tilde{\psi}} = -ik_1\tilde{\tilde{\phi}} - \partial_3\tilde{\tilde{\psi}} \\ u_3(x_1, x_3, t) = \partial_3\tilde{\tilde{\phi}} + \partial_1\tilde{\tilde{\psi}} = \partial_3\tilde{\tilde{\phi}} + -ik_1\tilde{\tilde{\psi}} \end{aligned} \tag{2.33}$$

Stresses:

$$\begin{aligned}\sigma_{33}(x_1,x_3,t) &= \lambda(\partial_1^2\tilde{\tilde{\phi}}+\partial_3^2\tilde{\tilde{\psi}})+2\mu(\partial_3^2\tilde{\tilde{\phi}}+\partial_{13}^2\tilde{\tilde{\psi}})\\ &= \lambda(-k_1^2\tilde{\tilde{\phi}}+\partial_3^2\tilde{\tilde{\psi}})+2\mu(\partial_3^2\tilde{\tilde{\phi}}-ik_1\partial_3\tilde{\tilde{\psi}})\\ \sigma_{31}(x_1,x_3,t) &= \mu(2\partial_{13}^2\tilde{\tilde{\phi}}+\partial_1^2\tilde{\tilde{\psi}}-\partial_3^2\tilde{\tilde{\psi}})\\ &= \mu(-2ik_1\partial_3\tilde{\tilde{\phi}}+\partial_1^2\tilde{\tilde{\psi}}-\partial_3^2\tilde{\tilde{\psi}})\end{aligned} \tag{2.34}$$

Equations 2.31, 2.32 and 2.34 are combined, giving two equations with the unknowns A,C and k_1 which after rearranging can be written in the matrix form:

$$\begin{pmatrix}2k_1^2-k_s^2 & 2ik_1q_s\\ -2ik_1q_p & 2k_1^2-k_s^2\end{pmatrix}\begin{pmatrix}A\\C\end{pmatrix}=\begin{pmatrix}0\\0\end{pmatrix} \tag{2.35}$$

This homogeneous problem can only be solved when the matrix containing the coefficients of A,C has determinant equal to zero. Traditionally, this will result in determining the unknown Rayleigh wavenumber k_1. This is the modal solution since no forcing is present and the wavenumber is determined from eigenvalues of this matrix. There will be two eigenvalues for a 2×2 matrix and they must have the same magnitude but opposite sign, corresponding to $+x_1$ and $-x_1$ propagating waves. The ratio of the two scalar potentials ϕ and ψ is determined by the eigenvectors of the matrix, which can be manipulated into the ratio of the vertical and horizontal motions. The absolute magnitude of the displacements cannot be determined since the solution is rank-deficient for the homogeneous problem. In simple terms, no force is provided and so there cannot be any displacements, rather the modal solution is a property of the body. It can be demonstrated that the A and B coefficients are $\frac{\pi}{2}$ out of phase and the motion takes on an elliptical pattern.

Note, that while the traditional solution to the homogeneous problem for the real valued Rayleigh wave-number is correct, it is not complete. There is another complex valued root pair corresponding to the body waves. These solutions are complex because they are not limited to the surface but rather spread out continuously in the x_1-x_3 plane, thus leading to an attenuation or decrease in amplitude, known as geometric damping. This will be discussed in the introduction of damping to the equations, but it is important to realize that complex valued solutions can exist. However, this body wave decays, so at a distance far from the source their effect can be said to be negligible and they are often of minor importance in surface wave analysis. Figure 2.7 is a schematic which shows the complex wavenumber plane for

a homogeneous halfspace. Note that the complex root pair may lie on the real axis for specific values of the poisson ratio, that is $\nu \leq 0.2$

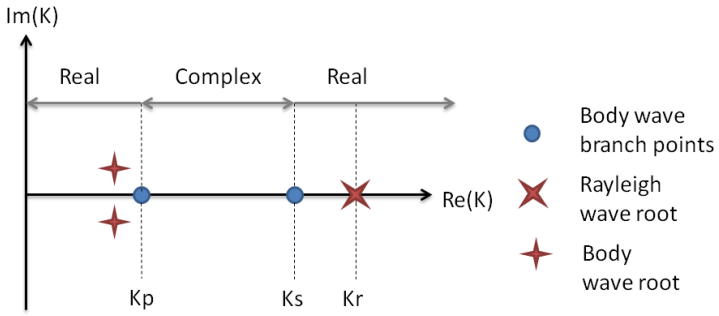

Figure 2.7: Schematic of the complex wavenumber plane for a homogeneous media show the real roots, complex roots and the branch points.

The Rayleigh wavenumber, K_r, lies on the real axis. Branch points are locations where the determinant reaches a singularity and changes form, but these are not root locations. The two branch points occur at K_p and K_s, the pressure and shear wavenumbers associated with the body velocities. Below K_p and above K_s the determinant is real valued. This is observed from inspecting the determinant equation show below, which is directly obtained by taking the determinant of the matrix in Equation 2.35. Note, a layered system will contain more branch points.

$$(2k_1^2 - k_s^2)^2 - (2 * k_1)^2 \sqrt{k_1^2 - k_s^2} \sqrt{k_1^2 - k_p^2} \tag{2.36}$$

Considering again only the real valued solution we see from the equations that the Rayleigh wave number and the ratio of deformations only depends on the ratio of the constrained modulus $\lambda + 2\mu$ and the shear modulus μ in the halfspace. In terms of more physical parameters then it is only the ratio of the C_p and C_s velocities which determines the characteristics of the system. In the limit case, where the shear stiffness, or S wave speed, tends to zero, then the halfspace responds as an acoustic halfspace.

If we assume $0 < \nu < 0.5$ and λ must be positive and we can rearrange to show

$$\lambda = \frac{E\nu}{(1+\nu)(1-2\nu)} = \mu(\frac{C_p^2}{C_s^2} - 2) \tag{2.37}$$

$$0 < \frac{C_s}{C_p} < \frac{1}{\sqrt{2}} \tag{2.38}$$

If the reader is interested in a deeper physical understanding of these equations, there are some illustrations and further discussion in the author's previous report [2]. Note also, for the $\frac{C_s}{C_p}$ range given above the $\frac{C_1}{C_s}$ ratio lies between $0.878 - 0.955$.

2.3 Damped Full Waveform Equations

2.3.1 Adding a Force

If it is of interest to solve the absolute displacements, to create a synthetic seismic test or to compare with measured results, then a force must be included and the inhomogeneous problem solved. The step to the full waveform solution is actually quite small and in some ways easier to consider than the modal solution. We are ultimately concerned with seismic measurements on the seabed and here we consider an impulsive pressure source which can, for the simplest example, be represented as a dirac delta pulse. However, other force profiles can be used, such as a ricker pulse or a measured spectrum which will result in different response spectrums. The dirac case is the simplest because it highlights the entire spectrum uniformly. The dirac force:

$$F(x_1, x_3, t) = \delta(t)\delta(x_1)\delta(x_3) \tag{2.39}$$

Which transformed into the fourier domain and evaluated at $x_3 = 0$ becomes:

$$F(k_1, x_3 = 0, \omega) = 1 \tag{2.40}$$

Hence, with a vertically acting normal stress source the Equation 2.35 then becomes:

$$\begin{pmatrix} 2k_1^2 - k_s^2 & 2ik_1q_s \\ -2ik_1q_p & 2k_1^2 - k_s^2 \end{pmatrix} \begin{pmatrix} A \\ C \end{pmatrix} = \begin{pmatrix} 1 \\ 0 \end{pmatrix} \tag{2.41}$$

The variable k_1 is no longer considered an unknown, but rather like ω it is a specified value for which we wish to identify the response. Hence the matrix can be viewed as a function $f(\omega, k_1, C_p, C_s)$, where the compressional and shear body wave velocities are chosen over the stiffness and density because it is a more physically intuitive term and also what is often measurable. However, C_p and C_s depend on $E, \nu, \rho, \lambda, \mu, \zeta$ where some of these parameters are dependent, but they are shown here for completeness and clarity since various combinations of these parameters may be used to define the inputs.

The matrix can be inverted to determine the unknown potential amplitude coefficients stored in the vector X.

$$\begin{aligned} \bar{\bar{M}}\,\bar{X} &= \bar{F} \\ \bar{X} &= \bar{\bar{M}}^{-1}\,\bar{F} \end{aligned} \tag{2.42}$$

However, at some frequency-wavenumber combinations the determinant of $\bar{\bar{M}}$ will be zero and the determinant is said to be singular and non-invertible. This is of course occurring at the roots of the modal solution. These are the 'resonant' combinations of the system and have 'infinite' amplitudes. In order to be able to invert the matrix for all frequency-wavenumber combinations, a small amount of damping can be added which is a physical way to make the amplitude finite. If the damping is very low then the matrix may be ill-conditioned and regularization techniques may need to be used in order to calculate a stable inverse. Inspection of singular values indicates that the ill-conditioning can be either discrete or rank deficient. Truncated singular value decomposition can be used for rank-deficient problems. Tikhonov regularization is required for discrete problems and can also be used for rank-deficient problems. Some literature [10] recommends using Tikhonov regularization and practically this makes sense since it can address both types of ill-conditioning. However, applying damping was sufficient so that regularization was not required.

2.3.2 Adding Damping

There are two types of damping [19] which contribute to the decay of soil waves. Geometric or radiation damping, which is a decrease in the amplitude of the wave due to the geometric spreading of the wave front. In an isotropic continuum the wavefront will be spherical and the geometric damping is proportional to $\frac{1}{r}$. For a halfspace the Rayleigh wave travels only along the surface and geometrical damping is proportional to $\frac{1}{\sqrt{r}}$, while body waves travelling at the interface decay faster with a rate of $\frac{1}{r^2}$ [9], [10]. In more complex layered systems it is not possible to find a simple geometric relation for radiation damping. The other type is material damping, which is a loss of energy due to internal dissipation within the material. This can be modelled in several different ways:

Viscous Damping

Viscous damping is commonly used in modelling a single degree of freedom mass-spring-damper system. The damping force is proportional to velocity. The damping work done in one cycle can therefore be shown to be proportional to the damping coefficient, the frequency and the square of the amplitude [19].

$$W_d = (\pi \omega c)\, u_o^2 \tag{2.43}$$

This is derived in Appendix A. Viscous damping can be applied through use of a complex stiffness. $*$ denotes a complex valued term.

$$\lambda^* = \lambda_0 (1 + i\omega\varepsilon_\lambda) \tag{2.44}$$
$$\mu^* = \mu_0 (1 + i\omega\varepsilon_\mu) \tag{2.45}$$

The soil system or coefficient matrix, M, is computed at every frequency and wavenumber separately so it is easy to add in damping which is either frequency or wavenumber dependent. In this case, we simply substitute the complex stiffness into the equations already derived.

Hysteretic Damping

It has been noted by researchers that damping in soils is not dependent on frequency [19] and that viscous damping leads to an overestimation of damping at higher frequencies due to the linear increase of damping with frequency. The hysteretic model is similar to the viscous damping but the equivalent viscous damping coefficient is divided by ω to make the damping work per cycle independent of frequency.

$$W_d = const\, u_o^2 \tag{2.46}$$

The hysteretic damping is similarly applied with a complex stiffness.

$$\lambda^* = \lambda_0 (1 + i\eta_\lambda) \tag{2.47}$$
$$\mu^* = \mu_0 (1 + i\eta_\mu) \tag{2.48}$$

The derivation in Appendix A shows how the loss factor, η, can be directly related to a critical damping ratio, ζ, through an analogy to the single degree of freedom mass-spring-damper system. This damping ratio is often given by ζ for single degree of freedom systems while in soil modelling is often referred to by the capital letter *D*. In this thesis we will refer to the material or intrinsic damping as ζ while *D* will be reserved for the modal damping which is explained in Chapter 6.

$$\zeta = \frac{1}{2}\eta \tag{2.49}$$

Coulomb Damping

The Coulomb model of damping hypothesizes that the damping should only be proportional to the displacement amplitude and not the square of the displacement amplitude. This is also sometimes referred to as dry friction or sliding friction. Hence, the equivalent viscous damper must be divided by the displacement amplitude such that:

$$W_d = const\, u_o \tag{2.50}$$

Coulomb friction will not be used because it is not thought to represent the damping behaviour of soil accurately. Instead the focus will be on hysteretic damping as suggested by [19] and possibly also viscous damping, since it can be implemented in a very similar way.

Since adding damping increases the complexity, it is a good point to clarify a few facts about these equations with and without damping. Without damping, all system parameters (wave velocities) are real valued. However, the determinant is generally complex, as shown in Figure 2.7. The Rayleigh velocity which solves the modal solution must be real (ignoring for now the complex body wave solutions which are not surface wave solutions). The halfspace system response, computed at some chosen surface or subsurface location, will be complex, since the determinant (appearing in the denominator of the response) is complex. Physically this makes sense, as we expect we can express all of the frequency-wavenumber solution components in terms of a magnitude and phase angle.

Adding damping, the P-wave and S-wave velocities can be seen as being complex due to the complex stiffness. The determinant and response, will naturally also remain complex. Additionally, the Rayleigh wavenumber (or velocity) solution of the homogeneous or modal problem must also be complex ie $k_1 = k_{1,RE} + ik_{1,IM}$. To understand physically what this means, we consider the integration kernel or basis function $e^{i(\omega t - k_1 x_1)}$. If we expand this with the complex wavenumber then we see

$$e^{i(\omega t-(k_{1,RE}+ik_{1,IM})x_1)} = e^{k_{1,IM}x_1}e^{i(\omega t-(k_{1,RE})x_1)} \tag{2.51}$$

The real part of this wavenumber k_{RE} corresponds to the wave propagation and the physical wavelength which is detected by a surface array. It is important to note this, that the physical array and the Fourier transformation made to process the data corresponds to the real part of the wavenumber, and no information about the imaginary part is gathered through Fourier transformation of the data. Equally, we compute the full waveform response over the frequency-real wavenumber plane, as we did before, although the modal solutions lie out of this real plane and instead

on the complex wavenumber plane. The imaginary part of the wavenumber, as can be seen above, no longer corresponds to a complex exponential or propagating function, but to a real valued exponential. This corresponds to an exponential decay in the direction of wave propagation if no mistakes have been made with the sign convention. Hence if k_{RE} is positive, we expect k_{IM} to be negative and vice versa. Modal solutions only exist in two of the four quadrants of the complex wavenumber plane.

2.4 Cylindrical Coordinate Equations

The derivations for the cylindrical coordinate formulation in this section were completed with the aid of [1].

Determination of the damping is tied precisely to amplitudes and energy distributions. Since we are interested in determining the material damping and this is combined with the geometric damping, we can conclude that we must correctly model the geometric damping in order to determine the material damping. Hence, we must model our physical system correctly. Although, we have discussed geometric damping as the spreading of wavefront, let us try to understand physically how this is different between 2D and 3D and also understand how geometric damping relates to the typical frequency-wavenumber domain analysis, before jumping into the 3D equation derivations.

Geometric damping cannot be seen in the wavenumber domain, it is a spatial phenomenon, occurring in the space domain. With the Fourier transform we make a change of basis from space/distance to wavenumber, so that the solution no longer depends on the original spatial coordinate. Of course, this information is carried into the wavenumber domain through the corresponding correct amplitude and phase components, but the loss of energy with distance only exists in the complete solution as the combination of all wavenumber components.

Firstly, consider the undamped 2D case where the basis functions are sinusoids. If you examine any individual harmonic component then the amplitude will never decay and it continues to infinity. In this case, with the line source, it logically follows that there is no geometric spreading of the interface waves since they are depth constrained and do not radiate energy into the lower halfspace, nor spread laterally, since we consider an infinite line source. So while it may seem strange, we logically conclude that in the hypothetical scenario of an infinite line source applied on an undamped elastic homogeneous media, the interface waves which are depth constrained, do not experience geometric damping in the far field. They are not

subject to any amplitude decay, leading to a wave which will propagate forever. Clearly, this must be a simplification.

If we instead consider a point source, then we can formulate the equations in cylindrical coordinates and we see the effect of the lateral spreading of energy as the propagation wavefront circumference is constantly expanding. Cylindrical type ODE problems are well known to have solutions that can be expressed in terms of Bessel functions. These Bessel function solutions naturally incorporate the 3D spreading of energy and the decay of the amplitude, as shown in figure 2.8. Hence, even in undamped media, the interface waves will have a decay of amplitude which is due to the geometric damping and the spreading of the wavefronts. In an homogeneous halfspace, Rayleigh waves are known to decay at $\frac{1}{\sqrt{r}}$. The Bessel functions are essentially a combination of a sinusoidal function and a real valued exponential decay. This leads to some methods that use the 2D equation formulations but include a 'geometric spreading factor' to account for this amplitude decay. The problem is that the analytical solution of the decay factor is only known for the homogeneous halfspace case, and for layered soil systems this factor must be estimated as part of an inversion approach. It is better to use the 3D equations which can automatically account for geometric damping in a layered media. Of course, in any of these methods it should be noted that errors in the estimate of the stiffness profile may lead to errors in the geometric damping. Approaches which use spatial domain processing to estimate the damping are especially subject to these errors since the combination of propagating modes results in a complicated amplitude versus distance pattern which does not simply decay exponentially but may have local increases due to constructive interference of waves.

The derivation now considers the waves generated by a point source in a 3D domain. However, for our purpose we consider only the axi-symmetric case, so there is motion only in 2 dimensions - the radial (r) and vertical (z) dimensions, and the mathematics is not much more complicated than the cartesian case. With the axi-symmetric assumption we can then say $u_\theta = 0$ and $\partial_\theta = 0$. Hence, the Helmholtz decomposition of the displacement, previously given in Equation 2.21, is $\bar{u} = \nabla\phi + \nabla \times \bar{\psi}$. It was expanded using the definition of the curl in cylindrical coordinates as obtained from Maple:

$$\begin{pmatrix} u_r \\ u_\theta \\ u_z \end{pmatrix} = \begin{pmatrix} \partial_r \phi \\ \partial_\theta \phi \\ \partial_z \phi \end{pmatrix} + \begin{pmatrix} \frac{1}{r}\partial_\theta \psi_z - \frac{1}{r}\partial_z (r\psi_\theta) \\ \partial_z \psi_r - \partial_r \psi_z \\ \frac{1}{r}\partial_r (r\psi_\theta) - \frac{1}{r}\partial_\theta \psi_r \end{pmatrix} \tag{2.52}$$

If $u_\theta = 0$ then it follows $\psi_r = \psi_z = 0$ which is also proven if $\psi \sim \nabla \times u$. Hence, $\bar{\psi}$ is

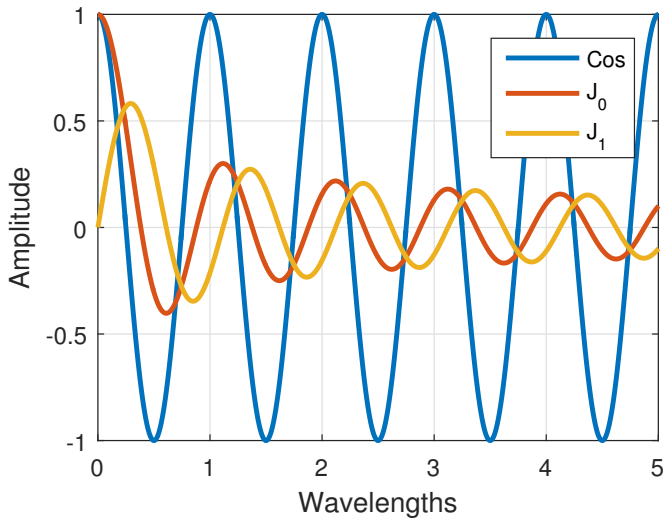

Figure 2.8: Bessel functions automatically include amplitude decay while harmonic functions do not.

simply written as ψ because only ψ_θ is non-zero and Equation 2.52 is simplified to:

$$\begin{pmatrix} u_r \\ u_\theta \\ u_z \end{pmatrix} = \begin{pmatrix} \partial_r \phi - \partial_z \psi \\ 0 \\ \partial_z \phi + \frac{1}{r} \partial_r (r\psi) \end{pmatrix} \tag{2.53}$$

We also need the stress equations and from Equations 2.5 and 2.9, we know the definition of the relevant compressional and shear stresses are:

$$\begin{aligned} \sigma_{zz} &= (\lambda + 2\mu)\epsilon_z + \lambda(\epsilon_r + \epsilon_\theta) \\ \tau_{zr} &= \mu \gamma_{zr} \end{aligned} \tag{2.54}$$

However, the strain vectors are different in cylindrical coordinates [20].

$$\begin{pmatrix} \epsilon_r \\ \epsilon_\theta \\ \epsilon_z \\ \gamma_{r\theta} \\ \gamma_{\theta z} \\ \gamma_{zr} \end{pmatrix} = \begin{pmatrix} \partial_r u_r \\ \frac{u}{r} + \frac{1}{r}\partial_\theta u_\theta \\ \partial_z u_z \\ \partial_r u_\theta + \frac{1}{r}\partial_\theta u_r - \frac{u_\theta}{r} \\ \frac{1}{r}\partial_\theta u_z + \partial_z u_\theta \\ \partial_z u_r + \partial_z u_z \end{pmatrix} \tag{2.55}$$

Substitution into the stress Equation 2.54 results in the cylindrical coordinate stresses given in Equation 2.56. The compressive stress was written in a simpler form using the chain rule, and $\partial_\theta = 0$ applied due to axisymmetry.

$$\begin{aligned} \sigma_{zz} &= (\lambda + 2\mu)\partial_z u_z + \lambda(\partial_r u_r + \frac{u_r}{r} + \frac{1}{r}\partial_\theta u_\theta) \\ &= (\lambda + 2\mu)\partial_z u_z + \frac{\lambda}{r}\partial_r(r u_r) \\ \tau_{zr} &= \mu\partial_z u_r + \partial_z u_z \end{aligned} \tag{2.56}$$

If the displacements from Equation 2.53 are substituted into Equation 2.56 then the stresses in terms of potentials becomes:

$$\begin{aligned} \sigma_{zz} &= (\lambda + 2\mu)\partial_z(\partial_z\phi + \frac{1}{r}\partial_r(r\psi)) + \frac{\lambda}{r}\partial_r(r(\partial_r\phi - \partial_z\psi)) \\ \tau_{zr} &= \mu\partial_z(\partial_r\phi - \partial_z\psi) + \partial_z(\partial_z\phi + \frac{1}{r}\partial_r(r\psi)) \end{aligned} \tag{2.57}$$

The Helmholtz separation and all the stages leading to Equations 2.25 were performed with vector mathematics and therefore the coordinate system is, up to that point generalized. So we can also take the governing equations and continue in cylindrical coordinates

$$\frac{1}{C_p^2}\partial_t^2\phi = \nabla^2\phi$$
$$\frac{1}{C_s^2}\partial_t^2\psi = \nabla^2\psi$$

Hence, we begin with these equations and use the appropriate scalar and vector laplace definition in cylindrical (r, θ, z) coordinates [35]. Scalar laplacian:

$$\nabla^2 f = \frac{1}{r}\partial_r(r\partial_r f) + \frac{1}{r^2}\partial_\theta^2 f + \partial_z^2 f \tag{2.58}$$

Vector laplacian of $\bar{V}$:

$$\nabla^2\bar{V} = \nabla^2\begin{pmatrix} V_r \\ V_\theta \\ V_z \end{pmatrix} = \begin{pmatrix} \partial_r^2 V_r + \frac{1}{r^2}\partial_\theta^2 V_r + \partial_z^2 V_r + \frac{1}{r}\partial_r V_r - \frac{2}{r^2}\partial_\theta V_\theta - \frac{V_r}{r^2} \\ \partial_r^2 V_\theta + \frac{1}{r^2}\partial_\theta^2 V_\theta + \partial_z^2 V_\theta + \frac{1}{r}\partial_r V_\theta + \frac{2}{r^2}\partial_\theta V_r - \frac{V_\theta}{r^2} \\ \partial_r^2 V_z + \frac{1}{r^2}\partial_\theta^2 V_z + \partial_z^2 V_z + \frac{1}{r}\partial_r V_z \end{pmatrix} \tag{2.59}$$

Which for the axi-symmetric case, including the fact that $\partial_\theta = 0$, the vector Laplacian reduces to:

$$\nabla^2 V_\theta = \partial_r^2 V_\theta + \partial_z^2 V_\theta + \frac{1}{r}\partial_r V_\theta - \frac{V_\theta}{r^2} \tag{2.60}$$

The substitution is made into Equations 2.25 (also repeated above), which leads to:

$$\begin{aligned} \frac{1}{C_p^2}\partial_t^2\phi &= \partial_r^2\phi + \frac{1}{r}\partial_r\phi + \partial_z^2\phi \\ \frac{1}{C_s^2}\partial_t^2\psi &= \partial_r^2\psi + \partial_z^2\psi + \frac{1}{r}\partial_r\psi - \frac{\psi}{r^2} \end{aligned} \tag{2.61}$$

These equations are transformed into the frequency domain with a single Fourier integral, similar to the double Fourier integration performed previously.

$$\begin{aligned} -\frac{\omega^2}{C_p^2}\tilde{\phi} &= \partial_r^2\tilde{\phi} + \frac{1}{r}\partial_r\tilde{\phi} + \partial_z^2\tilde{\phi} \\ -\frac{\omega^2}{C_s^2}\tilde{\psi} &= \partial_r^2\tilde{\psi} + \partial_z^2\tilde{\psi} + \frac{1}{r}\partial_r\tilde{\psi} - \frac{\tilde{\psi}}{r^2} \end{aligned} \tag{2.62}$$

Now we have the displacement, the stress and the governing equations in terms of potentials, they can all be transformed to the wavenumber domain using the appropriate Hankel transformation. The detailed transformation of Equations 2.53, 2.57 and 2.62 are shown in Appendix C. Different orders of Hankel transformation are used in order to get the equations in the most convenient form. The order of Hankel transformation is dependent on the order of the Bessel function which is used in the integration kernel and the order is denoted by n in Equation 2.63.

$$\tilde{f}^{H_n}(\kappa_r, x_3, \omega) = \int_0^\infty \tilde{f}(r, x_3, \omega) r J_n(r\kappa_r) dr \tag{2.63}$$

The Hankel transformed wave equations in the frequency-wavenumber domain which are derived in the Appendix C are:

$$\partial_z^2 \tilde{\phi}^{H_0} - (k_r^2 - k_p^2)^2 \tilde{\phi}^{H_0} = 0 \tag{2.64}$$

$$\partial_z^2 \tilde{\psi}^{H_1} - (k_r^2 - k_s^2) \tilde{\psi}^{H_1} = 0 \tag{2.65}$$

These are almost identical to the wave equations obtained by the 2D cartesian derivation and shown in Equation 2.30.

This type of equation is known to have the solutions of the following form:

$$\begin{aligned} \tilde{\phi}^{H_0}(k_r, x_3, \omega) &= Ae^{-q_p x_3} + Be^{q_p x_3}, \quad q_p = \sqrt{k_r^2 - k_p^2} > 0 \\ \tilde{\psi}^{H_1}(k_r, x_3, \omega) &= Ce^{-q_s x_3} + De^{q_s x_3}, \quad q_s = \sqrt{k_r^2 - k_s^2} > 0 \end{aligned} \tag{2.66}$$

The wavernumber domain displacement and stress equations which where derived in Appendix C are:

$$\tilde{u}_r^{H1} = -k_r \tilde{\phi}^{H_0} - \partial_z \tilde{\psi}^{H_1} \tag{2.67}$$

$$\tilde{u}_z^{H_1} = \partial_z \tilde{\phi}^{H_0} + k_r \tilde{\psi}^{H_1} \tag{2.68}$$

$$\begin{aligned} \tilde{\sigma}_{zz}^{H_0} &= \mu\Big((2k_r^2 - k_s^2)\tilde{\phi}^{H_0} + 2k_r \partial_z \tilde{\psi}^{H_1}\Big) \\ \tilde{\sigma}_{zz}^{H_0} &= -\rho\omega^2 \tilde{\phi}^{H_0} \quad \text{(for acoustic media)} \end{aligned} \tag{2.69}$$

$$\tilde{\tau}_{zr} = -\mu\Big(2k_r \partial_z \tilde{\phi}^{H_0} + (2k_r^2 - k_s^2)\tilde{\psi}^{H_1}\Big) \tag{2.70}$$

These equations can also be manipulated into a format which is very similar to the displacement and stress equations for the 2D cartesian case given in Equations 2.33 and 2.33. The equations are compared in table 2.1 and show remarkable similarity. This supports the findings of the author that the wavenumber domain solutions are identical in magnitude for 2D and 3D formulations. This is further supported by [15] which states:

A very important indeed fundamental observation that can be made about waves in horizontally layered media is that the wave spectra for SV-P and SH waves do not depend on whether plane-strain waves or cylindrical waves are being considered, even if the displacements patterns elicited by such waves are not the same. For example, guided torsional (cylindrical SH) waves in a layer over an elastic half-space exhibit exactly the same dispersion characteristics as plane Love waves in that same medium, that is, they propagate at exactly the same speed for a given frequency. Thus, it suffices for us to consider in detail only the two plane strain cases for SH and SV-P waves, which we then generalize without much ado to cylindrical waves.

Table 2.1: Displacement and stress equations in 2D and 3D.

	Cartesian	Cylindrical
u_1	$(-ik_1)\tilde{\tilde{\phi}} - \partial_3\tilde{\tilde{\psi}}$	$-(k_r)\tilde{\tilde{\phi}} - \partial_3\tilde{\tilde{\psi}}$
u_3	$\partial_3\tilde{\tilde{\phi}} + (-ik_1)\tilde{\tilde{\psi}}$	$\partial_3\tilde{\tilde{\phi}} + (k_r)\tilde{\tilde{\psi}}$
σ_{31}	$\mu(2(-ik_1)\partial_3\tilde{\tilde{\phi}} + (-k_1^2)\tilde{\tilde{\psi}} - \partial_3^2\tilde{\tilde{\psi}})$	$\mu(-2(k_r)\partial_3\tilde{\tilde{\phi}} + (-k_r^2)\tilde{\tilde{\psi}} - \partial_3^2\tilde{\tilde{\psi}})$
σ_{33}	$(\lambda+2\mu)\partial_3^2\tilde{\tilde{\phi}} + \lambda(-k_1^2)\tilde{\tilde{\phi}} + 2\mu(-ik_1)\partial_3\tilde{\tilde{\psi}}$	$(\lambda+2\mu)\partial_3^2\tilde{\tilde{\phi}} + \lambda(-k_r^2)\tilde{\tilde{\phi}} + 2\mu(k_r)\partial_3\tilde{\tilde{\psi}}$

So if the magnitudes are identical, does it matter if we formulate in 2D or 3D? Of course! The basis functions in the integration kernel are still different and so taking the inverse transformations, the spatial domain solutions are different. Given the same spatial data, the choice of transformation will effect the energy spectra calculated which will be different for these two cases. So, the measured data must be transformed to the wavenumber domain using the Hankel transformation in order to correctly compute the distribution of energy in the wavenumber spectra. Also, any theoretical cases which wish to include the effect of windowing by windowing in the space domain, should use the Hankel transformation to transfer between space and wavenumber.

2.5 Layered Model

Now that the halfspace model has been understood, we can extended this to a horizontally layered soil system. The jump to a layered model is theoretically straightforward, although tracking the mathematics and understanding the more complex

solutions which can arise from such a system is indeed quite challenging. Maple symbolic software is used to generate the equations, which are then converted to Matlab code such that the models are pre-defined and hardcoded within the Matlab function. This adds the disadvantage of another step if the model is not created for the desired number of layers. From coding and running both methods, it was found the hard-coding the definitions offers a significant speed advantage as compared with creating the model for an arbitrary number of layers within Matlab.

2.5.1 Equations

We begin with Equation 2.31 and now allow for the possibility of different potentials in every layer, since every layer in general has different physical properties. Thus the layer number is now denoted by the index j. One global coordinate system is used with x_3 positive downwards and x_1 horizontally along the surface.

$$\begin{aligned}\tilde{\tilde{\phi}}_j(x_3) &= A_j e^{-q_{pj}x_3} + B_j e^{q_{pj}x_3}, \quad q_{pj} = \sqrt{k_1^2 - k_{pj}^2} > 0 \\ \tilde{\tilde{\psi}}_j(x_3) &= C_j e^{-q_{sj}x_3} + D_j e^{q_{sj}x_3}, \quad q_{sj} = \sqrt{k_1^2 - k_{sj}^2} > 0\end{aligned} \tag{2.71}$$

In order to help with the numerical computations, a scaling term is introduced which limits the size of the positive exponential. The negative exponential term starts at $e^{-q_{pj}x_3} = 1$ when $x_3 = 0$ and decreasing in magnitude in depth. The increasing exponential is scaled to the layer depth so that it reaches a value of 1 at the bottom of the layer.

$$\begin{aligned}\tilde{\tilde{\phi}}_j(x_3) &= A_j e^{-q_{pj}x_3} + B_j e^{q_{pj}(x_3 - thk_j)} \\ \tilde{\tilde{\psi}}_j(x_3) &= C_j e^{-q_{sj}x_3} + D_j e^{q_{sj}(x_3 - thk_j)}\end{aligned} \tag{2.72}$$

Where thk_j is the thickness of soil layer j. This is allowed since B and D are unknown constants. The displacements from Equation 2.33 can then be defined:

$$\begin{aligned}u_{1|j}(k_1, x_3, \omega) &= -ik_1\tilde{\tilde{\phi}}_j - \partial_3\tilde{\tilde{\psi}}_j \\ u_{3|j}(k_1, x_3, \omega) &= \partial_3\tilde{\tilde{\phi}}_j + -ik_1\tilde{\tilde{\psi}}_j\end{aligned} \tag{2.73}$$

And stresses from Equation 2.34:

$$\begin{aligned}\sigma_{33|j}(k_1, x_3, \omega) &= \lambda(-k_1^2\tilde{\tilde{\phi}}_j + \partial_3^2\tilde{\tilde{\psi}}_j) + 2\mu(\partial_3^2\tilde{\tilde{\phi}}_j - ik_1\partial_3\tilde{\tilde{\psi}}_j)\\ \sigma_{31|j}(k_1, x_3, \omega) &= \mu(-2ik_1\partial_3\tilde{\tilde{\phi}}_j + \partial_1^2\tilde{\tilde{\psi}}_j - \partial_3^2\tilde{\tilde{\psi}}_j)\end{aligned} \tag{2.74}$$

For our application the upper layer is considered to always be a water layer. This is an acoustic layer with no shear stiffness and it is assumed no shear stresses can develop in this layer. The above equations then are simplified since $\mu = 0$ and also $\psi = 0$.

Acoustic potential

$$\tilde{\tilde{\phi}}_j(x_3) = A_j e^{-q_{pj}x_3} + B_j e^{q_{pj}(x_3 - thk_j)}, \quad q_{pj} = \sqrt{k_1^2 - k_{pj}^2} > 0 \tag{2.75}$$

Acoustic displacements:

$$\begin{aligned}u_{1|j}(k_1, x_3, \omega) =& -ik_1\tilde{\tilde{\phi}}_j\\ u_{3|j}(k_1, x_3, \omega) =& \partial_3\tilde{\tilde{\phi}}_j\end{aligned} \tag{2.76}$$

Acoustic stress:

$$\begin{aligned}\sigma_{33|j}(k_1, x_3, \omega) &= -k_1^2\lambda\tilde{\tilde{\phi}}_j + 2\mu\partial_3^2\tilde{\tilde{\phi}}_j\\ \sigma_{31|j}(k_1, x_3, \omega) &= -2ik_1\mu\partial_3\tilde{\tilde{\phi}}_j\end{aligned} \tag{2.77}$$

2.5.2 Boundary Conditions

The equations are formulated in the global coordinate system and the $Depth_j$ refers to the depth at the bottom of the j^{th} layer. There will only be $N_{layer} - 1$ depth values which must be specified since the last layer contains the halfspace which is considered to extend to ∞. The following boundary and interface conditions are applied:

- Pressure at the free surface equals zero.
  $\sigma_{33|1}(k_1, x_3 = 0, \omega) = 0$

- No shear stress can be transferred at the soil-liquid interface -shear stress equals zero.
  $\sigma_{31|2}(k_1, x_3 = Depth_1, \omega) = 0$
- Continuity of vertical stress at the soil-water interface.
  $\sigma_{33|1}(k_1, x_3 = Depth_1, \omega) = \sigma_{33|2}(k_1, x_3 = Depth_1, \omega)$
- Continuity of horizontal displacements at the soil-liquid interface.
  $u_{1|1}(k_1, x_3 = Depth_1, \omega) = u_{1|2}(k_1, x_3 = Depth_1, \omega)$
- Continuity of horizontal and vertical displacements at every soil-soil interface.
  $u_{1|j-1}(k_1, x_3 = Depth_j, \omega) = u_{1|j}(k_1, x_3 = Depth_j, \omega)$
  $u_{3|j-1}(k_1, x_3 = Depth_j, \omega) = u_{3|j}(k_1, x_3 = Depth_j, \omega)$
- Continuity of horizontal and vertical stress at every soil-soil interface
  $\sigma_{33|j-1}(k_1, x_3 = Depth_j, \omega) = \sigma_{33|j}(k_1, x_3 = Depth_j, \omega)$
  $\sigma_{31|j-1}(k_1, x_3 = Depth_j, \omega) = \sigma_{31|j}(k_1, x_3 = Depth_j, \omega)$
- No inward radiation at the infinite boundaries
  $B_{Nlayer} = D_{NLayer} = 0$

These equations form a closed system of equations with the number of unknowns and equations being equal to $2 + 4N_{soil} + 2$ or $4N_{layer} - 4$ where the first layer is an acoustic layer and the last layer is a halfspace so that $C_1 = D_1 = B_{Nlayer} = D_{Nlayer} = 0$. A Maple script was created which will generate all the equations and collect the coefficient matrix. The generated system matrices are then hard coded into a Matlab script. This is found to be much faster than generating the symbolic matrices in the Matlab function.

Chapter 3

Modal Inversion Method

This chapter treats in detail several specific aspects related to the inversion process. A short description of the inversion process will be given, but it should also be emphasized that the inversion can be considered as a general optimization problem once a few key aspects are treated carefully. The key parameter in an inversion problem is the objective function. If this is formulated in a poor or non-robust way then no matter what scheme or method is used, the results may be futile. On the other hand, a robust well-defined objective function can allow multiple methods to reach the correct result. The objective function is also called the misfit or error function and the goal of optimization is to minimize this error and thereby find the best candidate. The ideal candidate would have an objective function value of 0, although in reality this is often impossible to achieve due to noise and model simplifications. If a suitability function is used then this is the negative of the error function and often scaled so that the perfect candidate, with no error, has a suitability of 1.

The inversion of the soil stiffness profile is a non-convex problem which is expected to have many local minima [34], [10]. Therefore, a global optimization strategy must be used which can capture the global minima. The problem has an element of non-uniqueness, meaning that many different soil profiles can provide a reasonable approximation of the measured dispersion and have a objective function value that is close to the global optimum. This makes it more difficult to determine the global minima and even narrowing in on the solution could be a problem. As an analogy, imagine trying to find the lowest point in a bumpy football field, it would not be obvious where in the field it might occur and many dips might be close to the global minimum. On the other hand, a well behaved function is like a hill, there may be bumps on it but you can be sure the highest point is near the top.

The genetic algorithm initially creates a random, uniformly distributed population with the model values within stipulated search ranges. At every generation, more suitable candidates have a higher chance to pass on their 'genes' to the next generation. Cross breeding and random mutation occurs every time a new generation is born, so there is a significant amount of randomness to the search, which is what allows the genetic algorithm to find the global optimum. Specific details about the implementation of the genetic algorithm are given in Chapter 5.

Key to this process is having a robust reliable objective function. Finding the undamped or real dispersion curves is a key part of the classic modal misfit function. Finding the damped dispersion curves is essential to the damping inversion, which will be discussed in Section 5.1. Normalization of the determinant was found to be key to the chosen misfit function.

Additionally, several small topics including spectra identification, windowing, aliasing and resampling are covered which are of more relevance to the full waveform stiffness or damping inversions. They are considered in this section because they are useful for understanding the entire theoretical framework surrounding seismic inversion.

3.1 Modal Root Finding

Based on the equations given in Chapter 2, the theoretical dispersion character of a system is found as all the frequency-wavenumber combinations which lead to a zero determinant of the system matrix. The determinant equation is non-linear and in general the roots are difficult to find. Foti [10] states that the dispersion relation can only be written implicitly and is a "highly non-linear, transcendental function" which depends on the input arguments $\lambda, \mu, \rho, k, \omega$. The solution is non-trivial and the eigenvalue problem must be solved with numerical techniques. "For an elastic medium, the roots of the dispersion relations can be obtained by means of root-bracketing techniques combined with bisection. The use of the slow converging root-finding techniques is recommended by the rapidly oscillating behaviour of the Love and Rayleigh secular functions" and "requires the use of robust methods". "Determination of the roots in viscoelastic continua is even more difficult because in this case (the secular function) is a complex-valued mapping of the complex-valued wavenumber." Lai and Rix [14] state that "computing the zeros of a complex valued function of a complex variable is not trivial, particularly if the function is highly non-linear and known only numerically, as is the case for the Rayleigh secular function in vertically heterogeneous media. No general methods are available". They present a method for finding the complex roots, but this is based on complicated mathematics

and the Cauchy's residue theorem and is beyond the scope of this thesis.

3.1.1 Undamped Roots

The undamped roots are found by searching for the point where a sign switch occurs on both the real and imaginary parts of the determinant. First the determinant is computed for every grid point within the desired frequency-wavenumber domain. Then, a search is performed along a line of constant wavenumber, and the modal points are identified as the first point after (at larger frequency than) the sign of the real and imaginary parts change. Note the search direction will have an effect on the points which are found. However, generally with the fine discretization used the error on the position (due to the discrete nature of the calculation) is relatively small. However, there is a weighting effect. If we consider that the surface wave events are slow events, these have a low slope in the f-k domain and a search along constant wavenumber will cross a mode more times than a search along constant frequency as previously used [34]. Hence, searching along constant wavenumber gives a better resolution of surface wave events while searching along constant frequency results in a better resolution of the high velocity (often P-wave) modes. The position error of the modes, due to the discrete grid, is greatly reduced by refining the location of the root with a constrained local non-linear optimization function which minimizes the determinant value. It is chosen to keep the frequency constant, while the wavenumber is varied in the refinement optimization, in order to be able to compare values at the same frequency. This optimization is kept stable by constraining it to a very small search area of $+/-$ one grid step of the initial location. The Matlab function fmincon is used.

Additionally, it was found by experimenting that this approach cannot find all of the roots. At points slower than the minimum Cs velocity of the system, the imaginary part of the determinant is zero. This is explained by Section 2.2 and Figure 2.7. It can be seen in the response plots that part of the fundamental mode is not captured by the strict definition, as shown in Figure 3.1 and 3.2. The test case profiles for TC2 and TC3 are described in in Tables 4.2, 4.3 and Figures 4.2, 4.3. It is shown that this occurs both in normally (TC3) and inversely dispersive systems (TC2). Therefore, a modification of the picking criteria is used such that only the real part of the determinant is checked for a sign switch if the imaginary part of the determinant is zero and the grid location is at a phase velocity lower than the soil system minimum Cs velocity. This modified root definition is seen to capture all of the modes and will be used in all future root picking operations.

It is also interesting to note that we see more roots from the theoretical root finding than we might expect from a visual inspection of the response spectra. The

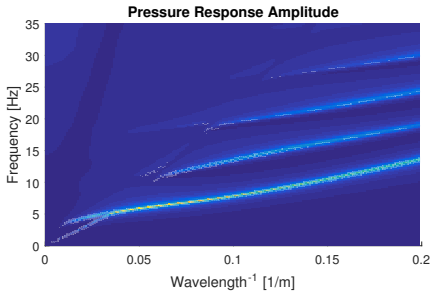

(a) Response spectra to dirac impulse for lightly damped TC2 soil profile.

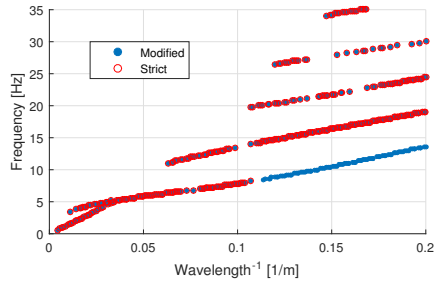

(b) Roots of determinant of undamped TC2 soil profile

Figure 3.1: Comparison of found roots with spectral response for TC2 soil profile.

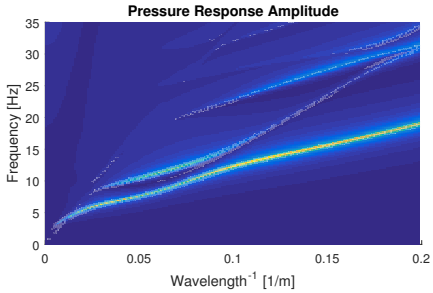

(a) Response spectra to dirac impulse for lightly damped TC3 soil profile.

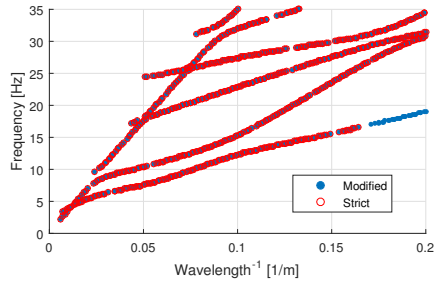

(b) Roots of determinant of undamped TC3 soil profile.

Figure 3.2: Comparison of found roots with spectral response for TC3 soil profile.

response spectra is generated using a dirac source, so it is expected to highlight everything in the f-k domain since the force is uniform. However, especially near the maximum Cs velocity of the system there is no visible energy in the response spectra. In Figure 3.2, the mode which runs straight (non-dispersively) from (0.02,5) to (0.08,30) is not visible in the response spectra. It is expected that there is a cut-off behaviour above the maximum Cs velocity where surface waves will no longer propagate because they leak and lose energy rapidly. However, the roots are still within the Cs range of the system so it is not clear why they do not show up in the spectra. This should be kept in mind for the real measurements, that there simply may not

be enough energy to activate this part of the higher modes.

3.1.2 Damped Roots

The roots of the determinant equation become complex. Hence, naively searching for roots along only the real wavenumber axis will not find any roots. Instead, the roots must be found in the complex plane. However, the roots are required at a fine resolution on the $f - k$ grid and adding another dimension to the problem, for a f, k_{RE}, k_{IM} would require computing an extraordinary number of points, and take too long. Hence, we need a smarter way to find the complex roots. Literature notes that this is indeed a complicated problem, and for high damping there are not that many satisfactory techniques. Some techniques linearize the equations to make finding the roots easier, but this error becomes large for high amounts of damping [14]. The roots start on the real axis and move deeper into the complex plane as damping is increased. However, if only a small amount of damping is applied the undamped root location can be used as a starting estimate for the location of the complex damped root. The Matlab function fminsearch and fmincon were used to find the complex roots. However, neither of these turned out to be robust and able to capture all of the roots. A function was tested which uses the argument principle, to bound the solution and locate how many poles lie within a search box. This box is then divided into pieces until the roots are singly contained within a search box. Then a particle swarm optimization is used to determine the root location. In trials, this function got stuck during the bisection phase and was terminated because it took too long to be feasible. Another approach, with the best results thus far, turned out to be using a weighted gradient based search optimization in order to follow the initial undamped root estimate to the complex root solution. This function was calibrated by noticing that the shift in the real part of the wave number is small while the majority of the shift tends to be in the complex direction. Hence, the gradient is weighted to move with a 10:1 ratio in the imaginary direction. However, this approach was still not generally able to find all of the root locations. For some points the optimization would simply diverge or fail to find a solution. In the end, the most robust solution was to use a semi-brute force approach. In this case, the soil model is incremented to the full amount of damping, and the roots are found at each of the intermediate damping steps. At each stage, the initial estimate of the root is used to define a small complex plane (the size of which is calibrated with some semi-effective non-dimensional numbers based on testing). The minima or dips of the determinant on this plane are identified and assumed to be the roots. In some instances this leads to additional roots being found, since multiple roots can fall within this small search plane when roots are closely spaced or if a numerical zero occurs (which tends to

happen at the body wave velocities of the system). The Matlab function fmincon is then used to search within a very small zone one grid-step around the found points. Multiples of roots are removed from the solution. Additionally, sometimes the numerical (not physical) roots corresponding to the body wave velocities are found, and these should be filtered out of the solution, since it is known they occur at one of the input velocities of the model.

3.2 Understanding Dispersion Curves

Low wavenumbers (long wavelengths), 'feel' deeper into the soil while high wavenumbers or short wavelengths only 'feel' the shallow soil layers and are not at all sensitive to the deeper deposits. Additionally, the phase velocity is equal to the slope in the f-k domain while the gradient of the slope gives the group velocity.

$$c_{phase} = \frac{f}{k} \qquad c_{group} = \frac{df}{dk}$$

The wave speed in (visco)elastic media is directly related to the stiffness. Hence, we can understand from Figure 3.3 that the modes are fast in the deep material and slower in the shallower material. Further since the dispersion curves vary smoothly without kinks, we can understand that this corresponds to a deposit with stiff soil deep down and soft soil in the shallow layers, and a smooth, possibly linear, variation of the properties from soft to stiff with increasing depth. Kinks in the dispersion curves are an indication of a soil stiffness profile which contains more discrete behaviour, for example, when the actual soil deposit has clear physical layering such as a layer of clay between sand.

We can further understand what is happening by investigating the mode shapes of the shear stress waves. In order to compute the surface response spectra we calculate the potential coefficients which describe the solution in all of the layers. Normally, only the coefficients from the top layer is used and the depth is set to zero so that the response at the surface is calculated. But we can also compute the response within every layer over the depth. Therefore, the mode shapes at a specific (f,k) location in the spectrum are computed by plotting the shear stress over the depth. Here it is then useful to consider three cases, as outlined in Figure 3.4. The first case, is looking at three points along the fundamental mode to see the effect of increasing the wavelength (decreasing wavenumber). The second case is at constant frequency while the third case is at constant wavenumber.

Figure 3.5 shows that the non-dimensional shape is very similar for the three points on the fundamental mode. It is well noted in literature that the depth of

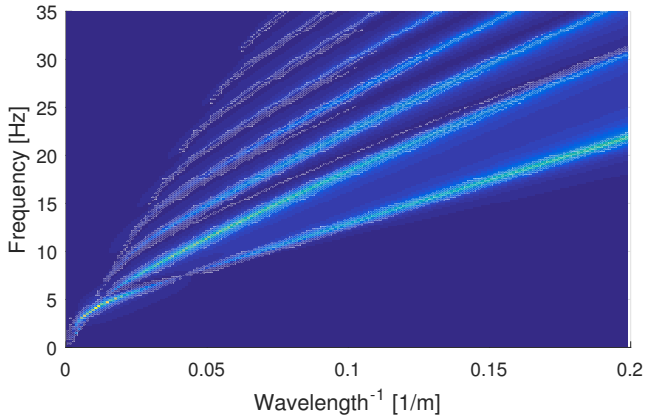

Figure 3.3: Horizontal velocity spectra for a linearly increasing stiffness profile.

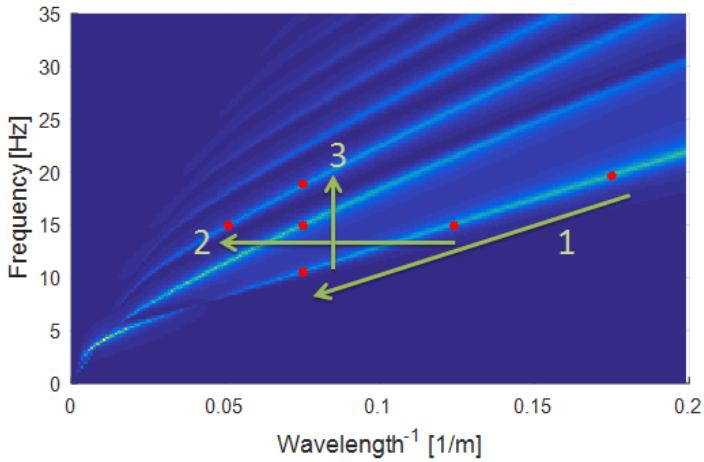

Figure 3.4: Points of response spectrum at which mode shapes are plotted showing the three cases considered.

penetration is related to the wavelength for the fundamental mode and most of the wave is contained within approximately one wavelength deep. The wavelengths corresponding to this figure are 5.7, 8.1 and 13.3m respectively. The shape corre-

sponds well to the shape given by Kramer [13] and shown in Figure 2.4. Note for homogeneous media, this fundamental mode shape is often non-dimensionalized by dividing the depth with the wavelength.

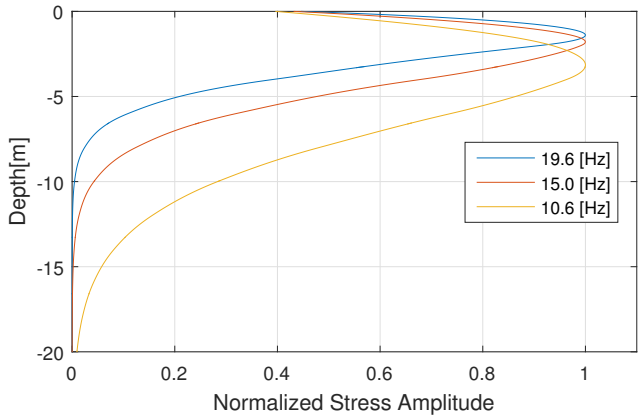

Figure 3.5: Mode shapes along fundamental mode corresponding to Figure 3.4 case 1.

The second case, Figure 3.6, plots mode shapes at constant frequency. Here, the wavelength is changing and we move to higher modes as the wavelength gets longer. Both of these are expected to increase the penetration depth of the wave. The higher modes also contain more oscillatory behaviour and the number of stress reversals seems to correspond to the number of the mode. That is, the fundamental mode is single sided, while the first higher mode has one stress reversal and the second higher mode has two.

The third case, Figure 3.7, which is the least intuitive, is what happens when the wavelength is kept constant. The wavelength for this plot is 13.3m and we see that the fundamental mode is contained within this distance. However, the higher modes increasingly feel a larger depth and the second higher mode even feels to 26m or double the surface wavelength. It is therefore clear that higher modes have deeper penetration even at the same surface wavelength. Additionally, the higher modes are proportionally more sensitive to deeper layers because a greater portion of the stress amplitude is at lower depth. Note for example that the second higher mode has much more energy between 11-24m depth than the upper portion between 0-11m.

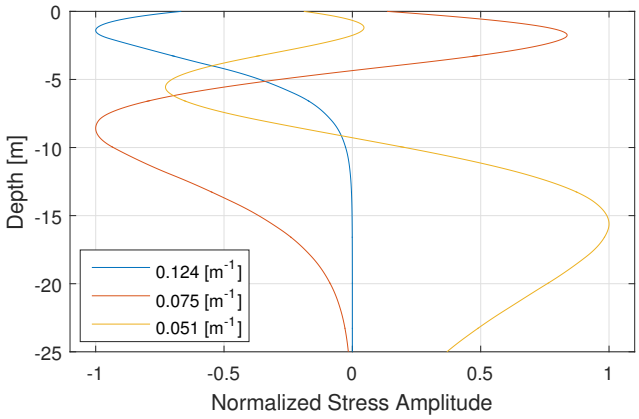

Figure 3.6: Mode shapes at constant $15Hz$ frequency corresponding to Figure 3.4 case 2.

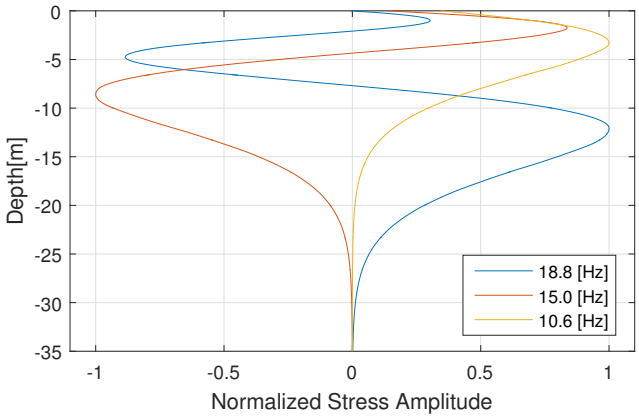

Figure 3.7: Mode shapes at constant $0.075m^{-1}$ wavelength corresponding to Figure 3.4 case 3.

3.3 Misfit Functions

In order to perform the inversion process, we must have an idea of how well the theoretical model matches the measured data. The error in the match is determined by the choice of formulation of this misfit or objective function. This inversion process then attempts to minimize this error and thereby maximize the suitability of the modelled candidate.

It is essential to determine the location of the modal dispersion curves from the measured data. Similar to a single degree of freedom system, the damped resonant frequency may be shifted from the undamped (stiffness only) natural frequency. However, with a low amount of damping this shift is quite small and could be considered negligible. For practical simplicity it is chosen that the experimental dispersion curves are identified as the peaks of the measured response.

3.3.1 Classic Misfit Function

The method proposed by [34] is an example of the classic formulation for the misfit function. It compares the distance between the theoretical and measured dispersion curves. The error from the measured mode to the closest analytic mode is found and is done per frequency trace. A schematic is shown in Figure 3.8.

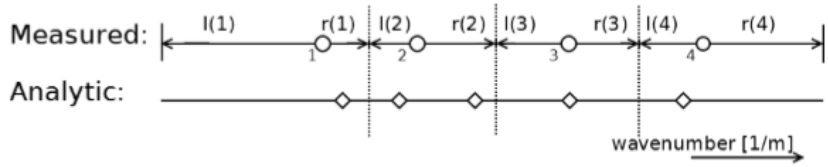

Figure 3.8: Schematic showing a possible suitability comparison between some measured and analytic modes [34].

The result is expressed by the equation:

$$Err(f) = \sum_{n=1}^{N_{modes(f)}} min[k_{meas}(n,f) - \overline{k}_{SW}(f)] \tag{3.1}$$

Where $\overline{k}_{SW}(f)$ represents all analytic surface wave modes for that frequency. To normalize the error per frequency, the maximum distance in the wavenumber domain

is calculated. From Figure 3.8, the maximum error node 1 can have is the maximum of l(1) and r(1). This means that the maximum error for frequency trace f equals:

$$Err_{max}(f) = \sum_{n=1}^{n_{freq}} max[l(n,f), r(n,f)] \tag{3.2}$$

$$\epsilon = \frac{1}{n_{freq}} \sum_{n=1}^{n_{freq}} \frac{Err(f)}{Err_{max}(f)} \tag{3.3}$$

The suitability is then calculated as:

$$suit = 1 - \epsilon \tag{3.4}$$

The disadvantage of this formulation is that the roots of the theoretical system must be found, which is computationally intensive since it involves computing the determinant at every point in the 2D f-k spectra. Further, the roots may not always be matched up in an accurate way as how one would intuitively measure their separation. That is no consistency is required so that a root which is roughly between two modes may be partially measured to one and partially measured to the other. Also, if the root finding misses any points, then a large error may be made by this distance measuring approach unless a smart way is made to interpolate the roots to ensure there are no gaps in a root measurement set. This would be easy to do if only one mode occurs but with multi-modal data the data from the theoretical root finding is unorganized and not attributed to any specific mode.

3.3.2 Determinant Misfit Function and Normalization

This objective function is based on the research of Maraschini et al [17]. The dispersion curves are identified from the measured data. This will form a set of N points containing (f,k) locations where the modes are occurring. These points are picked to be the peaks of the measured response. For the theoretical model that exactly matches the measured results, the determinant at all of these points should be zero since modes occur at zeros of the determinant equation. Hence, if the determinant is non-zero at these points where the modes occur, then this represents a misfit or an error of the theoretical soil profile. Therefore, this misfit function is simply the sum of the determinant at the modal points picked from the measured response.

$$Error = \frac{1}{N} \sum_{n=1}^{N} |M(f_i, k_i)| \tag{3.5}$$

where N is the number of points in the measured dispersion curve as picked from the response spectrum. This approach is much faster since the theoretical root set does not need be calculated across the entire f-k grid, but rather just at the points where roots have been measured to exist. Hence, instead of $500X500 = 250000$ points, perhaps only $100 - 500$ points are required resulting in an speed up $> 100X$. Additionally, the roots do not have to be assigned to a specific mode and if multiple modes come close or cross, such as with an apparent dispersion curve, then the area between them has a low determinant function value, and the misfit associated to that region is low.

The disadvantage to this approach is that the determinant function can vary by many orders of magnitude within the f-k grid. Hence, the points at low phase velocity can have a determinant that is much lower than a point which occurs very close to a root, but at a higher phase velocity. From experimenting, it was noticed the determinant function seems to drop off with some relationship to the velocity. Theoretically, this makes some sense as we can see that equations 2.31, which form the system matrix, contain an exponential term which gets exponentially smaller with decreasing phase velocity. That is the $q_s = \sqrt{k_1^2 - k_s^2}$ can also be written $q_s = \sqrt{k_1^2 - \frac{\omega^2}{C_s^2}}$ so that we see q_s is a balance between the k and ω terms. If we divide by waveumber then this term becomes: $\frac{q_s}{k_1} = \sqrt{1 - \frac{C_{phase}^2}{C_s^2}}$. As the phase velocity gets very low then q_s gets larger and approaches k and the $e^{-q_s x_3}$ gets very small. So even though we cannot conclude something in general about the determinant, we can say that the terms in the matrix get exponentially smaller with decreasing phase velocity.

It is necessary for a successful inversion with wide velocity ranges that the determinant has a similar value over the entire grid domain and only approaches zero at modal locations. Otherwise, a soil profile which puts all of the roots in the low velocity region of the model will have a very small determinant, and the inversion will therefore converge on a stiff, high velocity soil profile. A pragmatic approach, here called the '*phase velocity correction function approach*', is then suggested for normalizing the determinant. This involves determining the relationship between phase velocity and the model determinant value (away from the mode). This is done by computing the determinant on several (usually 3) testlines which trace arcs in the f-k domain. Figure 3.9 shows the determinant spectra with 3 testlines. Note that the determinant is plotted to the power of 0.3 in order to make it more visible because hardly anything is visible when only the absolute value of the determinant is plotted. A radial pattern where the testlines are discretized at uniform angular spacing was chosen. However, the radial distances are chosen randomly to be between

$25-100\%$ of the distance from the origin. These testline distances are randomized to avoid the situation where the theoretical soil profile coincides in such a way with the testlines that it receives an unfairly favourable normalization (resulting in a lower determinant value). However, that means the determinant norm alization process is not entirely determininstic which may be unfavourable for repeatability during the inversion process. This assumption should be tested with the inversion process and a choice made if it is better to use fixed radial test locations.

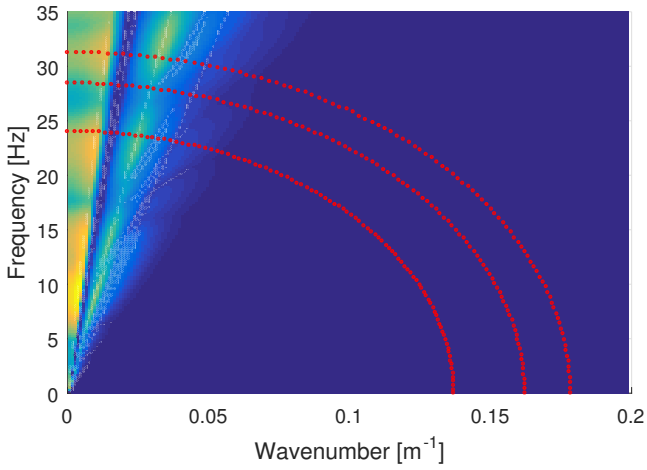

Figure 3.9: Testlines plotted on un-normalized determinant raised to the power 0.3

Figure 3.10 shows the raw determinant computed along the test lines. Since the modes cross the testlines at different points, the relationship of determinant vs theta is slightly different. Hence, the three testlines are averaged to form one estimate of the determinant-velocity relationship, which is less dependent on the modes which can cross these testlines. This line is then smoothed to further remove the effect of the determinant dipping to zero at the modes. A variety of smoothing methods were tested. In the end a moving average smoothing function was the most robust as some other methods could result in negative scaling factors in the low velocity region seen in Figure 3.10. It is known that the moving-average method is sub-optimal and it consistently cannot follow the steep drop-off of determinant in the low phase velocity region, leading to an underestimated scaling factor. However, the resulting low determinant region is much smaller than before, and much closer to the value in the rest of the grid, so it is quite acceptable. The dips at the modes are

very localised and only a small number of samples are required for computing the average. Testing resulted in a choice of 5 samples over which the moving average is calculated. Keeping this value small helps the normalization to reach a more uniform value, but without smoothing at all we would run the risk that we scale out the very modal dips in the spectrum that we are interested in. Averaging 3 lines also helps to avoid that we can remove a modal dip with the normalization.

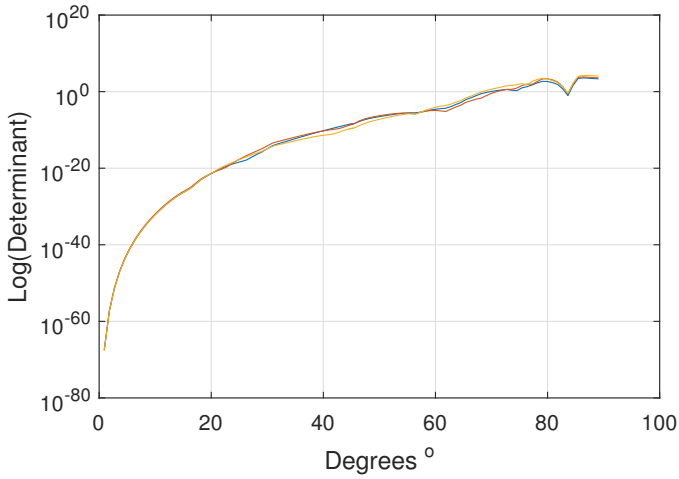

Figure 3.10: Un-normalized determinant vs angle in the f-k spectrum, where 0 degrees begins on x-axis and increases counter-clockwise.

The determinant at every point in the f-k domain is then normalized by using the found determinant-velocity relationship. The Figure 3.11 shows that the normalization is successful for this system of 1 water layer, 8 soil layers and a halfspace. This normalization approach is very pragmatic, and was found to be very effective in allowing the inversion to progress to the correct solution while being able to specify a wide search velocity range. Although, this method is fairly effective and the normalized determinant has a value 1 between modes, the exact value is not precisely determined and will vary a bit with the number of layers in the model (or size of the determinant matrix). Therefore, for the inversion the suitability is normalized by the mean of the suitability of the starting, completely random, population. It is then expected for a successful inversion that the mean of the objective function (or suitability) for the population will start at 1 and decrease until some small value where it levels off, indicating that the solution has converged. The best member of

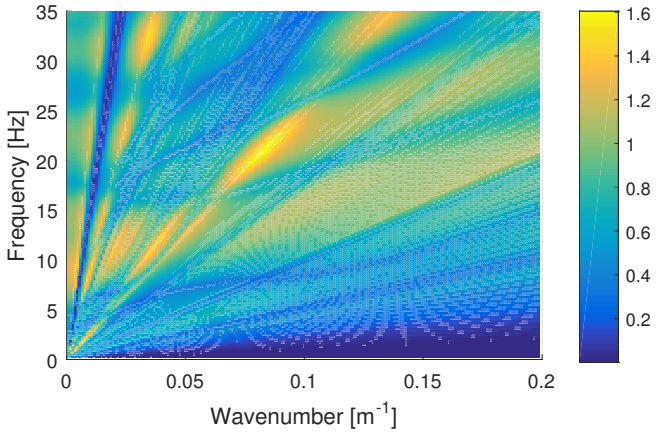

Figure 3.11: Determinant spectra after normalization with the phase velocity correction function approach.

the population, with the lowest objective function value, should follow this general trend as well, but can certainly increase in some generations because of the genetic mutations and cross-breeding meaning that the best sample may be 'destroyed' in a given generation.

3.4 Timing Comparison

The vast majority of the time in one run of the inversion is taken for creating the system matrices and evaluating the inverse since it must be done at every point. In testing with Matlab it is found to account for $80 - 95\%$ of the entire run time. A timing comparison was made between Fortran and Matlab for generating one response spectra for 1023X1024 grid points for a soil system with water, 8 layers and a halfspace, as used by [4] in the full waveform inversion process. The Fortran code of [34] was used while the Matlab code was programmed by the author. It was found that with a serial run in Fortran it took 0.8Gb of memory and 20.9minutes to generate the response, with 1 core of an intel i5-4300M CPU of 2.60GHz. While Matlab automatically used 2 cores, 0.6Gb of memory and the run time was 22.5minutes. Hence, for equivalent runtime the Matlab code took 45minutes. This means that the Matlab runtime is approximately twice as long as the Fortran code. Without

implementing parallelization, the two codes run at almost the same speed. Given the greater degree of difficulty and complexity of debugging and coding in Fortran and the practise of post-processing with Matlab, the author proceeded to code everything in Matlab. This also allows a clean start, rather than modifying the Fortran code of [4], which is already a modification of the code of [34]. Further, there are many very useful Matlab functions and documentation accessible which puts a lot of capability within close reach and also gives the potential to make the code easier for others to understand if more standard functions are used.

3.5 Notes about full waveform inversion

There were various challenges encountered for using the full waveform inversion to identify the stiffness profile [4]. Although, the full waveform process will not be used in this report, the author wishes to make some comments which may assist further attempts with the full waveform inversion process. Additionally, some comments are provided for a deeper and not entirely intuitive understanding about signal collection in relation to windowing and Shannon-Nyquist limits.

3.5.1 Source Spectra

The full waveform response spectrum is dependent on the choice of source. As noted, the method used for removing the source dependency is not entirely source independent due to the stabilization factor [4]. Therefore, an attempt was made to identify the source spectrum. One simple and very rough way to identify the source spectrum is to first transform the measured data to the f-k domain and then at every frequency to average the amplitude across all wavenumbers. This results in a source spectrum which is roughly equivalent to the spectrum identified by Ingmar. Figure 3.12 shows a comparison of the source identified by Ingmar, the source identified by the method described above and the source used by Ingmar in the full waveform inversion process. This shows that it is likely the source differs significantly from the source spectrum used, with two clear peaks in the response at $5Hz$ and $13.5Hz$, while the Ricker wavelet used for the inversion had a peak at 20Hz. Hence, even if the source profile is roughly Ricker shaped, it should be centered between these frequencies or a multi-peaked source spectrum could be created by combining multiple ricker wavelets. This may allow the full waveform inversion to find a better match and also to make the theoretical profiles visually much closer to the measured profile.

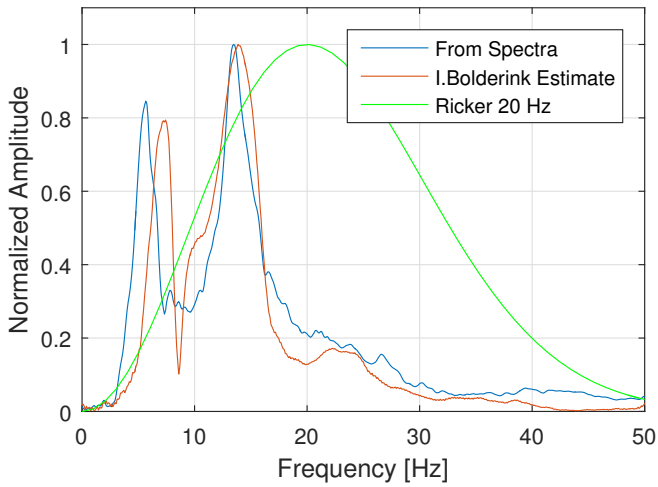

Figure 3.12: Comparison of the identified source signal with the Ricker pulse previously used for full waveform inversions.

3.5.2 Windowing

For a useful reference about discrete collection and windowing see [26]

Linear time invariant operations on the time signal are equivalent to multiplication by a transfer function on the fourier domain spectrum, that is they change the magnitudes or angles. Any other operations will create new frequency components that can be referred to as leakage in a broad sense [33]. The window function introduces spectral leakage, where when we take the fourier transform of the signal, the energy becomes spread around the frequency where it actually occurs at. The spreading is a characteristic of the window used and is generally a trade off between the reduction in height of the peaks and the width of the main lobe. The rectangular window is the simplest window and is often used in transient analysis to avoid attenuating energy from the impulse inducing a shift in the energy distribution of the spectrum.

First, let us understand the effect of windowing in 1D, then we can easily understand this concept in 2D where the principles are the same. When we measure a time domain continuous signal at a point, we immediately introduce two effects.

First we perform continuous time truncation of the true signal - or a multiplication with the rectangular/boxcar window function. That is, the signal is captured everywhere within the measurement window (multiply by 1) and nowhere outside of the measurement window (multiply by 0). Secondly, we perform discrete data sampling, which is represented with a multiplication by the dirac comb function. This is 1 at multiples of the sampling period and zero in between. The effect of the dirac comb is that we sample the continuous time or frequency domain signal at discrete points. The points that we sample are dependent on the length sampling period and will result in a spectrum resolved at multiples of $df = \frac{1}{T}$. In the case when the measured signal frequencies are exact integer multiples of the sampling spectrum resolution, there is no effect of windowing. This is seen more clearly by diving into the mathematics and recalling the convolution property where a multiplication in the time domain is a convolution in the frequency domain.

$$f(t) \times g(t) = F(\omega) * G(\omega) \tag{3.6}$$

where the convolution integral is given as:

$$F(\omega) * G(\omega) = \int_{-\infty}^{\infty} F(\omega)G(\Omega - \omega)d\omega = \int_{-\infty}^{\infty} F(\Omega - \omega)G(\omega)d\omega \tag{3.7}$$

The rectangular window function is the sinc function in the frequency domain. If $g(t)$ is the boxcar function of period T, then it can be shown that

$$\begin{aligned} \int_{-\infty}^{\infty} g(t)e^{i\omega t}dt = G(f) &= \frac{sin(\pi fT)}{\pi fT} = sinc(fT) \\ = G(\omega) &= \frac{sin(\frac{\omega}{2}T)}{\frac{\omega}{2}T} = sinc(\frac{1}{2\pi}\omega T) \end{aligned} \tag{3.8}$$

It can be proved using L'Hopitals rule that $sinc(0) = 1$ and that the zero crossings occur at multiples of the periodic frequency $df = \frac{1}{T}$. If $f = n\,df = \frac{n}{T}$ then $sinc(fT) = \frac{sin(n\pi)}{n\pi})$ and if $n = 1, 2....$ then $sinc(fT) = 0$.

A harmonic is can be expressed in the frequency domain

$$\int_{-\infty}^{\infty} e^{i\Omega t}e^{i\omega t}dt = F(\Omega) = \delta(\omega - \Omega) \tag{3.9}$$

If we perform multiply the harmonic signal f(t) with the rectangular sampling window g(t), we can perform this as a convolution in the frequency domain and

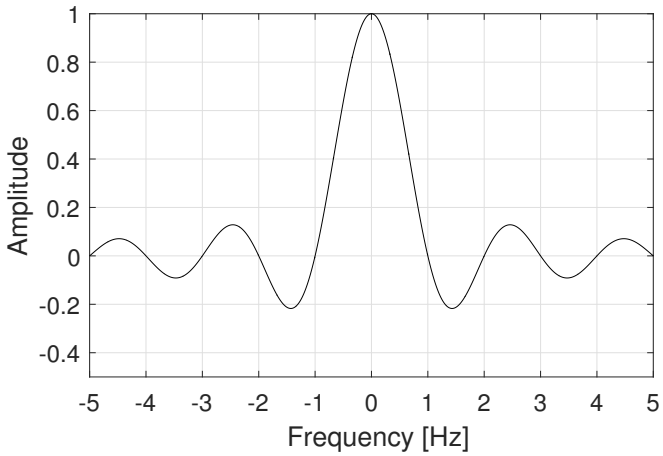

Figure 3.13: Sinc function of 1s rectangular window in frequency domain.

obtain a shifted sinc function.

$$F(\Omega) * G(\Omega) = \delta(\omega - \Omega) * \frac{sin(\frac{\omega}{2}T)}{\frac{\omega}{2}T} = \frac{sin(\frac{(\omega-\Omega)}{2}T)}{\frac{(\omega-\Omega)}{2}T} \tag{3.10}$$

This mathematics is still considering a continuous time signal. If we now move to a discrete definition we can use the dirac comb to represent sampling. The fourier transform of the dirac comb sampling function again returns the dirac comb in the frequency domain.

$$\int_{-\infty}^{\infty} III_T(t)\, e^{i\omega t} dt = df\, III_{df}(f), \text{ where } df = \frac{1}{T} \tag{3.11}$$

So we multiply $f(t) \cdot g(t)$ with $III_T(t)$ in order to obtain the sample data. This operation is again represented by a convolution in the frequency domain. Convolution with the dirac comb has the effect of 'copying' the shifted sinc function to every point of the dirac comb. Note that the function is mathematically continuously defined, although we are trying to represent discrete sampling. Therefore, we should only consider the points in the frequency domain which are sampled when we compute our discrete fourier transformation. These are multiples of $df = \frac{1}{T}$. Therefore, we can actually reduce this convolution operation to a multiplication with the Dirac

comb in order to make it more clear which points are considered in the frequency domain.

Spectral leakage is then associated with the points at which the Dirac comb samples the shifted sinc function. The sample period is always an integer multiple of the timestep. That is $T = n\Delta t$ and this both defines the sinc function $sinc(\frac{1}{2\pi}\omega T)$ and the dirac comb $III_{\frac{1}{T}}$. Therefore, what determines if spectral leakage occurs is the sample period, T, and the frequency of the sampled signal, Ω. It can be expressed $\Omega = \frac{n}{T} = n\, df$. If n is an integer, then the dirac comb samples the shifted sinc function at exactly the zero crossings and the peak point. If n is not an integer then, the shifted sinc function is sampled not at these points and there is spectral leakage.

To demonstrate this visually, we consider a sampling window of 1s then, the periodic frequency associated with this window is $df = 1Hz$. We see the fourier transformed version of the rectangular sample window in Figure 3.13. The zero crossings of the sinc function indeed occur at integer multiples of the sample period frequency $df = \frac{1}{T} = 1[Hz]$.

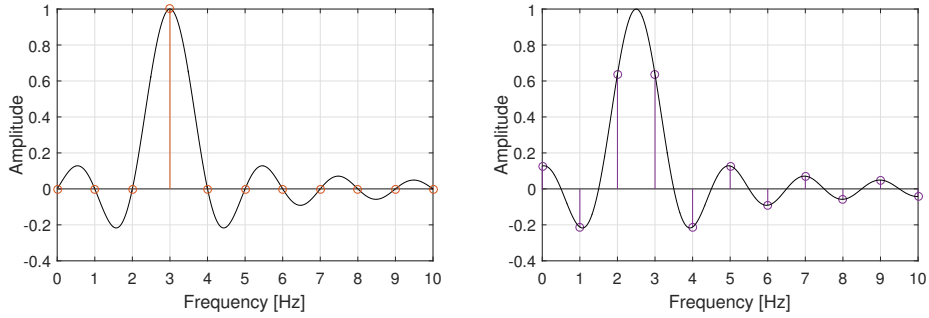

(a) Integer sampling - no spectral leakage occurs.

(b) Non-integer sampling - spectral leakage occurs.

Figure 3.14: Dirac comb discrete sampling.

The continuous spectrum associated with sampling this is the convolution of this function with the sinc function, which results in a shifted sinc function, shown in black on Figure 3.14a. When the discrete sampling is considered, we only get information at the orange marks shown. This is considering a sample window of 1s and a frequency of 3Hz, so three periods fit exactly within the sample window. However, if we consider a harmonic signal with 2.5Hz and the same sampling window, we see that there is spectrum leakage as shown in Figure 3.14b. There is not an integer

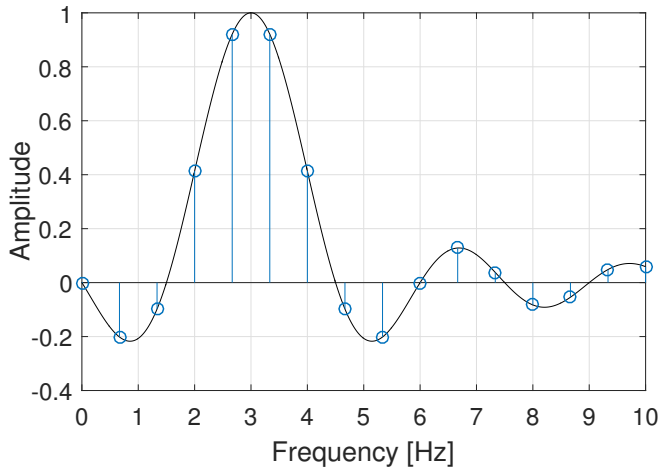

Figure 3.15: Dirac comb discrete sampling of a 1.5s rectangular window.

number of periods and the sampling points do not line up with the crossings of the sinc function or with the main peak.

This can also be shown, if we consider the same 3Hz harmonic signal, but consider a different sample period of 1.5s. The sinc function is wider this time, and the associated sampling frequency resolution is smaller with $df = \frac{1}{1.5} = 0.67[Hz]$. Again, the harmonic signal is not an integer multiple of the frequency resolution and so the sampling results in leakage as shown in Figure 3.15

Note, that real signals consist of many frequencies, and the frequency spectrum can often be described by a continuous function, so many frequency components experience spectral leakage due to windowing. Therefore, it can be said that practically, discrete samples are always affected by spectral leakage due to windowing.

Note also, that the FFT windowing technique [4] first starts with discrete frequencies. Therefore, it may not be subject to windowing in the same manner as a measured data, especially if the truncated length of the array fits an integer multiple of times into the virtual array which is computed.

3.5.3 Nyquist-Shannon Sampling Limits

The Nyquist-Shannon sampling theorem states that the minimum sampling frequency required is double the highest frequency in the signal. This can also be stated that

the Nyquist or maximum frequency which can be measured is half the sampling frequency or that at least two measurements must be made within one wavelength or period considering harmonic signal components.

$$f_{nyquist} = \frac{1}{2\Delta t}$$
$$k_{nyquist} = \frac{1}{2\Delta x} \tag{3.12}$$

However, stated this way is not actually entirely correct. In fact, aliasing can be used in compressed or sparse sampling of signals in order to extract information above the Nyquist frequency. What the Nyquist-Shannon theorem states is more that only signals up to the Nyquist-Shannon frequency can be recovered with perfect fidelity, since at higher frequencies the signal becomes undistinguishable from a lower frequency. This is shown in Figure 3.16. However, if other constraints are known,

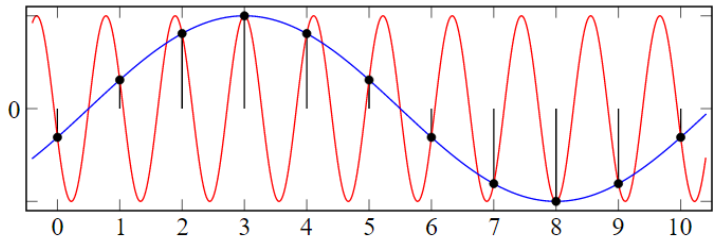

Figure 3.16: Example of aliasing due to an undersampled high frequency component compared with a well sampled low frequency[32].

then this energy can be recovered. In the case of space data and wavenumbers, we actually know that the data occuring at higher frequencies cannot be attributed to the corresponding lower negative frequencies. This is because we have selected our measurement array so that it only contains wave propagation in one direction and a negative frequency would correspond to a wave propagation in the opposite direction. This assumes that the amount of reflected energy is very minor and no reverse propagating waves exist. Using this knowledge, the spectrum can be extended to double the nyquist frequency and all of the energy in the negative spectrum can be recovered.

3.5.4 Implementation of Discrete Transforms

The continuous forward Hankel transformation of order n is given:

$$\tilde{f}^{H_n}(k_r, x_3, \omega) = \int_0^\infty \tilde{f}(r, x_3, \omega) r J_n(r k_r) dr \tag{3.13}$$

While Fourier transformations may be computed with fast fourier transformation techniques, no similar method exists for uniformly spaced data. An exponential grid can be used in order to utilized the Mellin connection which allows the Hankel transformation to be computed with a regular FFT algorithm [12]. However, our data has been collected on a uniform grid and a discrete direct numerical integration will be used. The discrete form of the Hankel transformation, considering rectangular integration for one fixed frequency is:

$$\tilde{f}^{H_n}(k_r) = \sum_{j=1}^{N} \tilde{f}_i(r_j) r_j J_n(r_j k_r) \Delta r \tag{3.14}$$

N is the length of the radial position vector, r. This integral is computed for every wavenumber at which we wish to obtain the solution. This is one benefit of direction integration over fast transformation techniques, that we can compute the transformed variables only at the specific wavenumbers which we desire them. Given a grid vector in the wavenumber domain, of length M, then we can define the integrand matrix $I = r_j J(k_{r|i})$ of dimensions MxN. This is precomputed by determining all of the values for i=1...M and j=1...N. This integrand matrix can be used for all the integrations on a grid of the same size and the entire integration simply becomes a matrix multiplication operation as shown below.

$$\tilde{f}^{H_n}(k_r) = I \tilde{f(r)}' \tag{3.15}$$

In this equation $\tilde{f}^{H_n}(k_r)$ is a column vector of length M, I is the integrand matrix $r J_n(r k_r)$ as computed above and $\tilde{f(r)}'$ is the data vector to be transformed, which is transposed to be in column format for the matrix multiplication.

Since this integration is computed for discrete data, rectangular integration is used. It can be shown that the accuracy is very close to trapezoidal integration, since it is only the first and last integration point which are modified in trapezoidal integration. Additionally, higher orders of integration, such as Simpsons rule, do not give an increase in accuracy except for the start and end integral terms. This is because we have discrete data and cannot evaluate the function value at intermediate points. A short refinement study was performed to determine the resolution

required for an accurate discrete transformation. The reference case of $\Delta x = 0.01m$ was used. The error is plotted relative to the values computed with this finest refinement level. It is found that the error behaves linearly as shown in Figure 3.17a. A resolution level of $dx = 0.2m$ seems to be sufficient, with an error of just over 0.2%. The run time for all of these cases was not significant, when compared with the time required to generate a full grid response.

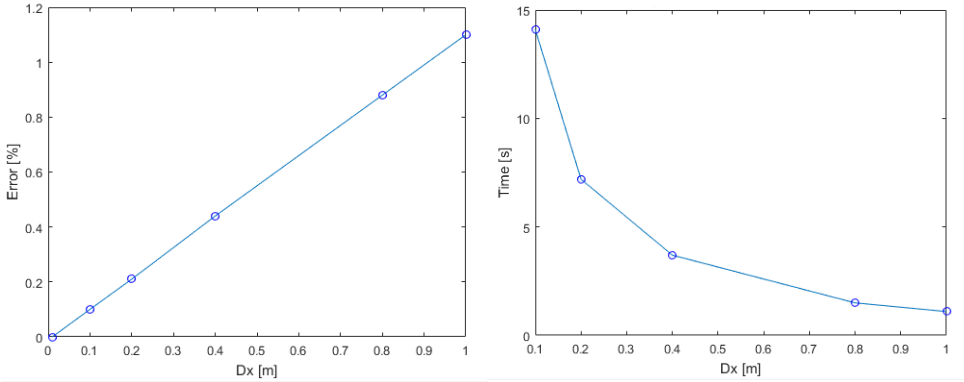

(a) Accuracy of direct Hankel transformation vs the spatial step size.

(b) Speed of direct Hankel transformation vs the spatial step size.

Figure 3.17: Results of direct Hankel transformation refinement study.

3.5.5 Resampling to finer grids

The physical measurements are collected on relatively coarse grids. Although the 1m spacing is more than sufficient to capture the high wavenumber content, the resolution may not be good enough to perform reliable discrete transformation calulcations. Hence, we require the data on a finer grid. This can fairly easily be done by first converting the data to the frequency domain using a fast fourier transform (FFT in Matlab). Then, the data is padded with extra trailing zeros and the inverse fast fourier transformation is taken. This will result in the data on a grid with a finer spatial sampling. This is a physically accurate way to interpolate harmonic functions. Of course, we expect that our functions are actually Bessel functions, so this is not a completely valid approach since the interpolation uses harmonic functions. However, in practice this method seems to achieve very good results.

Chapter 4

Model Studies

The theory behind wave propagation, generating system matrices and finding modal dispersion curves has been covered in Chapter 2 and Chapter 3. This chapter aims to understand the model further by investigating how various properties or choices affect the location of the dispersion curves and hence, to understand the limitations or implications for the inversion process.

4.1 Sensitivity to damping

We wish to be able to estimate the in-situ stiffness and damping parameters. These could be estimated from a combined inversion, but it would be more robust if the estimation could be decoupled whereby the stiffness is first estimated and then the damping is estimated. During the modal inversion process, the root locations from the measured data must be identified. They are taken to be the location of the peaks in the measured response spectra. However, this does not directly correspond to the location of the undamped roots of a system with only stiffness.

It is known for a single degree of freedom mass-spring-damper system that the damped resonant frequency differs from the natural frequency, especially as the damping becomes large. The relationship for a system with viscous damping is $\omega_{res} = \omega_{nat}\sqrt{1-2\zeta^2}$. For the layered soil system it is not possible to derive such a simple expression for the effect of damping on the modal location, so it will be investigated numerically. It is important to know how the damping affects the location of the dispersion curves, since the location of the dispersion curves dictates the stiffness found by the inversion process. If we assume that the stiffness inversion is

damping independent, how big is the error that we make by identifying the modal locations as the resonant peaks of the damped system? Is a decoupled inversion an acceptable assumption to make or would it introduce a large error on the stiffness?

In order to study this effect four model cases were used. A normally dispersive soil profile is one where the stiffness and shear wave velocity increases with increasing depth, while an inversely dispersive profile gets weaker with depth. The first test case, TC1, is normally dispersive and consists of a 5m water layer, a 5m soil layer and a halfspace with the Cs velocity profile shown in Table 4.1 and Figure 4.1. The second test case, TC2, consists of a 5m water layer, two 5m soil layers and a halfspace where the halfspace is weaker than the layer above as shown in Table 4.2 and Figure 4.2. The results for TC2 should be interpreted carefully since this case is not thought to be very representative of what happens in reality and would be quite a rare situation. The third test case, TC3, shown in Table 4.3 and Figure 4.3 is a profile with a water layer, three soil layers and a halfspace, where there is a velocity inversion in the layers but the overall profile is normally dispersive. While the last test case, TC4, is the profile which was determined as the best result from full waveform inversion [4] and contains a water layer, 8 soil layers and a halfspace and has the profile shown in Table 4.4 and Figure 4.4.

Table 4.1: Properties for TC1 soil profile.

Layer	Thickness [m]	Cp [m/s]	Cs [m/s]	ζ_p	ζ_s	$\rho[Mg/m^3]$
Water	5	1500	0	0	0	1.0
1	5	1000	100	0.05	0.05	2.0
Half-space	∞	1000	200	0.05	0.05	2.0

Table 4.2: Properties for TC2 soil profile.

Layer	Thickness [m]	Cp [m/s]	Cs [m/s]	ζ_p	ζ_s	$\rho[Mg/m^3]$
Water	5	1500	0	0	0	1.0
1	5	1000	75	0.05	0.05	2.0
2	5	1000	300	0.05	0.05	2.0
Half-space	∞	1000	150	0.05	0.05	2.0

The complex roots are found using the methods outlined in Chapter 3. As noted, this process is not entirely robust. The complex roots are difficult to find and in some parts the roots may not be found without a clear reason why, but due to divergence of the solver or some other reason. The determinant equation is noted for being

Table 4.3: Properties for TC3 soil profile.

Layer	Thickness [m]	Cp [m/s]	Cs [m/s]	ζ_p	ζ_s	$\rho[Mg/m^3]$
Water	5	1500	0	0	0	1.0
1	3	1500	100	0.01	0.01	1.8
2	3	1500	200	0.01	0.01	2.2
3	3	1500	100	0.01	0.01	1.8
Half-space	∞	1500	400	0.01	0.01	2.3

Table 4.4: Properties for TC4 soil profile.

Layer	Thickness [m]	Cp [m/s]	Cs [m/s]	ζ_p	ζ_s	$\rho[Mg/m^3]$
Water	4.4	1450	0	0	0	1.0
1	2.0	1500	98	0.03	0.03	1.9
2	0.6	1450	53	0.03	0.03	1.5
3	0.7	1600	50	0.03	0.03	1.0
4	5.3	1650	405	0.03	0.03	2.0
5	1	1700	617	0.01	0.01	2.0
6	6.5	1700	180	0.01	0.01	2.0
7	3.3	1600	365	0.01	0.01	2.0
8	1.2	1600	334	0.01	0.01	1.8
Half-space	∞	1600	884	0.01	0.01	2.0

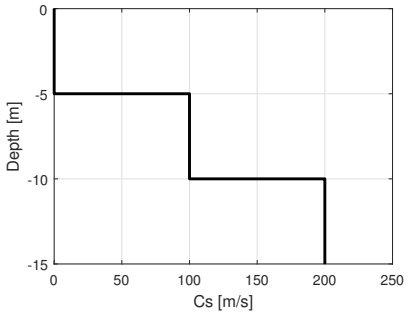

Figure 4.1: Cs velocity of TC1 soil profile.

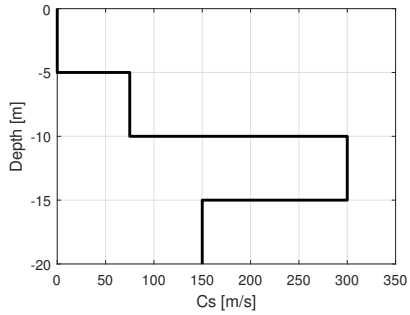

Figure 4.2: Cs velocity of TC2 soil profile.

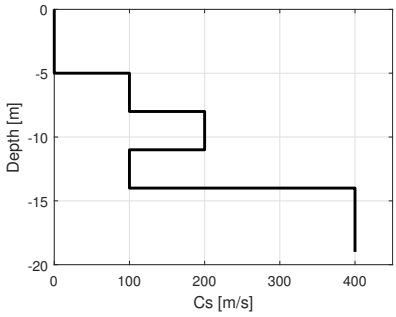

Figure 4.3: Cs velocity of TC3 soil profile.

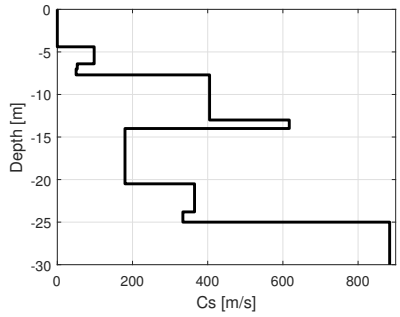

Figure 4.4: Cs velocity of TC4 soil profile.

difficult to solve in literature [10], [14]. However, the general sensitivity trends can certainly be determined. For the comparisons we project the roots into the real plane and take only the real part of the wavenumber. This is also what happens with the measurements if we pick the dispersion curves directly from the peaks of the spectra.

Figure 4.5 shows for the cross section of the TC1 spectra how the roots are varying in the complex plane for a cross section of the spectra taken at 35Hz. The poles start on the real axis with zero imaginary part and then move downwards into the complex plane as damping is applied while the real part of the wavenumber is slowly decreasing in magnitude. At the points of the poles the determinant is zero and hence these look like dips in the surface of the determinant on the complex plane. The points represent increments of $\Delta\zeta = 2.5\%$ for a total range of damping ratio of $0 < \zeta < 25\%$

For TC1, Figure 4.6 shows how the modes vary with soil damping ratio. It can be seen that the wavenumber decreases as damping increases and that it seems to vary in quite a smooth manner. The pole migration from TC2 is shown in Figure 4.7. There are unintuitive patterns in some locations where the dispersion curve moves to the increasing wavenumber. A cross section of the spectra, showing the pole migration on the complex plane is shown in Figure 4.8 which shows the strange behaviour where the modal roots can migrate to higher wavenumbers when damping is increased and also a new pole appearing which has a high imaginary part. This behaviour is unexpected since it means that increasing a damping decreases the velocity of the wave. Typically, since damping adds to the overall magnitude of the force resisting motion, it has a similar effect to increasing the stiffness in that it promotes a shift to a stiffer, faster wavenumber. This case has a weak halfspace

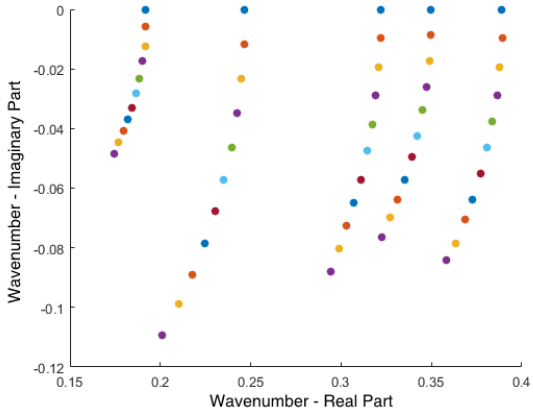

Figure 4.5: Pole migration on complex plane at 35Hz, from $0 - 25\%$ in steps of 2.5%, with the undamped roots having zero imaginary part and the poles migrating from top to bottom as damping increases.

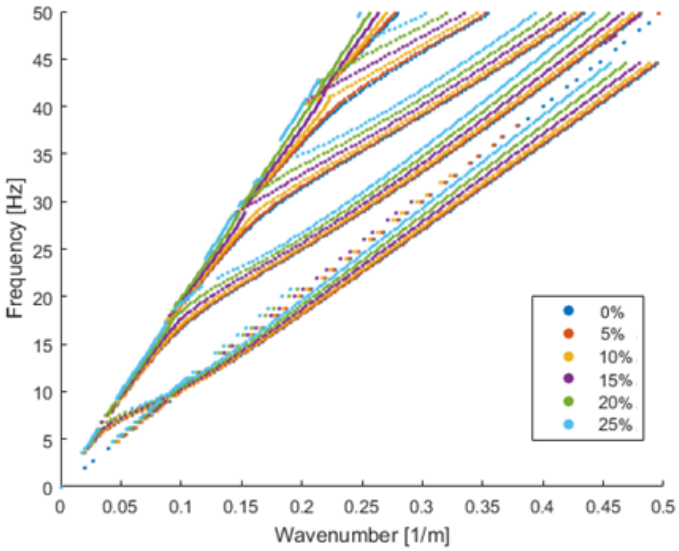

Figure 4.6: Dispersion curve migration under the influence of increased soil damping ratio for TC1 soil profile.

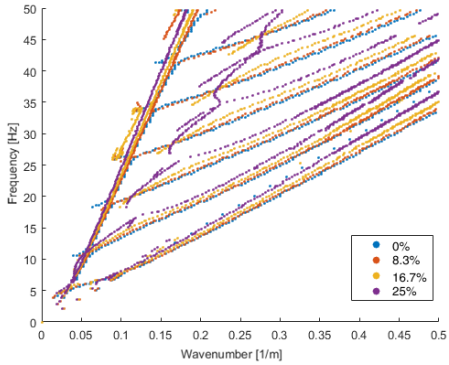

Figure 4.7: Dispersion curve migration under the influence of increased soil damping ratio for TC2 soil profile.

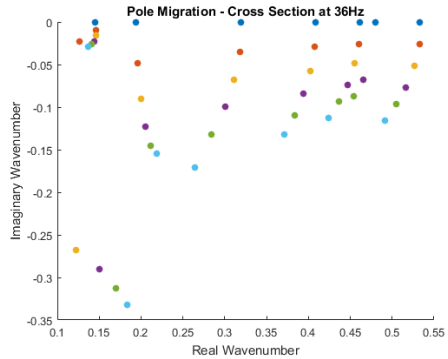

Figure 4.8: Complex plane pole migration for TC2 soil profile at 36[Hz].

with a stiffer layer on top and is thought to be unrepresentative of reality, occurring very rarely if at all. Therefore, little emphasis is placed on these results, and no conclusions are drawn from TC2.

The migration of the modes for TC3 is shown in Figure 4.9 which again displays the same trend that the real part of the wavenumber is decreasing with increasing damping. Similarly, TC4 shows the same pattern of mode migration as the other normally dispersive cases, although the amount of 'missing' modes where the root finding strategy has not been able to find the complex roots is increasing. The author believes that this is because at these locations the roots become imaginary more rapidly and deviates further from the initial guess. Hence, the roots cannot be found. This possibly also indicates that these roots would be less likely to appear in the real data, because if they have a larger imaginary component then they will decay faster and less energy will make it to the measured spectrum.

The data is aggregated for test cases 1,3 and 4, where the percentage shift of the roots for all of the found roots in the 2D spectra is calculated. Figure 4.11 shows the trend that the shift is fairly consistent and predictable and the shift is relatively small for the expected range of soil damping ratios of $0 - 10\%$. Within each of the datapoints in this figure, there is of course a distribution around this mean point which is shown on the graph. However, the author verified by checking histograms of the percentage shift that representing it by the mean is valid. Although, in hindsight, it would have been nice to include standard deviation bars around this mean values.

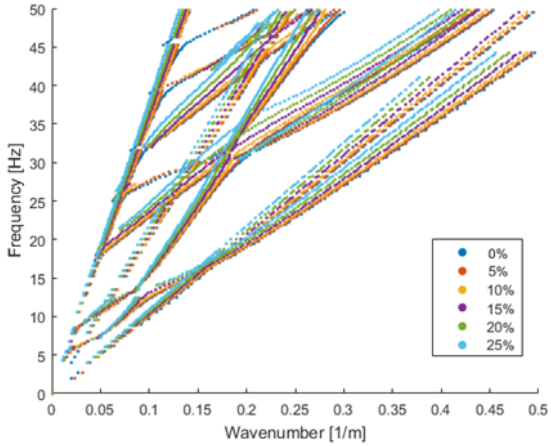

Figure 4.9: Dispersion curve migration under the influence of increased soil damping ratio for TC3 soil profile.

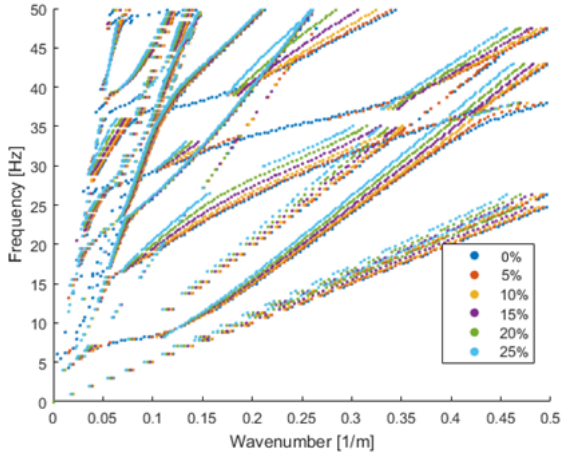

Figure 4.10: Dispersion curve migration under the influence of increased soil damping ratio for TC4 soil profile.

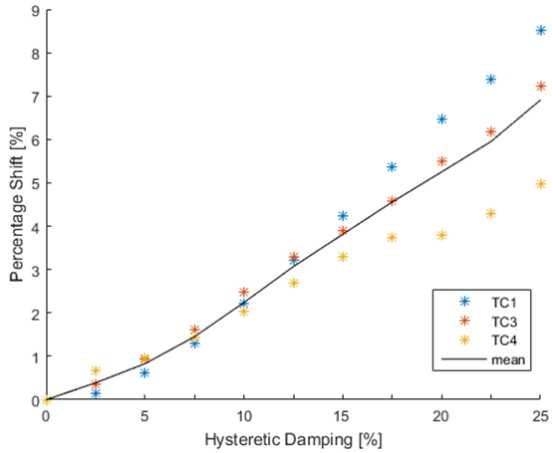

Figure 4.11: Summary of percentage shift in wavenumber due to change in soil damping ratio.

Further, we cannot say from this graph alone what error a 2% shift in the location of the wavenumber due to a 10% soil damping means in terms of the error for the stiffness estimation. Therefore, the next section investigates the model sensitivity in order to put these results on the sensitivity of the modal damping locations into better context.

Tests were also completed to determine the relative sensitivity of the P-wave and the S-wave damping, since in the general model these can be specified differently. However, the tests were conclusive that the S-Wave damping dominates the model and the P-wave has a very small effect. Therefore, it is recommended to use one combined value of the damping, so that the P-Wave and S-Wave damping values are the same.

Additionally, tests were done for a viscous damping assumption. However, it was very difficult to find the complex roots, especially at higher frequencies. This is because the amount of damping applied is very large at higher frequencies when compared with the hysteretic damping. Hence, it is recommended to use hysteretic damping since it is also noted by researchers that damping in soils is not dependent on frequency for seismic waves [19]. It may also be possible that the real frequency dependence of the damping can be identified from the measured data.

4.2 Sensitivity to model properties

The idea of this section, is to develop an understanding about the sensitivities in the layered soil system model. This is important for understanding the level of confidence we can have in an inverted estimate and also to determine which parameters are important for a successful inversion. Here one model parameter value in one layer is varied by either $+/-5\%$ while all of the rest are kept fixed. The new roots and dispersion curve locations are calculated and then the mean shift in wavenumber from the baseline case is computed. The sensitivity from the $+/-$ cases are combined and the figures show the total change in wavenumber for a 10% shift in the model property in that layer. It is well noted by literature that the surface wave propagation is most sensitive to the shear wave velocity profile of the soil [34], [10] and [13]. We can calibrate our expectations about the sensitivity by considering the case where the Cs velocity of all layers is simultaneously changed by 10%. Then, this has the effect equivalent to scaling the axis and given that $C = \frac{\omega}{k}$ we can rearrange so that we see a 10% increase in the Cs velocity results in the wavenumber shifting to $\frac{1}{1+0.1}$ for the same ω. Hence, a 10% increase in Cs velocity results in a 9.1% decrease in wavenumber and a 10% decrease in Cs velocity results in a 11.1% increase in the wavenumber.

Figures 4.12, 4.13 and 4.14 show that the modal locations are most sensitive to the Cs velocity and fairly sensitive to the thickness of the layer. The other parameters have a very low sensitivity. The model also seems to be more sensitive to the near surface layers than to deeper layers. The sensitivity of the model to the layer thickness is relatively higher than suspected, which indicates that this could be a confounding parameter for the inversion. That is, if the incorrect layer thicknesses are chosen in the initial model then the inversion will have difficult to converge to the correct soil profile. Additionally, given that the CPT measurements only sample a very thin column of the soil, there is quite a high probability that the thickness of the layers identified from the CPT measurements would not be exactly the layering over the entire surface array if the site has a significant amount of lateral variability. This would then suggest that it could be beneficial to perform a joint inversion of the Cs velocity and layer thickness, so that the inversion process is not hindered by an unrepresentative initial guess for the model layering. Of course, this increases the amount of parameters to be estimated in the inversion process and would increase the length of the inversion process since the search domain size is increased by including additional parameters.

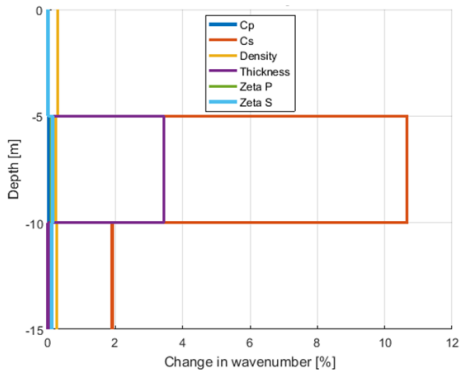

Figure 4.12: TC1 modal location sensitivity to model parameter variations.

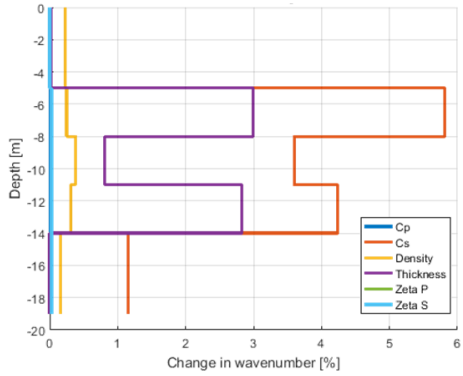

Figure 4.13: TC3 modal location sensitivity to model parameter variations.

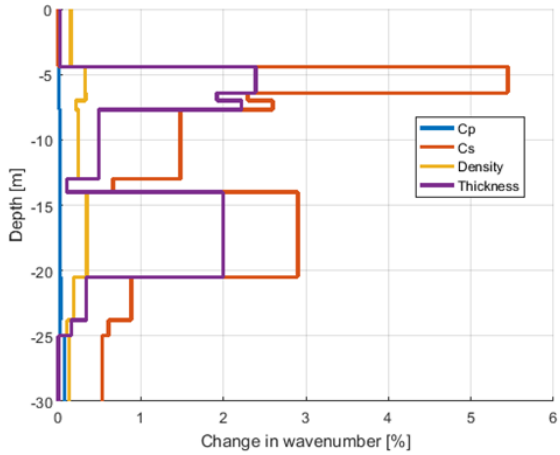

Figure 4.14: TC4 modal location sensitivity to model parameter variations.

4.3 Layer Splitting

This section attempts to address the question - what happens if one of the layers in the model is split into two layers, both with a property variation? Or said another way, what is the effect of averaging two layers into one thicker layer. Hence, in

this section a specific property and model layer is chosen and two soil variants are created by splitting this layer into two layers of equal thickness and in one variant the top layer will have a property variation of $+10\%$ and the bottom layer will have -10% while in the other variant the top layer will have -10% and the bottom will have $+10\%$. This test is only performed on TC3 and TC4 and note that the water layer is not plotted in this case, so that the depth starting at zero is measuring from the seabed. From the Figure 4.15 and TC3 we get the clear idea that splitting layers is more has a much bigger effect the closer it is to the surface. It is not clear from Figure 4.16 what the pattern is of splitting the first layer but it is very interesting to note from the right figure the pattern given by the roots of the variants resulting from splitting the second layer. The third mode past the kink at $17Hz$ and $0.05m^{-1}$ is the only part of the dispersion curve that is clearly affected by splitting the second layer. From Figure 4.17 it can be seen that the effect of splitting layers is also important for thick layers, although, in this model which already has more layers, the effect of splitting any layer has a smaller impact on the overall dispersion curves. It is interesting to see from Figure 4.18 that both for the first and sixth layers, which are shown because they have the highest sensitivities, that the effect of splitting the layer is localized to a specific part of a mode or modes. In the case of the first layer, splitting it has the big impact on the fundamental mode between wavenumbers of 0.05 and 0.15 m^{-1} and for the second mode for wavenumbers above the kink just after 0.05 m^{-1}. The sixth layer has a very localized effect where the only visible change in the root locations occurs for the fourth mode. This could be an important tool for an experienced user who wishes to use intuition to improve the inversion algorithm. For example, if the best inversion candidate has a mismatch only at a specific place, it may be possible that this requires a splitting of one of the model layers in order to allow the model to vary the roots in that specific way without affecting the other parts of the roots which may already be correct. It is a challenge how to effectively incorporate the findings of the effect of layer splitting and is likely to have to be evaluated on a case by case basis if layer splitting would improve a modelled result and which layer is the correct one to split.

4.4 Layer Discretization

From the study on layer splitting we already have an indication that the resolution of the near surface layers is important for the correct prediction of the dispersion curve locations. This intuitively makes sense if we consider that the higher wavenumbers and smaller wavelengths have a smaller lengthscale and therefore, the non-dimensional layer resolution is worse for small wavelengths because the wave

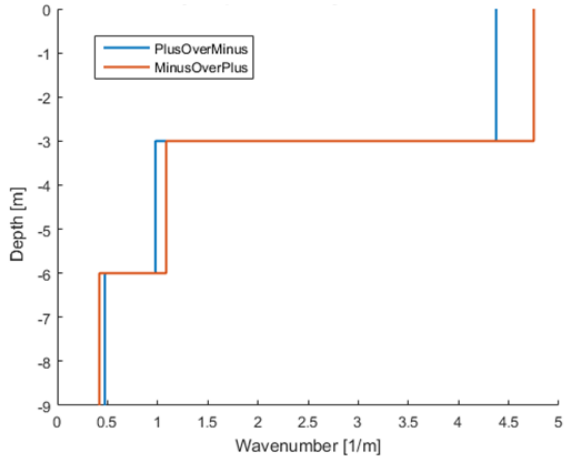

Figure 4.15: TC3 modal location sensitivity to soil layer splitting.

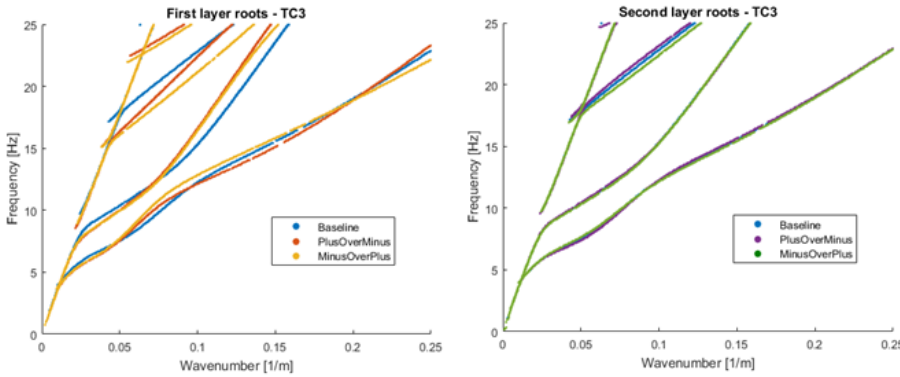

Figure 4.16: TC3 modal root locations for baseline soil profile and splitting of layers 1 and 2.

samples fewer layers than a longer wavelength would.

For this two test cases are considered. The first case is a linear soil profile, which varies from a Cs of 100 to 900 m/s over 32m of depth and then remains constant in the halfspace as shown in figure 4.19. The second case is a profile with a velocity inversion which varies linearly between a Cs of 100-400-200-500 with turn points in

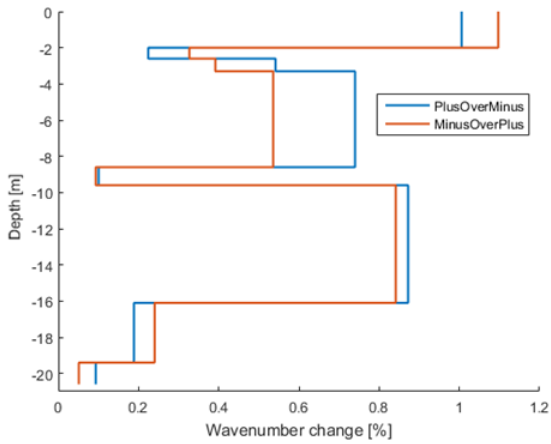

Figure 4.17: TC4 modal location sensitivity to soil layer splitting.

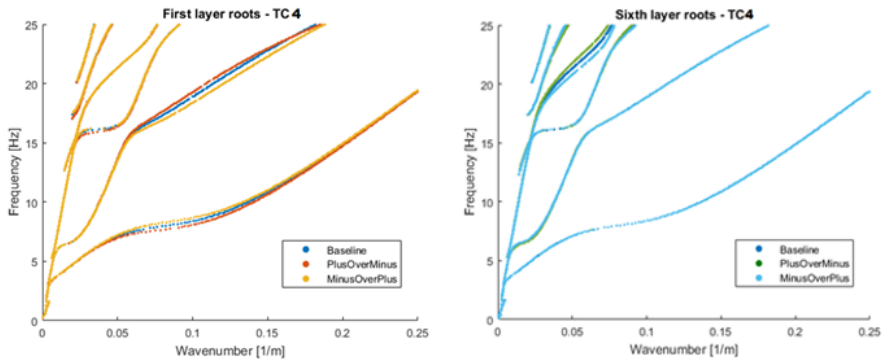

Figure 4.18: TC4 modal root locations for baseline soil profile and splitting of layers 1 and 6.

the profile at 8, 16 and 24m of soil depth as shown in figure 4.21.

Figure 4.19 shows the discretizations for layer sizes of $\Delta x = 1, 2, 3$. The difference between $\Delta x = 1$ and $\Delta x = 2$ is fairly small. There is a definite shift in the location of the first and second higher modes above the fundamental mode, especially this difference is larger at higher wavenumbers. This makes sense, since the higher wavenumbers or shorter wavelengths reach a smaller depth and are more

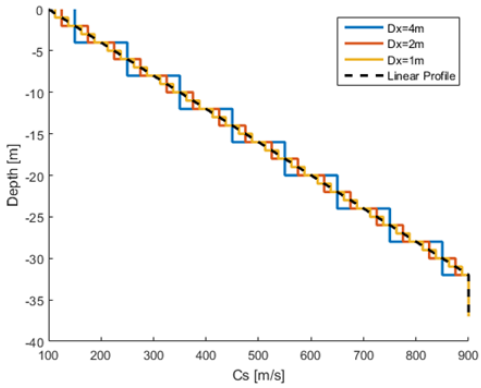

Figure 4.19: Discretization of linear Cs profile.

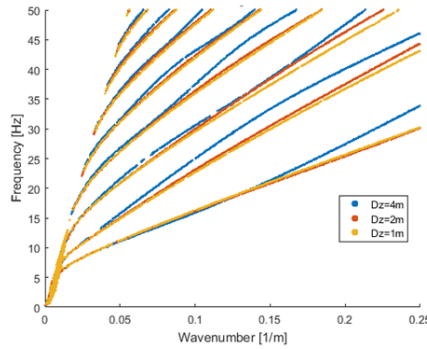

Figure 4.20: Dispersion curves of linear Cs profile.

affected by the discretization. The $\Delta x = 4$ is not fine enough to capture the correct dispersion behaviour. These roots are far away from the $\Delta x = 1$ root locations. This makes sense because the smallest wavelength is $4m$ corresponding to $k = 0.25$. The model resolution should be at least $2 - 4$ times as small as the smallest wavelength which is considered.

Figure 4.22 shows a similar pattern to the linear case. This time the discretizations plotted are $\Delta x = 1, 2, 3$. Both the $\Delta x = 2$ and $\Delta x = 3$ cases seem to have root locations which differ significantly from the $\Delta x = 1$ case. Even a model discretization half the size of the smallest wavelength is not sufficient to accurately predict the roots. A resolution of at least 4 times smaller than the smallest wavelength is recommended. Possibly even smaller discretization would be beneficial if the computational expense is permissible. It is clear that the discretization is very important to the theoretically predicted modal dispersion curves in linearly varying soil deposits. For both test cases the results with even larger discretizations have been omitted, since the dispersion curves are even much more erroneous and the diagrams become chaotic.

4.5 Implications for Inversion

This section aims to pull together the model studies conducted in this chapter and draw some conclusions about what this implies for the inversion process.

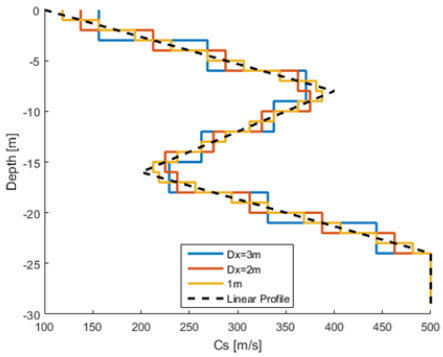

Figure 4.21: Discretization of linear Cs profile with velocity inversion.

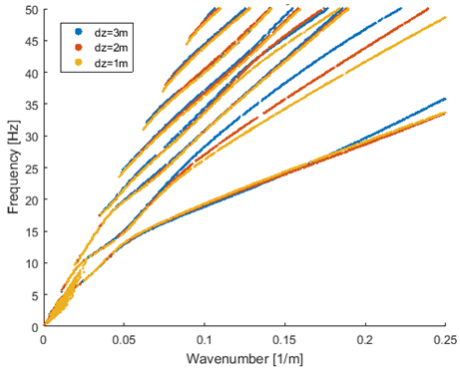

Figure 4.22: Dispersion curves of profile with velocity inversion.

- Damping has a predictable impact, causing a smooth shift in the modal root locations. For a damping up to 10%, the shift in the real part of the wavenumber is approximately 2%. This is considered to be acceptably small in order to use a decoupled inversion approach. If damping inversion indicates a high level of damping, an iteration or correction to the soil stiffness profile could be performed in order to achieve more accurate results.
- The dispersion curves are highly sensitive to the shear wave velocity, especially near the surface. However, it is also fairly sensitive to the chosen layer thicknesses and an incorrect a-priori choice may be a confounding parameter for a stiffness inversion.
- Averaging two layers into one layer, or splitting on into two, has a high impact if the layer was near the surface. Additionally, thick layers also influence the results. The effect is found to be relatively localized (to one mode or to specific small frequency and wavenumber ranges of the modes) on the dispersion curves and it is possible an experienced user could identify how the model layering should be changed in order to improve the fit of a model.
- Discretization of the layers and the thicknesses chosen are very important to the predicted dispersion curve locations. This was probably the most significant finding from the model studies and indicates that a finer resolution should be considered in the models than was previously used for the full waveform inversion.

- Deposits which have continuously varying soil deposits have smooth dispersion curves while kinks or sharp bends in the dispersion curves are indicative of a more discretely layered soil deposit with jumps in the shear wave velocity profile.
- Higher modes have higher sensitivity to deeper layers, as was seen from splitting the deeper layers into two.
- The S-wave damping ratio controls the amplitudes of the spectral response and the P-wave damping ratio has almost no effect. Therefore, it should be sufficient to use one damping ratio, assuming that the P-wave damping ratio is the same as the S-wave damping ratio.
- Assuming viscous damping makes the roots very hard to predict at higher frequencies because the amount of damping applied, compared with hysteretic damping, is very large. Hysteretic damping should be used, although if possible, the actual frequency dependency of the damping should be identified from the data.

Chapter 5

Modal Surface Wave Inversion

In the inversion process, the goal is to find the soil properties that make the forward model best match the measured results. Usually, a subset of the parameters is chosen to vary in order to match the results. Parameters such as the density or poisson ratio are generally not inverted for since they tend to fall within a relatively narrow range [13] and therefore have less influence on the solution. It is also shown in Chapter 4 that there is a low sensitivity to the density and compression wave velocity. The modal solution can be assumed to be independent of the damping in the system as also shown in Chapter 4. Hence, the goal of the modal surface wave inversion is to determine the shear wave velocity without the damping influencing the results. Later on the damping will be estimated.

5.1 Inversion via a genetic algorithm

The layered soil model forms a complicated system and it can be expected that local minima occur in the objective function of the optimization problem. Hence, the algorithm should be able to handle the local minima and find the global minimum[34]. Therefore, in our research we adopted a global optimization method, being the genetic algorithm. However, some researchers have also used conjugate gradient optimization for inverting for the damping ratio from a suitable starting estimate [3]. It is also possible that a hybrid model could achieve a more efficient inversion process. However, this is left for further research.

The location of the modal dispersion curves is identified from the measured data using a semi-automated GUI that the author programmed. This tool allows the pick-

ing of the peak energy points from the measured spectrum but requires the user to verify that erroneous points, due to noise in the response spectrum, are not included in the pick. There is also the option to pick the roots completely manually, which relies on an experienced person to interpret the measured spectrum and to pick the dispersion curves. The implementation of the genetic algorithm follows closely with the process used by [34] with some practical changes that increase the flexibility of the algorithm and allow the possibility of more ways to tune the inversion for a more successful or faster result. Additionally, the suitability or objective function implemented is the determinant based suitability, as discussed in section 3.3.2.

The genetic algorithm breeds a random initial population that is uniformly distributed within the defined search ranges for all of the properties and layers that are allowed to vary. The suitability function is calculated for every member of the population. The suitability defines how well the trial solution fits the observed measurements. Then, in the default case, 1/3 of the population is chosen via tournament selection to act as the 'parents' that pass on their characteristics to the next population. In the actual implementation, the 6 random members from the population are automatically allowed to pass on their genes in order to keep a little more randomness in the population. The tournament selection chooses a random selection of candidates from the yet unselected population and then holds a tournament whereby only the best candidate from this subset is selected into the parent population. This promotes more variation than simply choosing the best 1/3 of the entire population by allowing some random chance that a less suitable profile may be passed on.

Once the parent population is selected, then the new population is bred. The first 1/3 is an exact copy of the parent population, the next 1/3 uses the top n layers from the parent population and takes the rest from a random parent, where n is a random number of layers that varies for each candidate. The last 1/3 keeps the bottom n layers and takes the rest from a random parent, where n is again a different random number for each candidate. Additionally, an option is included where a specified number of the best candidates that have ever occurred can be included in the child population. This will decrease the genetic variability, but may help allow the algorithm to converge better by avoiding the situation where the best candidates are lost due to either mutation or cross breeding.

Lastly, the entire child population is allowed to mutate based on some specified probability. So each of the properties in each of the layers will generate a random number and if it is within the probability of mutation then the value will be replaced with a uniform randomly selected value within the search range. Experience with test cases suggested that the full mutation that is uniform randomly distributed over the search range has a low success range in the new generated candidates. So the algorithm was tweaked to allow two kinds of mutation. The first is the original full

mutation that allows the new property to be anywhere within the search range. The second is a small mutation where the property is random uniformly picked from a range of $+/-10\%$ around the starting property value. When included this allows the candidates the possibility to vary themselves on a finer scale to improve their fit. Only one type of mutation is allowed per layer property, so the small mutation is additional to the full mutation and increases the genetic variability.

Some other improvements include dynamic re-ranging, layer stripping, phased settings and run interrupts. The dynamic re-ranging was found to have a big positive impact on the inversion process without adverse side-effects. The dynamic re-ranging allows the search ranges to be automatically adjusted as the inversion progresses. This allows for a wide search range to be specified at the beginning of the inversion but accomplishes that the algorithm naturally reduces the ranges to avoid computing useless profiles and wasting guesses far away from the global minima. At every generation specified, for example at every 10th generation, then the best certain fraction of the population, say 15%, is taken. The maximum and minimum values of the properties for each of the layers in this subset of the population is then computed. These are set to be the new search ranges. Although it may be unnecessary, there is a relaxation factor provided on this to avoid the situation where the ranges would shrink too quickly.

The second feature that is helpful in some inversions is layer stripping. Since the objective function is most sensitive to the near-surface layer properties, then the near-surface layers can overwhelm the successful estimation of the deeper properties. Hence, as the inversion progresses, the layers near the surface are progressively turned off, allowing the deeper layers to be estimated with more confidence. This is seen to work very well in synthetic cases where the algorithm can converge to the correct solution in the top layers and then move on to deeper layers. However, there is still the question if it is a good choice to make for the real measurements, since we may end up locking in an error on the upper layers if the algorithm has not correctly determined them due to the non-uniqueness of the problem.

Thirdly, the settings are phased, which allows for a new set of mutation probabilities or any other setting to be introduced after N generations. This includes the ability to introduce a different rootset such that the inversion algorithm is initially using only the fundamental mode and after N generations it can switch to using a root set that contains all the modes for computing the suitability. There is also the ability to specify weights between different roots, so that if three roots sets are loaded, for example the fundamental mode and the two higher modes, then a specified weighting between these modes can be given to the suitability function.

Finally, the last important modification is the option to interrupt a run in a smooth way by changing a setting in a text file in the run folder. This allows the

run to be terminated early if convergence is reached or if the user wishes to view the results urgently. After every generation the program also computes statistics for the population, so that the progress of the inversion may be monitored. The best 5 profiles are plotted at each generation to get a visual on how the profile is progressing, although usually the user will not be observing the inversion process. In the future a smooth restart capability could also be added such that the user could truly steer the inversion process by altering some settings.

5.2 Synethetic Data Inversion

In order to first verify that the inversion process is working, it was tested on a synthetic case. It was decided that profile TC3, shown in Table 4.4, would be a good benchmark since this is a relatively difficult profile with the sharp jump in velocities. For the first run the default same mutation probability used by [4] of 25% was used and none of the other new additions to the program such as dynamic ranging and layer stripping were used. The resulting Cs velocity profile obtained is shown in Figure 5.1. This already shows very good agreement with the initial input profile and the convergence is rapid so that this case was only run for 20 generations.

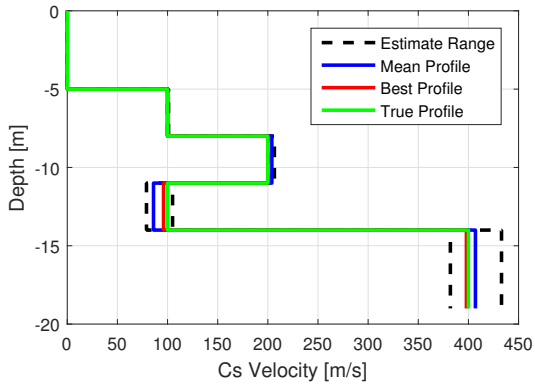

Figure 5.1: Result of Cs inversion on the synthetic dispersion curve of the TC3 soil profile using default inversion parameters.

In testing, the main feature that was able to improve the convergence of the inversion profile to better match the true profile was layer stripping. After every 5 generations the top active layer is turned off. This results in a very good estimate of

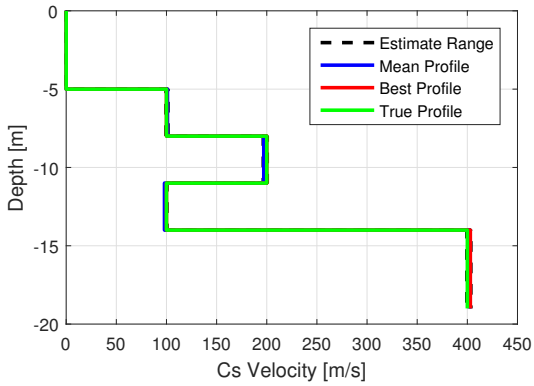

Figure 5.2: Result of Cs inversion on the synthetic dispersion curve of the TC3 soil profile using layer stripping.

the soil profile, as shown in Figure 5.2, with good convergence characteristics shown in Figure 5.3. Due to the layer stripping process we have fixed in a small error in some of the upper layers because they were turned off before they fully converged to the correct solution. However, the benefit can clearly be seen for the lower layers; the stiffness of the lower layers is predicted within a much narrower range.

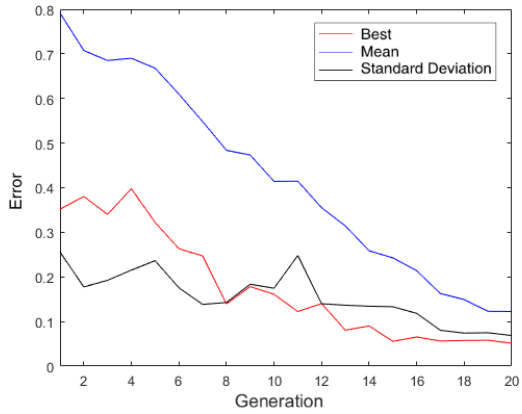

Figure 5.3: Error convergence for Cs inversion on the synthetic dispersion curve of TC3 soil profile curve using layer stripping.

5.3 IJsselmeer Stiffness Inversion

The collection and processing of the IJsselmeer data from the W27 turbine of the Westermeerwind wind farm will be discussed. Then 4 different stiffness inversion cases are presented, which use a combination of different inversion settings and different dispersion curve interpretations.

5.3.1 Collection and Processing

The difficulties with collecting the data meant that only one good dataset was obtained and this was for the hydrophones. No useable data was obtained for the geophones. The measurement array consists of 48 sensors spaced at every 1m. The array was placed stationary and centred over the location where the wind turbine would be installed while the source was moved so that shots were performed at several distances from the start of the array. The accuracy of the positioning system was low and the shots were performed at a $\sim 15^o$ angle to array. Hence, the array spacing was scaled to account for this. The results were concatenated into one virtual array of longer length and this combined shot record is shown in Figure 5.4. There are some gaps in the data and several traces had to be removed due to unexpected jumps in the amplitude. In order to reconstruct a clean dataset, a sparse Radon

transformation [27] was used to decompose the shot record into a minimum number of linear and parabolic events. Hence, a reconstructed virtual shot record, which represents a 'clean' version of the actual shot record, is created. This is shown in Figure 5.5. It is important to note that the start of the shot record has a large impact on the spectrum, but several different choices can be made on how to extrapolate the record to one that starts at the origin. Theoretically, the amplitude is infinite at the origin since it is a point source. However, a more practical approach was taken where the extrapolated amplitude is finite. The validity of the record is questionable in this region, where there are many near-field effects and wave development taking place. More details on the pre-processing, scaling and radon space reconstruction can be found in [4].

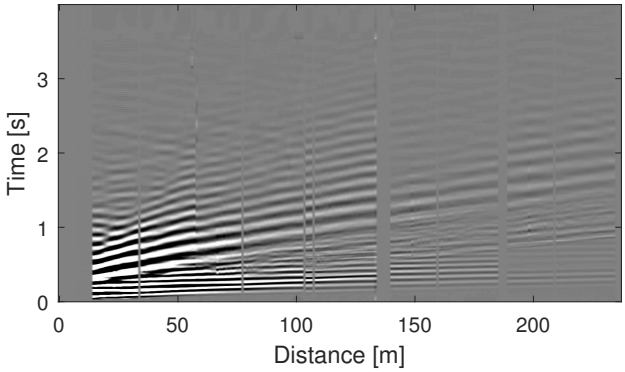

Figure 5.4: Concatenated shot record from the IJsselmeer data.

Since the taking the Fourier or Hankel transform of the data results in the same modal root locations, the FFT is taken for the stiffness determination for convenience. If the FFT of the data is taken then the resulting spectrum is very unclear. Previously, RMS scaling of the amplitudes at each sensor (spatial) location was performed. The benefit is that this increases the influence of the far-field effects. Additionally, windowing was simultaneously performed with a Tukey window. Testing by the author indicated that the primary reason for the windowing further clearing up the spectrum is the further reduction of the near-field effects. However, windowing redistributes the energy by introducing new frequencies. Therefore, it is preferable to simply truncate the sensor traces near the start of the array and ignore the data it carries. The separate effects of RMS scaling, truncation and windowing before the Fourier transformation are shown in Figures 5.6, 5.7, 5.8 and 5.9.

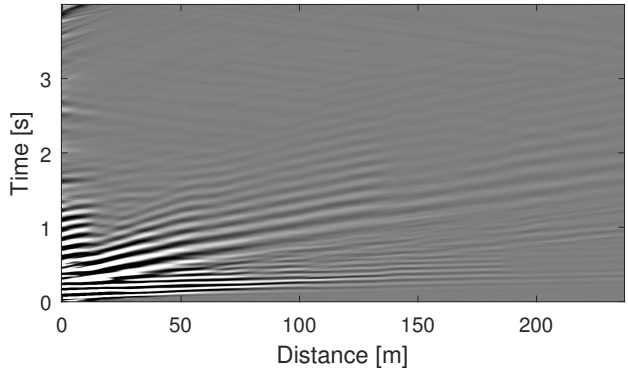

Figure 5.5: Concatenated and pre-processed shot record for the IJsselmeer data.

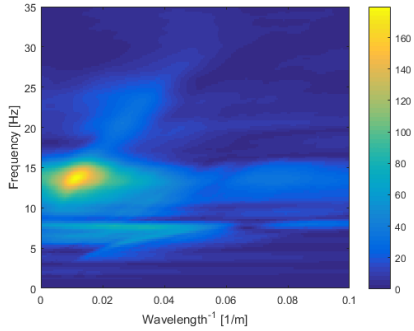

Figure 5.6: F-K spectrum of the raw IJsselmeer data.

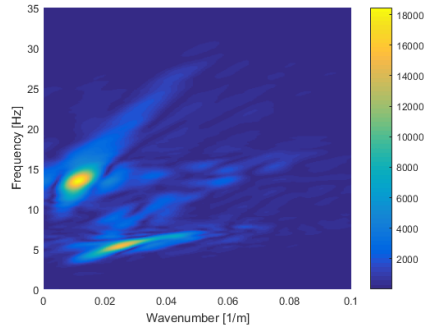

Figure 5.7: IJsselmeer spectrum after application of RMS scaling and Tukey windowing.

Due to timing considerations and for consistency, the modal root locations were picked from the spectrum as produced by RMS scaling and Tukey windowing the first and last 100 traces. The root locations in this spectrum are not fully clear and there are features of the spectrum that are not easily explainable. Especially the large blob of energy occurring at wavelengths of 70-120m or wavenumbers $0.008 - 0.015m^{-1}$ and 13.5Hz. The phase velocity associated with this event is very high, 1200-1500m/s and it occurs at a low wavenumber. If this is a propagating mode it implies that there must be a stiff deep layer of at least 1200m/s shear-wave

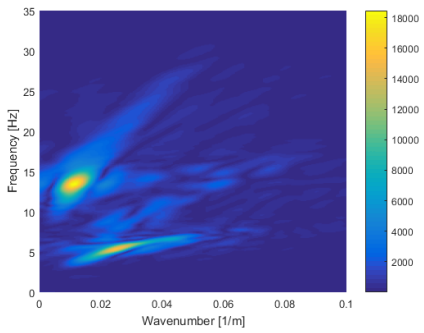

Figure 5.8: IJsselmeer data spectrum with only RMS scaling.

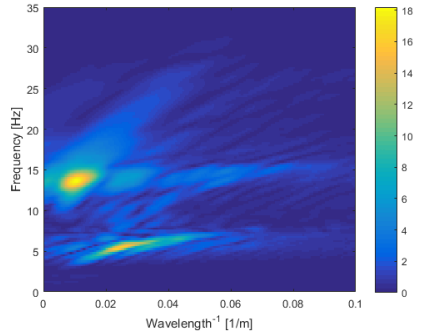

Figure 5.9: IJsselmeer data spectrum with first the 70 data traces discarded.

velocity, since propagating surface wave modes do not exist above the maximum shear wave velocity of a system. Consultation with Fugro [23] indicates that indeed it is likely that there is a layer of bedrock at 60-100m depth since the Appelscha rock formation[5] is known to be present in this area. There is also energy that appears to even touch the y-axis at zero wavenumber. This could be caused by a zero-group velocity mode [11] or could be caused by smearing of the data due to the truncation effect. This high energy event could be associated with some form of stationary or resonating soil behaviour. We know there is a stiff layer at 30m, since none of the CPT measurements were able to measure past this depth and the sensor force spiked off the scale. Further, the borehole sample shows that there is gravel layer at 30m depth. Hence, this high energy event could be associated with a full wavelength resonance down to the bedrock at 60-100m (although the author considers it unlikely that the source has enough energy to resonate such a large soil layer). Otherwise, it could be a resonance of the soil above the stiff layer at 30m, which would correspond to approximately one quarter of a wavelength. It could also be due to a direct wave arrival of the P-wave in water, which travels at $\sim 1500m/s$. Further, it could be a converted wave, where a P wave travels downwards and at a sharp jump in the properties creates a reflected converted S-wave which propagates upwards. The physics behind all the phenomena is complicated, but the model should theoretically be able to capture this response behaviour. However, in all the models tested in this research, it was not possible to generate a significant (visible) response in this region. Since, it is likely this corresponds to some resonating behaviour, then this event may not be of interest for the surface wave identification and probably can be ignored if it does not assist the inversion.

To investigate this slightly further, the data was analyzed in the frequency-space domain. At every frequency the decay factor was fit to the data for a simple geometric decay of $A = \frac{c}{r^n}$ where n is the decay factor, c is a constant and r is the radial distance from the source. Logs were taken of the equation and the parameters were fit by using a linear polyfit in Matlab, where the equation form is $log(A) = log(C) - nlog(r)$. Surface waves are known to decay with n=0.5 while body waves that travel along the surface decay faster at n=2 [9], [10]. The material damping will increase this decay factor while the interaction of multiple modes means that the amplitude may not strictly decay but can locally increase, rendering this simple fitting method to be less accurate. From Figure 5.10 we see that only near 5Hz is the energy concentrated near a decay factor associated with a surface wave. At the other frequencies, the decay factor is much higher, which indicates that it is related to an evanescent wave type or a body wave that propagates along the surface. Surface waves can still exist since this is a combined decay factor, but it is clear that the surface waves, which we wish to use for identification, are not the major contribution to the total energy at this part of the spectrum.

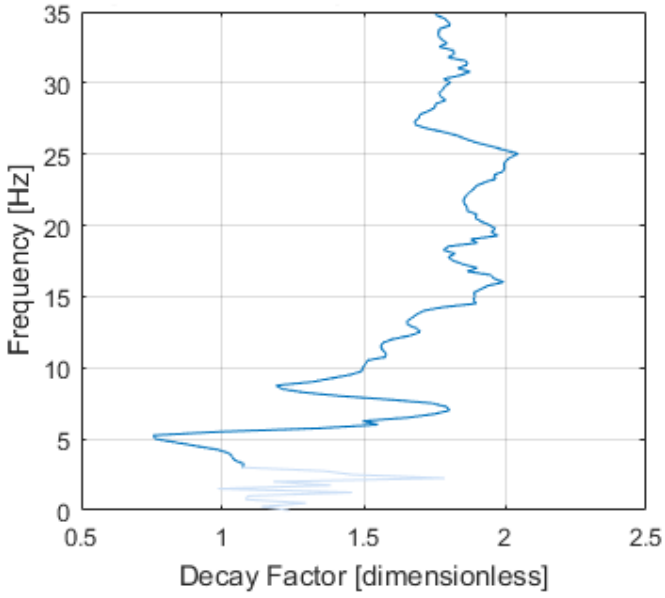

Figure 5.10: Frequency-Space domain fit attenuation factors n where $A \sim r^{-n}$.

Overall, it becomes clear that this is a difficult dataset and perhaps the measurement setup is not sufficient for the surface wave inversions that we wish to perform. However, now that we understand the limitations of the quality of the data, let us try to get the best possible results out of it.

Several picks or interpretations of the modal root locations are made using both purely manual picking and a semi-automated method which is a combination of automated and manual picking. Since the data is not clear, and the picked root locations have a large impact on the stiffness inversion, several different root sets are tested in the inversion process, also with different inversion settings. The picked roots are shown in figures 5.11 to 5.14. The fully automated pick shown in Figure 5.11 are not used, but is included to show the location of the peaks in the response spectra. It is interesting that the high velocity event and mode that extends above the large spot of energy is composed of multiple peaks of lower group velocity rather than one single peak. It is possible this one large energy event is actually a combination of multiple modes. In the manually picked root set, in Figure 5.12, it is intentional that there is a denser selection on the fundamental mode to resolve the fundamental mode more accurately. The fundamental mode is of key interest to the inversion process. Although it is unclear where the modes lie, several points are placed in the centre of some disconnected energy regions in order to give some minor weighting to these phenomena in case they do actually correspond to modes. The high energy spot and the tail extending above the spot is picked with one single line, even though it is not physically clear what this event corresponds to, perhaps it will be important to the inversion and is thus included. It is only picked from the centre of the spot and above so that the maximum phase velocity of these points is $1200[m/s]$. Two root sets, shown in figures 5.13 and 5.14, are created with a semi-automated picking method. The automatic pick for the lower modes are accepted while two interpretations of the higher mode are manually added to the root set. In the first pick, a more classic picking approach is taken while in the second it is considered that a more strange mode behaviour may be possible where the highest mode extends all the way to the y-axis. It is seen in literature that these types of modes can theoretically exist [11]. The use of these various dispersion curve root sets will be discussed in the specific inversion cases which are considered.

An estimate of the stiffness profile in 1m increments down to 30m has been made by Pim Versteijlen [31]. This profile was estimated by performing an inversion on seismic cone penetration test measurements. Although, a baseline profile is not used in the inversion process, the model search range must be defined and so it is useful to have a realistic estimate of the stiffness profile. This profile can also be used to make a smart choice on the discretization of the model. Regions with variations will be discretized more finely than regions where the Cs velocity is roughly constant. It will

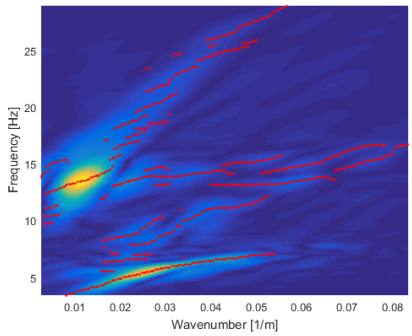

Figure 5.11: Peaks of response spectrum found with the automatic picking tool shown on the measured response.

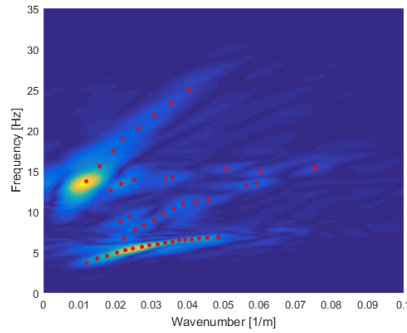

Figure 5.12: Manually picked dispersion curves shown on the measured response.

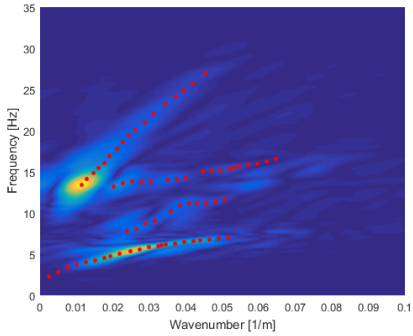

Figure 5.13: Dispersion curves found with semi-automated picking - interpretation 1.

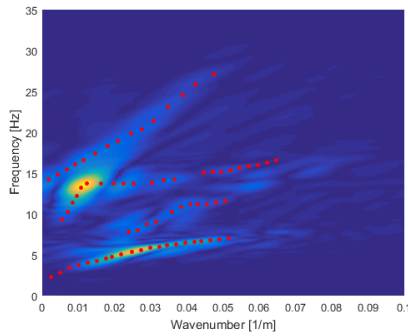

Figure 5.14: Dispersion curves found with semi-automated picking - interpretation 2.

also be considered that the near-surface layers need a finer discretization than the deeper layers. Several discretizations are also investigated to see what the effect is on the inversion, although only the most important runs are included in this report.

5.3.2 Case 1

The first case considers a model with 9 soil layers sandwiched between a water layer and a halfspace layer. This corresponds to the model size that was used in the full waveform inversion [4] although, in this case it is extended to 30m. This is done both since we have the SCPT estimate up to 30m and because we know that this is a point where an abrupt change to a stiffer material occurs. Hence, it seems like an appropriate location for the halfspace. Additionally, the layer thicknesses were made more uniform because the author believes the lateral variability means that the CPT based thickness estimates are not more beneficial than a more uniform choice for the discretization. Assuming less a priori information about the layer thicknesses is also beneficial if the inversion can be successful without it.

This inversion uses the 'semi-automated 2' root set from Figure 5.14. The inversion settings that can be compared to the full waveform inversion are summarized in Table 5.1, while the additional settings that relate to added functionality are given in Table 5.2. The soil profile fixed parameters and Cs velocity range which was specified for the inversion is shown in Table 5.3. A uniform Cp velocity is used, which is equal to the water acoustic velocity. This choice is made since the soil is saturated and it is unlikely that the dilational wave will travel slower than the pressure wave velocity in water [25]. Further, the model sensitivity is very low for the Cp velocity as shown in Chapter 4. Since the model sensitivity to the density is also fairly low, a uniform density is used for this case. A better estimate could be made by computing the layer densities as the average from the finer resolution density profile given with the SCPT results [31]. This was not done for the first case, but was performed for subsequent cases for a small improvement in accuracy.

Table 5.1: IJsselmeer inversion case 1 settings for the genetic algorithm.

N_{gen}	N_{Pop}	N_{Dad}	N_{Con}	p_{FM}
100	240	80	35	0.25

N_{gen} is the number of generations which the genetic algorithm will run. N_{Pop} is the number of trial soil profiles making up the population. N_{Dad} is the number of parents which pass on their genes to the next generation population, which is taken as one third of N_{Pop} by default. N_{Con} is the number of contestants taking part in the tournament selection. p_{FM} is that probability that one of the properties will be uniformly randomly selected from within the search range. p_{SM} is the probability that one of the properties will be selected from a small range, usually 10%, around the current value.

Table 5.2: IJsselmeer inversion case 1 additional settings.

p_{SM}	Re-Range	Layer Strip	Rootset
0	Yes - every 10 gen	No	IJ_comb2

Table 5.3: IJsselmeer stiffness inversion case 1 soil profile and Cs velocity search range.

Layer	Thickness	Cp	ρ	Cs Min	Cs Max
Water	4.4	1520	1025	0	0
1	1	1520	2000	40	250
2	2	1520	2000	40	250
3	2	1520	2000	40	250
4	3	1520	2000	40	250
5	3	1520	2000	100	450
6	4	1520	2000	100	450
7	5	1520	2000	100	450
8	5	1520	2000	100	450
9	5	1520	2000	100	450
Halfspace	∞	1520	2000	400	1200

The convergence observed in Figure 5.15 is not as good as in the synthetic case. There are several reasons for this. Reality does not correspond to a discrete horizontally layered soil deposit. So we expect there is some residual error in the location of the roots because of discretization in our model. Additionally, any noise or measurement error in the measured response spectrum and error in the picking of the roots means that the residuals at the roots cannot be satisfied and the error function remains high. However, we see that the result seems to have converged by approximately 50 generations since the values of the suitability are no longer dropping but oscillate at the same level.

Figure 5.16 shows that the estimate of the best profile is actually somewhat close to the expected stiffness given by the SCPT curve. Indeed we see it is a lot closer than the estimate from the full waveform inversion process as described in [4]. This is a very encouraging result. However, there may be other profiles that have a very similar suitability but different shape. This is related to the non-uniqueness of the found solution. In the full waveform inversion the solutions which were found were drastically different, suggesting they are far away from a global solution. Far from the global solution, multiple solutions have very different profiles but a similar objective

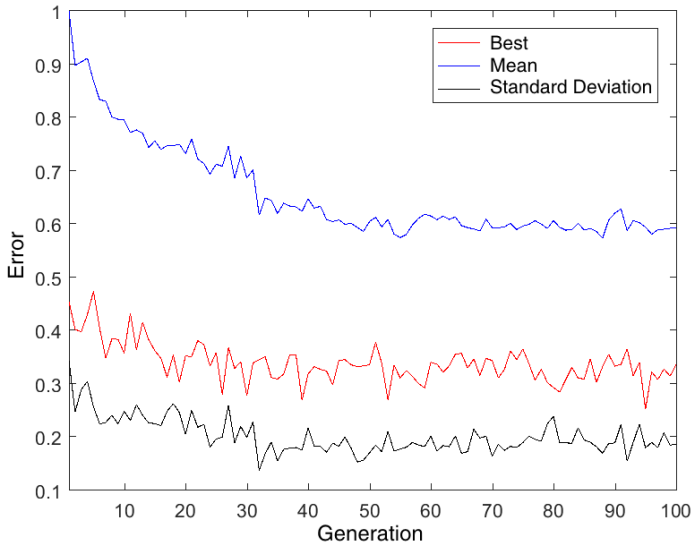

Figure 5.15: Error convergence for case 1 Cs inversion of the IJsselmeer soil profile.

function value. So in order to characterize the range of possibilities within which the solution could lie, the maximum and minimum of the values in the top 15% of the population are determined. This is shown in Figure 5.17 where the mean value of the top 15% population is also plotted. These ranges are fairly wide, indicating there is still quite some variability and non-uniqueness in the solution.

5.3.3 Case 2

The second case that will be considered for the IJsselmeer inversion uses 21 soil layers between the water layer and the halfspace in order to provide a better resolution and also allow the model more flexibility in the shape of the stiffness profile found. From the model studies it was observed that the layer discretization can have a big impact on the dispersion curves. Also, we see a strong linear shape in the SCPT profile near the surface and so both of these would suggest that a fine discretization could be beneficial.

The genetic algorithm settings that were used are the same as those for the first case and are shown in Table 5.1. The root set which was used for case 2 is the 'semi-

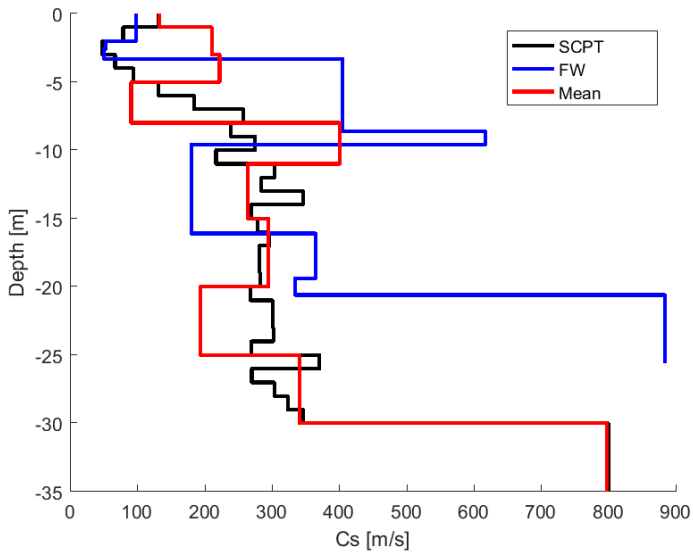

Figure 5.16: IJsselmeer Cs inversion case 1 comparison of inversion results.

automated 1' shown in Figure 5.13 and this difference is shown in the additional settings in Table 5.4. The soil profile fixed parameters and Cs velocity range which was specified for the inversion is shown in Table 5.5.

Table 5.4: IJsselmeer inversion case 2 additional settings.

p_{SM}	Re-Range	Layer Strip	Rootset
0	Yes - every 10 gen	No	IJ_comb1

The convergence at the end of the inversion run does not appear to have improved significantly over the previous case, as shown in Figure 5.18. The best estimate has a lower error than the previous case, however, it is difficult to directly compare the suitability between models with a different number of layers. The best profile, shown in Figure 5.19, shows a very good agreement with the SCPT profile, although it very clearly disagrees in the first 5m. There the MASW predicts a higher stiffness near the surface and that the dip in the stiffness has its minimum 2m deeper in the soil. Figure 5.20 shows that the ranges are wide and so the uncertainty in such a profile could still be relatively high, but it again confirms the overall shape of the

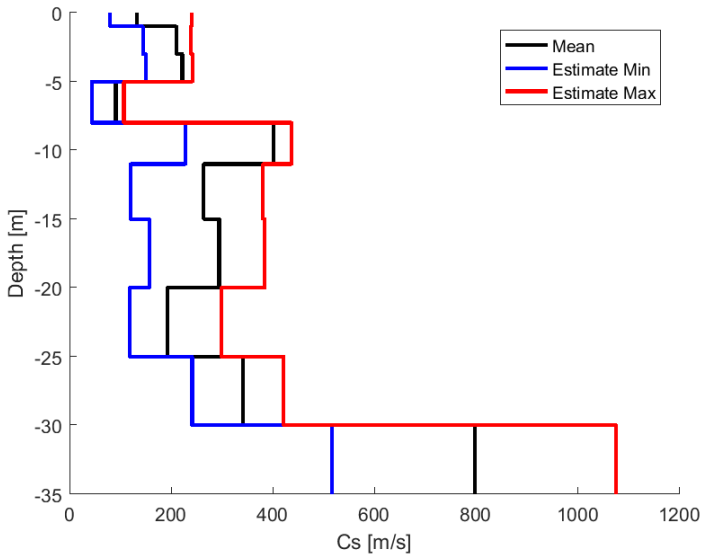

Figure 5.17: IJsselmeer Cs inversion case 1 range of the estimated parameters based on the top 15% of the population.

SCPT profile quite well.

5.3.4 Case 3

The third inversion case uses the same genetic algorithm and inversion settings as the previous case, but with the manually picked root set shown in Figure 5.12. This change of the root set in the additional inversion settings is shown in Table 5.6. The soil profile fixed parameters and search ranges were kept the same as the previous case and are shown in Table 5.5.

Figure 5.21 shows the convergence is comparable to before. Figure 5.22 summarizes the inversion run results. The best profile seems to deviate more from the SCPT estimate, even though the velocity ranges are slightly smaller. This could be random chance and the mean of the top population indeed has quite a good agreement with the SCPT measurements. This indicates that manually picking the root set, seems to have a small effect on the inversion performance if the picking is done carefully. In fact, the slightly smaller ranges could indicate that the manually picked

Table 5.5: IJsselmeer stiffness inversion case 2 soil profile and Cs velocity search range.

Layer	Thickness	Cp	ρ	Cs Min	Cs Max
Water	4.4	1520	1025	0	0
1	1	1520	1400	40	250
2	1	1520	1700	40	250
3	1	1520	2000	40	250
4	1	1520	2000	40	250
5	1	1520	2000	40	250
6	1	1520	2000	40	250
7	1	1520	1900	100	350
8	2	1520	1800	100	350
9	1	1520	1800	150	450
10	1	1520	1800	150	450
11	2	1520	1800	150	450
12	1	1520	1800	150	450
13	2	1520	1600	150	450
14	1	1520	1700	150	450
15	3	1520	1667	150	450
16	1	1520	1800	150	450
17	3	1520	2000	150	450
18	1	1520	2000	150	450
19	1	1520	2000	150	450
20	2	1520	2000	150	450
21	2	1520	2000	150	450
Halfspace	∞	1520	2000	400	1200

Table 5.6: IJsselmeer inversion case 2 additional settings.

p_{SM}	Re-Range	Layer Strip	Rootset
0	Yes - every 10 gen	No	IJ_MP1

roots resulted in an estimate with a higher degree of certainty. It is interesting that the weakest layer with a depth of $4-5m$ has a very narrow range, while most of the ranges are much larger.

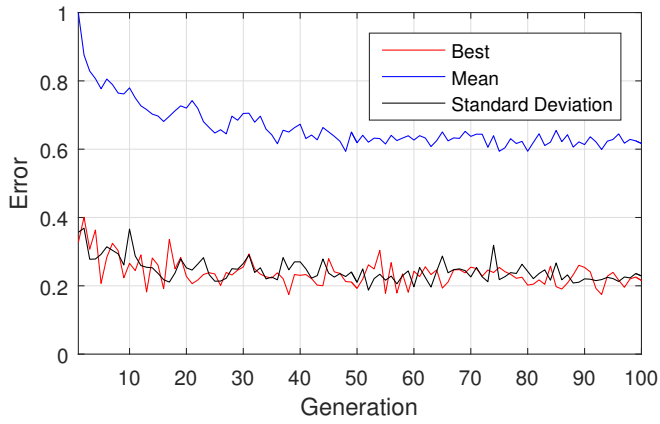

Figure 5.18: Error convergence for case 2 Cs inversion of the IJsselmeer soil profile.

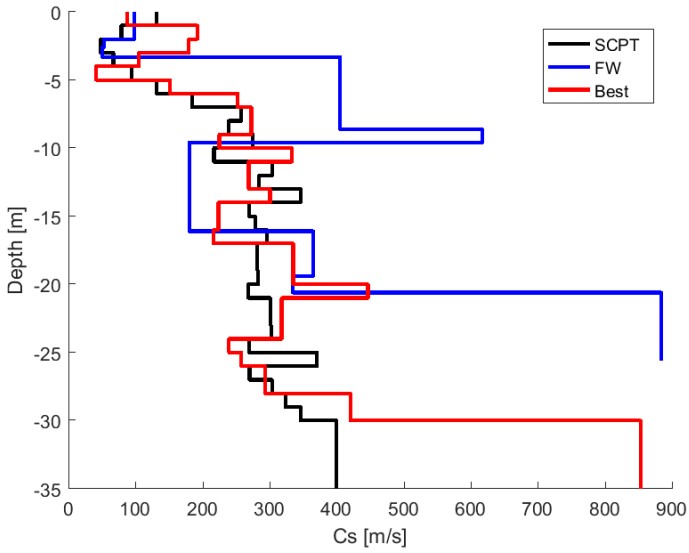

Figure 5.19: IJsselmeer Cs inversion case 2 comparison of inversion results.

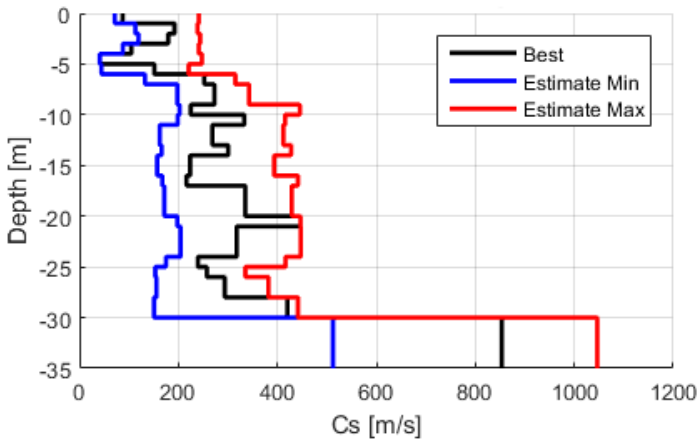

Figure 5.20: IJsselmeer Cs inversion case 2 range of the estimated parameters based on the top 15% of the population.

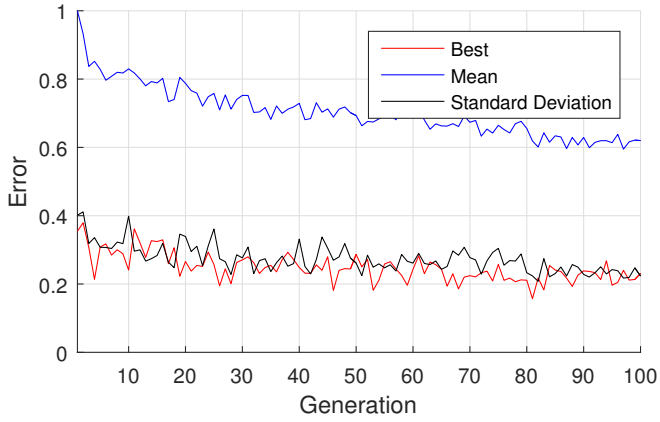

Figure 5.21: Error convergence for case 3 Cs inversion of the IJsselmeer soil profile.

5.3.5 Case 4

The last case uses a new root set, shown in 5.23, that ignores the high energy spot and the mode that occurs above it. The genetic algorithm and all other inversion

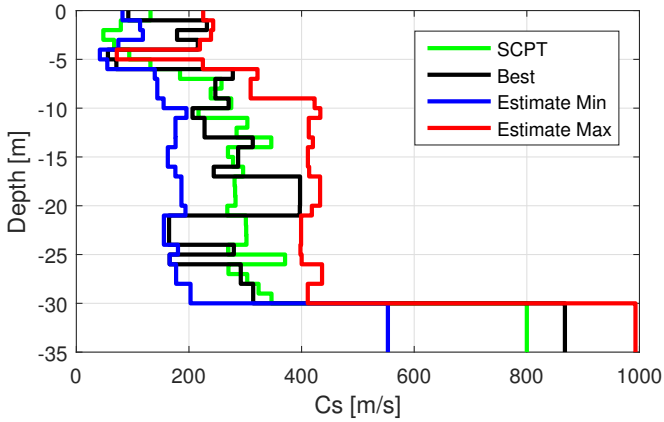

Figure 5.22: IJsselmeer Cs inversion case 3 comparison of inversion results and range of the estimated parameters based on the top 15% of the population.

settings are kept the same. The 21 layer soil model given in Table 5.5 is also used.

It is clearly seen in Figure 5.24 that this results in a better convergence. The high energy mode was difficult for the model to handle and that is why there was a persistent large error due to the points in this region that could not be matched. Removing those points has allowed for a better convergence. As a result the ranges, defined by the top 15% of the final population, in 5.25 are much smaller in width compared to the previous inversion attempts. This indicates a higher certainty in the stiffness profile. Although, the best candidate, shown in Figure 5.26, seems to have a more staggered appearance that seems to be physically unrealistic. This could correspond to the presence of several stiff layers or it could be some form of error where the inversion process is not converging to a physically valid candidate. The top 15% of the population is plotted with the colours scaled by the suitability where the red profile is the best candidate and the fainter yellow profile is the worst of the top 15% of the final population.

In order to further verify the results, for every run we have investigated sensitivities, statistics about the population and the roots. A good way to analyse the results is to plot the input roots on top of the F-K spectrum of the response related to the best candidate after inversion. This is shown in Figure 5.27. Alternatively, Figure 5.28 shows the roots from the best candidate profile and plotted on top of the measured response spectrum. Lastly, the theoretical roots of the best candidate are

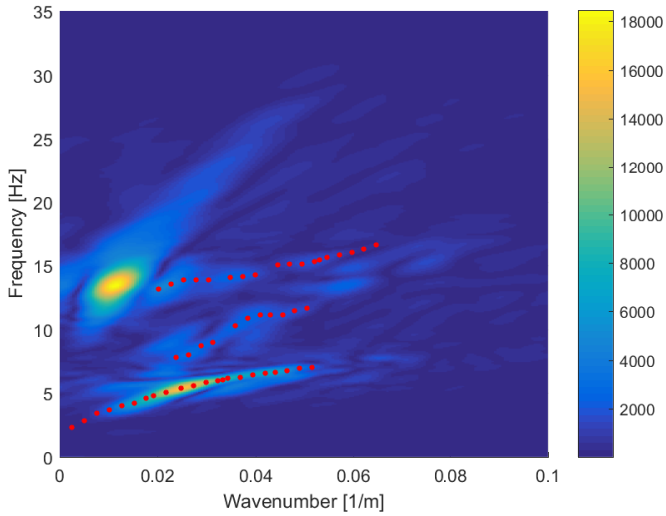

Figure 5.23: New root set automatically picked from the IJsselmeer response spectrum which only contains the 3 lower roots.

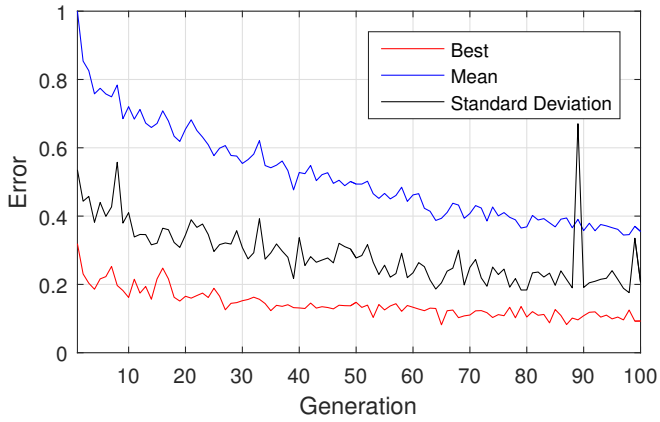

Figure 5.24: Error convergence for case 4 Cs inversion of the IJsselmeer soil profile.

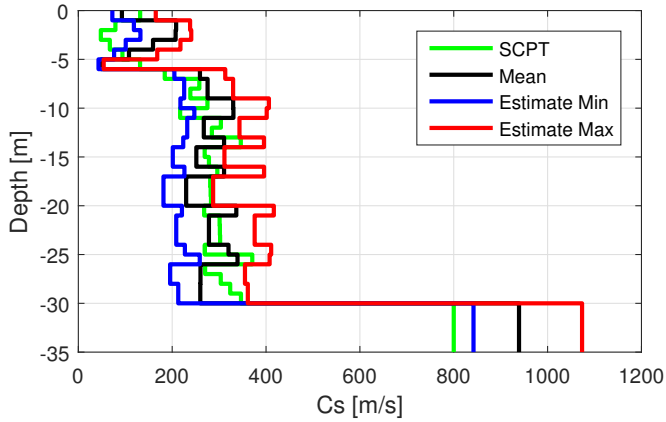

Figure 5.25: IJsselmeer Cs inversion case 4 comparison of inversion results.

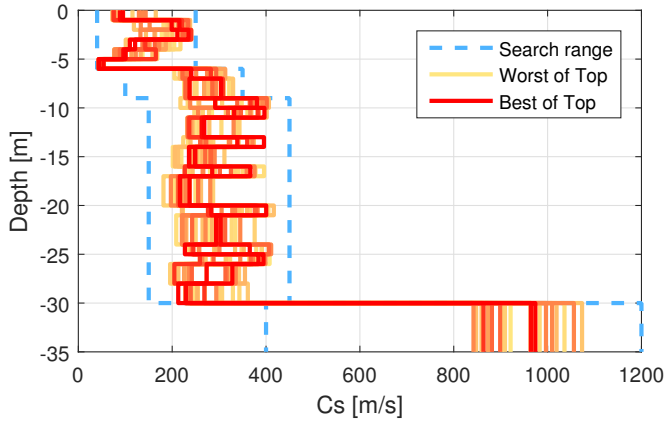

Figure 5.26: IJsselmeer Cs inversion case 4 search range and top 15% of the population with scaled colours based on the suitability

plotted with the input (measured) roots, shown in Figure 5.29. For this inversion case these three plots show quite good agreement, meaning the found candidate is plausible and valid. If the roots do not match up, then it can be certain the inversion was not good enough to trust the inversion. A good visual match is not enough to say

that a profile is correct, but adds a large measure of confidence. It can be observed in Figure 5.29 that the measured second mode wiggles around the theoretical mode, and it is likely that if we were to interpret the measured data considering a more straight mode response at this location, that we could get an even better fit.

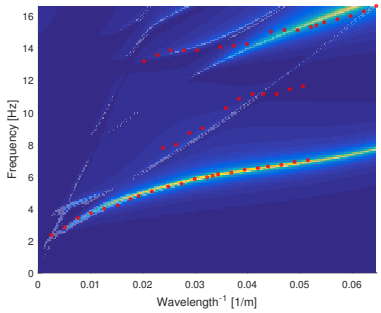

Figure 5.27: IJsselmeer Cs inversion case 4 comparison of input modes plotted on the response spectrum of the best candidate.

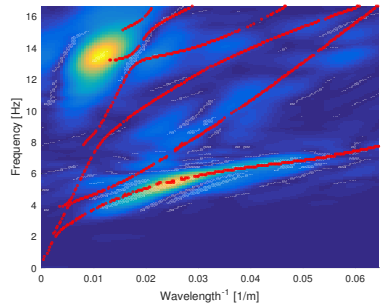

Figure 5.28: IJsselmeer Cs inversion case 4 comparison of theoretical modes of best candidate plotted on the measured response spectrum.

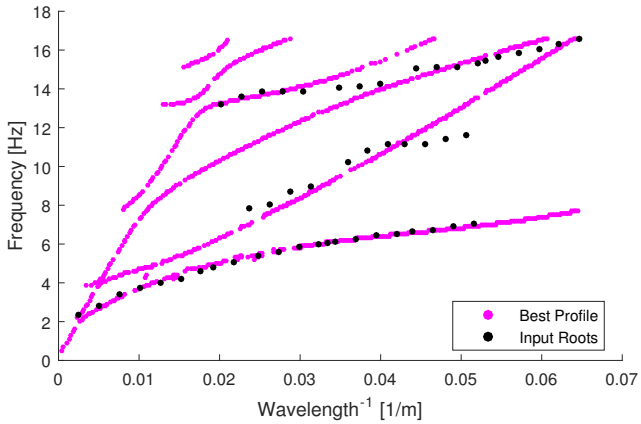

Figure 5.29: IJsselmeer Cs inversion case 4 comparison of the input modes and the theoretical modes of the best candidate.

5.3.6 Conclusions on the IJsselmeer stiffness inversion

Although the results are not exhaustive, it can be concluded that the modal inversion process is significantly more successful than the full waveform inversion process. Several velocity profiles are found, which are all in relatively close agreement with the SCPT inversion profile. A range of different profiles have a suitability value close to that of the best fit, so perhaps it cannot be said exactly what the best profile is, but rather a range can be given within which it is expected to lie. No results were presented for the layer stripping process because it was not found to be effective for the inversions of the IJsselmeer data. The layer stripping process forces the upper layers to fix on one value and due to the non-uniqueness of the solution, where multiple profiles are close to satisfying the data, this is a bad assumption. The algorithm may converge to one profile, but it is not guaranteed that it is the global minimum and also it would misrepresent that data if we suggest that we can determine one specific profile from the data.

The roots of the best stiffness profile from the final inversion run match the measured roots well, and the spectra are also in reasonable correspondence. Table5.7 shows the values determined by the end of the last inversion run. The maximum, minimum and mean of the top 15% of the population are given along with the profile of the best candidate.

5.4 Gjøa Stiffness Inversion

Another dataset to perform the inversion method on was made available through a collaboration with the Norwegian Geotechnical Institute (NGI). This high quality dataset was obtained via the NGI prototype seabed-coupled shear wave vibrator. This uses a 3.25m diameter suction caisson which penetrates 2.5m into the soil and contains a linear hydraulic actuator with a 3700kg mass. The actuator can be rotated to produce Love or Scholte waves. It can produce excitation frequencies from 5-60Hz and can produce a flat power spectral density between 10-55Hz. The maximum horizontal force is 250kN. A 4 component cable is used to capture the hydrophone and 3 direction geophone signals. The array is 600m long and dragged into place across the source so that there is 440m of uninterrupted cable on one side of the source. Dragging is used to achieve an effective receiver spacing of 2.5m. The source sweep contains a signal which ramps up in frequency and lasts 7.5s and then an additional 7.5s is recorded in order to capture the propagating waves. For the full details about the collection of the data refer to [29].

The Gjøa data set contains stacked versions of both the in-line and cross-line

Table 5.7: Summary statistics for IJsselmeer Cs inversion case 4 result.

Layer	Thickness	Cp	ρ	Cs Min	Cs Best	Cs Max	Cs Mean
Water	4.4	1520	1025	0	0	0	0.0
1	1	1520	1400	72.4	94.8	165.0	92.9
2	1	1520	1700	118.4	198.9	238.1	208.4
3	1	1520	2000	132.3	210.9	240.6	207.3
4	1	1520	2000	101.0	109.8	217.6	159.1
5	1	1520	2000	76.2	100.7	168.1	107.9
6	1	1520	2000	43.0	43.7	54.0	48.9
7	1	1520	1900	204.6	240.7	313.1	259.2
8	2	1520	1800	225.5	304.1	329.8	275.4
9	1	1520	1800	217.5	291.6	406.1	330.0
10	1	1520	1800	247.2	396.6	401.4	330.5
11	2	1520	1800	232.0	268.3	343.4	267.4
12	1	1520	1800	223.5	395.6	395.6	310.6
13	2	1520	1600	201.3	235.7	311.3	251.5
14	1	1520	1700	226.0	366.5	395.8	310.5
15	3	1520	1667	181.4	237.0	287.2	229.7
16	1	1520	1800	220.8	400.3	416.6	336.6
17	3	1520	2000	208.6	293.6	375.7	278.3
18	1	1520	2000	227.1	227.1	410.9	320.0
19	1	1520	2000	258.8	394.6	407.6	339.2
20	2	1520	2000	195.6	328.1	355.1	260.3
21	2	1520	2000	212.9	212.9	361.2	259.9
Halfspace	∞	1520	2000	842.1	973.9	1073.4	939.1

source sweeps. These can be used for Scholte and Love wave analysis. Since the author's tools were not developed to handle Love waves, this analysis will only focus on the Scholte wave. However, it should be considered that the Love wave may prove to be the best dataset to use since it does not contain the body pressure waves and only the surface waves are present. Figure 5.30 shows a shot record for the vertical velocity of the inline sweep.

The data is transformed to the wavenumber domain using a discrete Hankel transformation (DHT). The computed spectrum is shown in Figure 5.31. Two root sets are considered for the inversion cases and are shown in Figures 5.32 and 5.33.

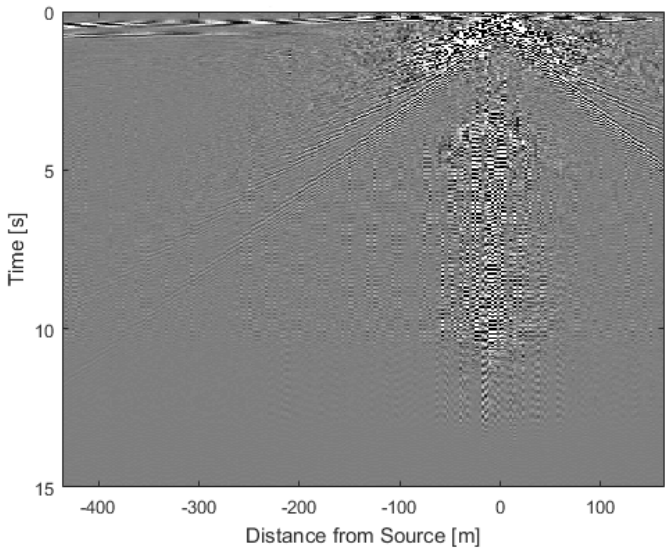

Figure 5.30: Gjøa shot record for vertical velocity of the inline sweep.

5.4.1 Case 1

The first inversion case for the Gjøa data used only the fundamdental mode. The same settings genetic algorithm settings are used as for the IJsselmeer inversion cases, except for the different input roots and soil layering. The settings are shown in Table 5.8 and 5.9. The fixed soil parameters and the Cs velocity ranges are shown in Table 5.10.

Table 5.8: Gjøa inversion case 1 settings for the genetic algorithm.

N_{gen}	N_{Pop}	N_{Dad}	N_{Con}	p_{FM}
100	240	80	35	0.25

Table 5.9: Gjøa inversion case 1 additional settings.

p_{SM}	Re-Range	Layer Strip	Rootset
0	Yes - every 10 gen	No	Fundamental only

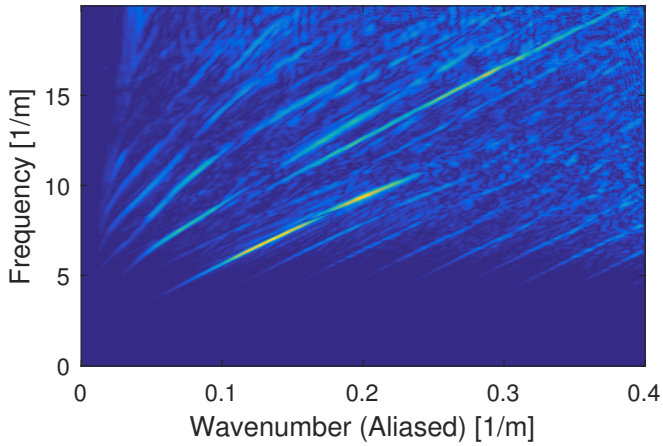

Figure 5.31: Gjøa data f-k spectrum of vertical velocity for the inline sweep.

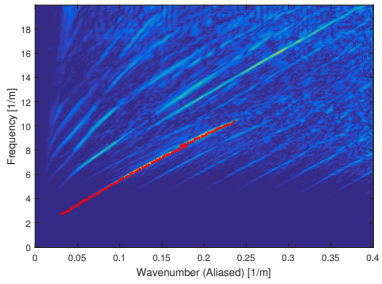

Figure 5.32: Gjøa fundamental mode picked from spectrum peaks.

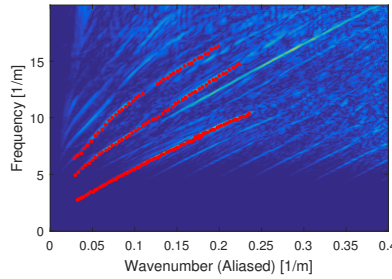

Figure 5.33: Gjøa fundamental mode and two higher modes.

Figure 5.34 shows that the inversion achieves excellent convergence. This is because the data is of a high quality and because only the fundamental mode is used. The inversion finds a very good match to the data. Figure 5.34 shows the ranges of the estimate for the top 15% of the final population as well as the mean of this top population. It shows that the top 10m of soil has been estimated with a very high degree of confidence as indicated by the very narrow ranges. Lower in the soil the ranges are wider as the system loses sensitivity to the lower layers. The overall

Table 5.10: Gjøa soil profile fixed parameters and Cs velocity search range.

Layer	Thickness	Cp	ρ	Cs Min	Cs Max
Water	364.6	1500	1025	0	0
1	1	1500	1650	20	300
2	2	1500	1700	20	300
3	4	1500	1800	20	300
4	4	1500	1800	80	400
5	4	1500	1900	80	400
6	4	1500	1900	80	400
7	4	1500	2000	80	400
8	4	1500	200	150	500
9	4	1500	2100	150	500
10	4	1500	2100	200	600
11	4	1500	2100	200	600
Halfspace	∞	1500	2100	200	700

profile is very linear in behaviour. It matches well with previously published results [25], both in shape and in magnitude.

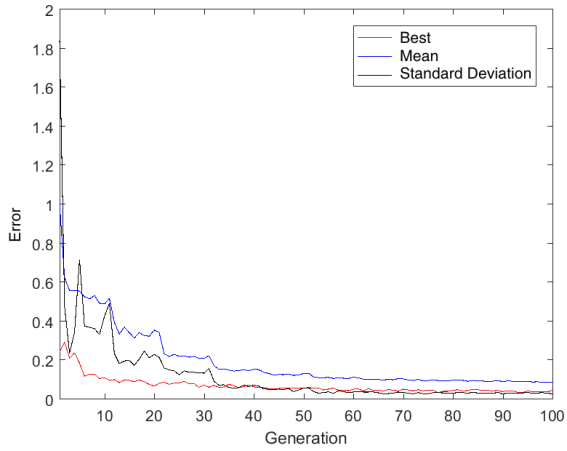

Figure 5.34: Error convergence for case 1 Cs inversion of the Gjøa soil profile.

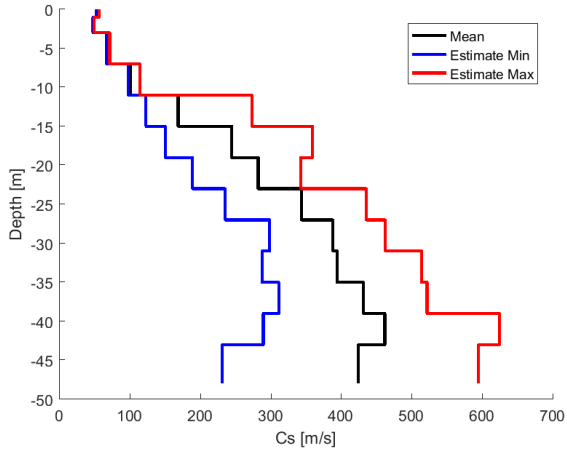

Figure 5.35: Gjøa Cs inversion case 1 range and mean of the estimated parameters based on the top 15% of the population.

5.4.2 Case 2

The second inversion case for the Gjøa data starts with the same settings as before but uses the phased settings functionality. It starts with only the fundamental mode and then after 30 generations introduces the next two higher modes as well. After 30 generations the fundamental mode is given a weighting of 0.5 while each of the two higher modes each have a weighting of 0.25. Additionally, at generation 40 layer stripping is started and one layer is turned off every 10 generations.

Figure 5.36 shows that excellent convergence is again obtained. It is difficult to comment about the exact level of convergence since the values are no longer visible on the same scale as the starting graph. In such a case the suitability should perhaps be plotted on a log scale. Figure 5.37 shows that the soil profile has been estimated with higher certainty down to 15m, an improvement over the previous case. This is due to two combined effects. The first is that the higher modes carry sensitivity to the deeper soil deposits and including them allows more certainty about the deeper layers. The second effect is that the layer stripping turns off variation in the upper layers, so the inversion can focus on the deeper layers and estimate them with a higher degree of certainty. With the already high certainty of the estimates in the upper layers, it is unlikely that the layer stripping process is locking in the wrong estimates, which would compound the error for deeper layers. Hence, layer stripping

can be used because the inversion already appears to be well behaved. However, it should not be used too agressively, that is it should not be started too early in the inversion process or layers switched off too rapidly as this would lead to estimation errors.

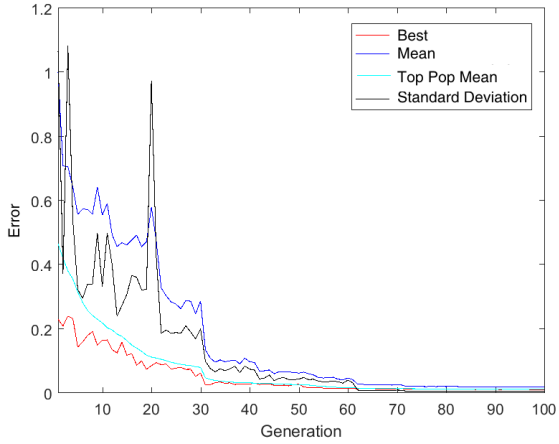

Figure 5.36: Error convergence for case 2 Cs inversion of the Gjøa soil profile.

Figure 5.41 shows the search ranges and the top 15% of the final population with the colours scaled according to the suitability of the candidates. The red profile shows the best one while the lighter yellow profiles are less good estimates. There is still a lot of scatter in the deeper layers of the estimates.

In order to assess the validity (or lack thereof) of the estimate, it is insightful to compare the roots and spectral responses. Figure 5.38 shows the measured modes plotted on the theoretical response spectra, created with a dirac pulse source. Figure 5.39 shows the theoretical modes of the best estimate for the stiffness profile plotted on top of the measured response spectrum. Figure 5.40 shows the theoretical roots of the best estimate plotted with the measured dispersion curves. From these three figures we can see that the fundamental mode lines up extremely well. The other modes, do not seem to line up as clearly. The second measured mode crosses between the third and second theoretical modes while the third measured mode shares is close to the fourth theoretical mode at some points but also deviates at other points.

This is an interesting result, since the error function indicated a very good convergence, yet visually there is a misfit. This is for several reasons. The classic misfit

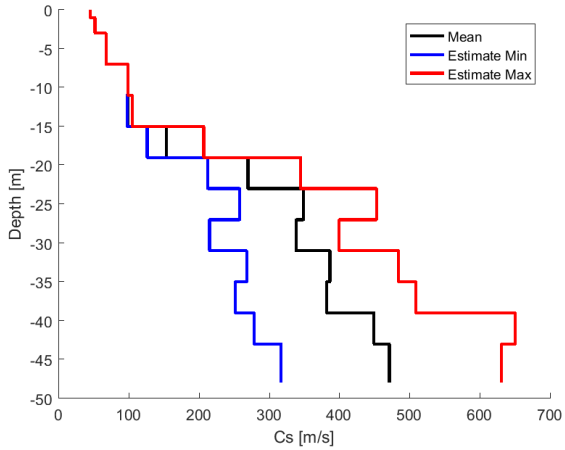

Figure 5.37: Gjøa Cs inversion case 2 range and mean of the estimated parameters based on the top 15% of the population.

function, which measures the distance between the roots, corresponds well with visual intuition. However, the determinant based misfit does not since the formulation is completely different and does not directly include any distance measuring. The determinant function can be relatively flat between the modes due to the normalization. Therefore, the error is not increasing with linear distance of the mode from its 'true' location and the points which are 'far' from lining up may only incur slightly more error than points which are 'close'. This can be understood by seeing that the dips in the normalized determinant in Figure 3.11 are very close to the modes, and that relatively large spaces between modes can have similar error values.

If it is required to have the modes line up more accurately this could be done in three ways. Firstly, the higher modes could be given a higher weighting in the cost function. Secondly, it is possible to adjust the smoothing operation of the determinant normalization in order to allow more sensitivity of the determinant function to the distance from the mode. That is, the dips of the determinant function near the modes could be made wider by applying the moving average over a larger number of points. This could be beneficial or disadvantageous and further testing would have to be completed with inversion runs. Using a small smoothing fraction ensures that all of the soil profiles have more similar determinant values, so a larger smoothing fraction may make the fit worse. The third method would be to use the classic misfit function in a hybrid approach which uses both misfit functions. After the inversion

has been done with the determinant misfit function, then the final soil profile can be tweaked to fit better according to the classic distance measuring misfit function.

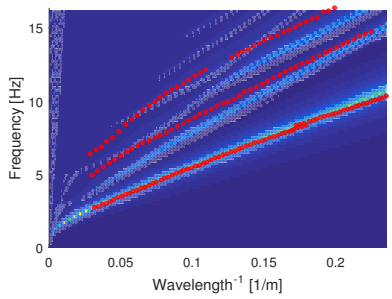

Figure 5.38: Gjøa Cs inversion case 2 comparison of input modes plotted on the response spectrum of the best candidate.

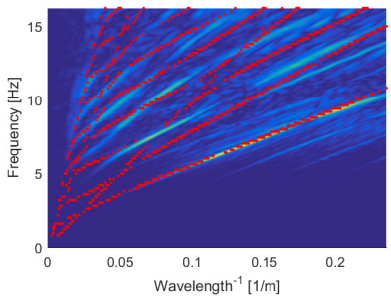

Figure 5.39: Gjøa Cs inversion case 2 comparison of theoretical modes of best candidate plotted on the measured response spectrum.

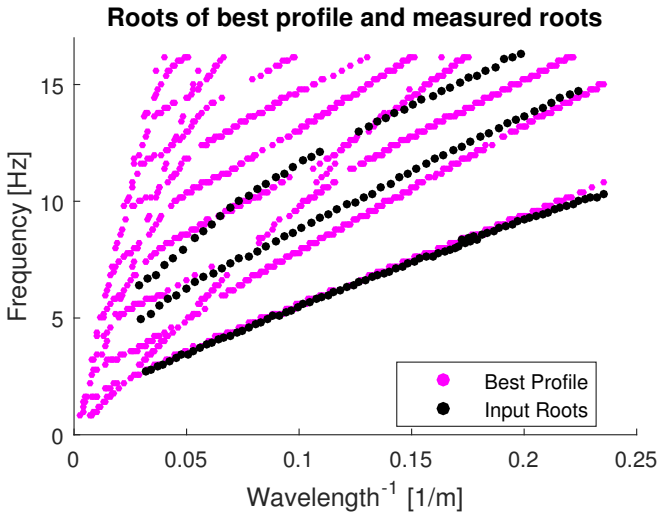

Figure 5.40: Gjøa Cs inversion case 2 comparison of the input modes and the theoretical modes of the best candidate.

5.4.3 Conclusions on the Gjøa stiffness inversion

Overall, we see that the predicted stiffness profile, shown in Figure 5.41, agrees well with the published results from Socco [25], shown in Figure 5.42. There are several differences in the formulation of the inversion process. First, the choice of using a genetic algorithm instead of using a Monte Carlo approach as used by Socco. Additionally, the choice to normalize the determinant and how the determinant was normalized. Thirdly, use of the layer stripping process. Hence, it is encouraging that these results are in good agreement. The results presented in this report suggest a higher degree of certainty for the stiffness profile than the published results. However, more studies would have to be done to make this conclusive.

The average and mean profiles are shown in Table 5.11.

Table 5.11: Gjøa soil profile fixed parameters and Cs velocity search range.

Layer	Thickness	Cp	ρ	Cs Best	Cs Mean
Water	364.6	1500	1025	0	0
1	1	1500	1650	45	45
2	2	1500	1700	52	52
3	4	1500	1800	68	68
4	4	1500	1800	99	99
5	4	1500	1900	99	99
6	4	1500	1900	148	153
7	4	1500	2000	282	270
8	4	1500	200	283	349
9	4	1500	2100	241	339
10	4	1500	2100	268	387
11	4	1500	2100	440	382
12	4	1500	2100	449	449
Halfspace	∞	1500	2100	439	471

The main purpose of this stiffness inversion was to determine the stiffness profile accurately so that it could be used in a damping inversion method. To that end, we have a high degree of confidence that we have found a good estimate of stiffness profile and can use it for the damping inversion, which will be discussed in Chapter 6. Since only the fundamental mode is lining up well, then only the fundamental mode should be used for the damping inversion. If a multi-modal damping inversion is to be performed, then the misfit in the higher mode dispersion curves needs to be addressed in order to ensure that theoretical modes correspond directly to the

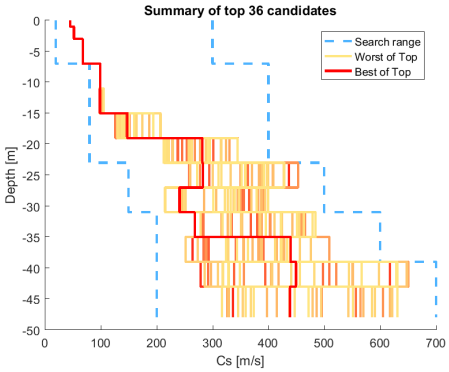

Figure 5.41: Gjøa Cs inversion case 2 search range and top 15% of the population with scaled colours based on the suitability.

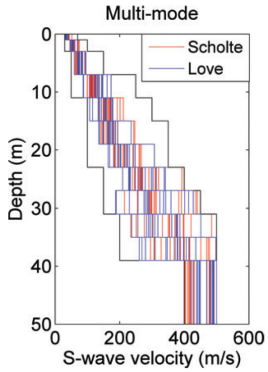

Figure 5.42: Gjøa published stiffness estimate [25].

measured modes.

Chapter 6

Damping

This chapter focuses on the identification of the material damping properties of the soil. The damping is of great relevance for monopile structures since this long slender structure tends to be poorly damped. Current design methods combine structural and soil damping into one combined conservative value that is decided based on experience and limited data. Hence a method to estimate the actual damping could be of great value to the design process.

Section 6.1 discusses three methods to identify the modal damping or attenuation curves from measured data. By nature of their differences, these three methods will result in different modal damping curves. Section 6.2 verifies two methods to compute the modal damping curves of a theoretical soil system. These methods should produce the exact same model damping curves and any differences are due to computation errors. Note, that confusingly the half-bandwidth or Q-factor method, described in section 6.1.3, falls under both categories and could be used to both compute the modal damping curve from measurements or from the response spectrum computed for a theoretical model.

6.1 Attenuation Curve Identification Methods from Measured Data

There are several methods used in literature that can theoretically be used to identify the material damping ratio from measurements. The paper by S.A. Badsar [3] covers two existing methods and introduces a new method, while comparing the

effectiveness of all three methods. The findings of this paper are summarized below.

6.1.1 Phase-Amplitude Regression in Frequency-Space Domain

The force signal and resulting displacement are transformed from time to frequency via the Fourier transformation. The frequency-space transfer function of force to displacement is computed $H(r,\omega) = \frac{u(r,\omega)}{F(\omega)}$ where $H(r,\omega)$ is the transfer function, $u(r,\omega)$ is the displacement and $F(\omega)$ is the source spectrum. Usually several recordings are stacked to create an estimate of the transfer function with better signal to noise ratio. The experimental dispersion curve, $C_R(\omega)$, and attenuation curve, $A_R(\omega)$, of the surface wave are determined by phase and amplitude regression. This scheme assumes that there is only one surface wave and multiple modes do not exist. Then the transfer function is

$$h(r,\omega) = \zeta(r,\omega)e^{(-i\frac{\omega}{C_R(\omega)})}e^{-A_R(\omega)r}$$

The first term $\zeta(r,\omega)$ accounts for the geometric damping and is equal to the displacement amplitude in a soil deposit without damping. Since it depends on the stratification, which is initially unknown, the surface wave decay factor of $\zeta(r,\omega) = \frac{1}{\sqrt{(r)}}$ is used and then iterated. The second term $e^{(-i\frac{\omega}{C_R(\omega)})}$ is a harmonic function that depends on the Rayleigh wave velocity. The third term $e^{-A_R(\omega)r}$ is an exponential decay that accounts for the wave decay due to material damping.

The first step in the inversion procedure is to perform an amplitude and phase regression. This problem has many local minima and the correct global solution must be found. The estimate of the dispersion and attenuation curves are then used to solve an inverse problem for the shear wave velocity profile. This new profile is used to update the geometric spreading factor and this whole procedure is iterated until convergence is reached. Next, the attenuation curve is assumed to be correct and an inversion problem is solved to determine the material damping ratio profile of the soil, which corresponds to the attenuation curve.

6.1.2 Amplitude Regression in Frequency-Wavenumber Domain

This method is somewhat similar to the previous method and is also similar to the modal surface wave inversion. The experimental transfer function is determined where the frequency-space data from the previous method is transformed into the frequency-wavenumber domain using the appropriate Hankel transformation in order to properly account for the cylindrical nature of the wavefield. The dispersion

curve is taken to be the peak in the frequency-wavenumber spectrum. An inverse problem is solved to find the stiffness profile. Then this is used to estimate the geometric spreading factor. No iteration is required for the geometric spreading factor since it is computed directly. The attenuation curve is still calculated from the frequency-space data, but using the direct estimate of the geometric spreading factor. With the attenuation curve $A_R(\omega)$ found then a second inverse problem must be solved to determine the material damping ratio of the layered soil.

6.1.3 Half-power Bandwidth in Frequency-Wavenumber Domain

The final method uses a modified half-power bandwidth or Q-factor method in order to determine the attenuation curve directly from the measured data. It is the only method that is suitable for incorporating multi-mode data and calculating attenuation curves separately for each mode rather than just assuming one relation with frequency. This method uses an analogy to the single degree of freedom system and the attenuation curve is identified from the width of the peak of the spectral response. Appendix B shows a proof of the relationship for the half-power width, the Q-factor and the damping ratio. In a single degree of freedom system we have

$$\zeta = \frac{\Delta\omega}{\omega_{res}} = \frac{1}{2Q} \tag{6.1}$$

A modification is made to the half-power bandwidth method where instead of measuring the magnitude at $\frac{1}{\sqrt{(2)}}$, (or $\frac{1}{2}$ in the energy spectrum), the amplitude can be measured at any height that is specified as γ times the peak value. It is preferable to measure the width closer to the peak since there is a relatively smaller contribution occurring from adjacent peaks. The relationship is derived for both viscous and hysteretic damping and so it is verified that for both that the following relation applies:

$$\zeta = \frac{\Delta\omega}{\omega_{res}} \frac{1}{\sqrt{\gamma^{-2} - 1}} \tag{6.2}$$

where γ is the ratio of the amplitude where the width is measured to the amplitude of the peak and is therefore allowed to vary between 0 and 1. The height at which this measurement is made is a parameter that must be carefully chosen [3]. Selecting γ closer to 1 results in less influence from adjacent energy peaks, but may introduce more error in determining the actual width.

The limited length of the measurement array introduces a windowing effect that causes a widening of the peaks in the frequency-wavenumber domain. Badsar [3] re-

moves this effect by introducing an artificial additional damping in the form of an exponential window. The decay rate for this exponential window must be chosen carefully and is chosen differently for every frequency with the windowing performed in the frequency-space domain. This artificial attenuation that is introduced by the exponential window is subtracted from the attenuation that is measured from the spectrum. Note, the geometric attenuation is automatically accounted for through transformation of the measured spectrum with the Hankel transformation and with the estimated stiffness profile that is required as an input for the damping inversion problem. If the stiffness profile is poorly estimated, this can cause an inaccurate prediction of the geometric damping thereby leading to an incorrect estimate of the material damping. However, this error is common to all three methods.

In the comparison by Badsar, the half-power bandwidth method was found to be the most effective at retrieving the synthetic damping profile on three benchmark tests. All three methods can retrace an adequate damping profile. While in the irregular soil profile the third method retrieves a better result than the first two due to the contribution of the higher modes which cannot be accounted for in the first two methods. The third method also fares better than the first two in the soil deposit with linearly varying properties, since the first two methods assume that the geometric damping is exactly known. It is important to note that theoretically only the third method can deal with soil deposits where there is a strong contribution of multiple modes. With a multi-mode situation the geometric spreading factor may contain local increases in the amplitude due to interference of the modes. We also wish to be able to use the inversion technique for multi-modal situations and complex stiffness profiles and additionally this third method has a better performance in all of the cases tests. Therefore, the half power bandwidth method, will be used for the estimation of the modal damping curve from the measured data.

6.2 Verification of the Theoretical Calculation Method

This section aims to verify that the half-bandwidth method which will be used to compute the modal damping curve from the measured data, matches with the modal damping curve computed using the theoretical phase damping ratio method.

The first step to implementing a successful inversion of the soil damping profile is to verify that the two methods that are used to calculate the attenuation curves are indeed equal. The first is the half-power bandwidth method which is used to compute the attenuation or modal damping curve from the measured response spectrum. The second method is using the phase damping ratio relation of the complex roots

and will be used to generate the theoretical attenuation curves from the candidate models. Although these methods use alternate definitions of the quality factor in their derivation, they should be equivalent. The phase damping ratio method is used for computing the theoretical modal damping curves because it is more computationally efficient as it does not require generating the entire response spectrum. It is also theoretically more accurate, since some interpolation error is made during the measurement of the spectral width with the modified half-bandwidth method.

6.2.1 Phase Damping Ratio

The phase damping ratio is suggested by S. Foti [10] and is a method that was used by Misbah and Strobbia [18] to analyse the modal attenuation of a theoretical model. This paper borrows from the derivation of the quality factor (Q factor) performed by Carcione [6]. This definition considers the ratio of the peak energy density stored per cycle to the energy dissipated during the cycle. The phase damping ratio is given as:

$$D(\omega) = \frac{Im(k^{*2})}{2Re(k^{*2})} \tag{6.3}$$

where k^* denotes a complex wavenumber and not a conjugation operation.

The test case defined by [10] on page 256 is used with the properties given in Table 6.1.

Table 6.1: S. Foti test case soil profile for phase damping ratio.

Layer	Thickness [m]	Cp [m/s]	Cs [m/s]	Dp	Ds	$\rho[Mg/m^3]$
1	5	400	200	0.04	0.04	1.9
2	5	500	250	0.03	0.03	1.9
3	5	600	300	0.025	0.025	1.9
Half-space	∞	800	400	0.02	0.02	1.9

The complex root locations were computed using the complex root finding tool and methods described previously in Section 3.1. Figure 6.1 shows the multi-modal phase damping ratio curves. The plot on the left is presented by S. Foti [10] and the plot on the right was computed by the author. This clearly shows that the author's root finding tool is in good agreement with the predictions given by S. Foti. However, it can be noted that the root finding is not perfect, which is not surprising given all of the previously outlined difficulties related to finding the complex roots. Nonetheless, the author wished to point out that several erroneous numerical roots

are also found with his root finding technique. These can be seen to occur exactly at the damping ratios specified as inputs for the soil layers, since the erroneous roots occur at phase damping ratios of 0.025,0.03 and 0.04. These roots can and will be filtered to remove them from the modal damping curves.

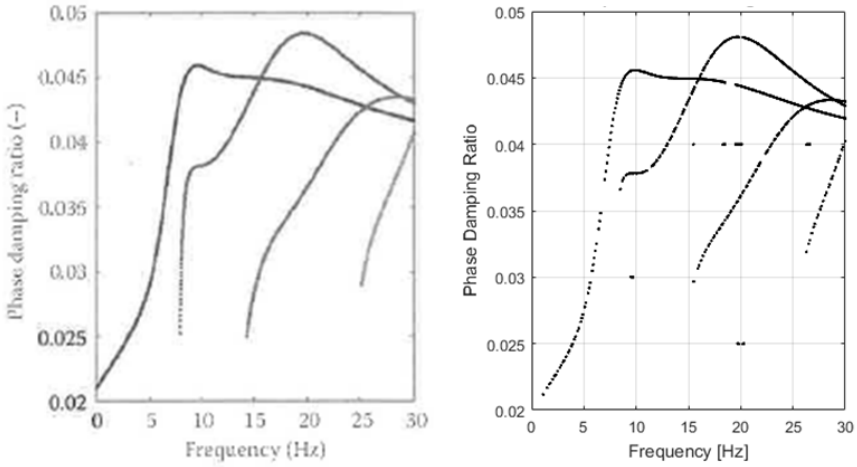

Figure 6.1: Multi-modal phase damping ratio comparison. Image from S. Foti [10] [shown left], attenuation curves computed by the author [shown right]

6.2.2 Half-Bandwidth

The next verification case that was considered was the first test case from [3].

Table 6.2: S.A. Badsar regular test case soil profile for attenuation curve comparison.

Layer	Thickness [m]	Cp [m/s]	Cs [m/s]	ζ_p	ζ_s	$\rho[Mg/m^3]$
1	2	300	150	0.04	0.04	1.9
Half-space	∞	500	250	0.025	0.025	1.9

Note that since we are measuring a spatial decay (and not a time decay) the Q-factor method is used in the wavenumber direction. Therefore, the equation be-

comes:

$$\zeta = \frac{\Delta k}{k_{res}} \frac{1}{\sqrt{\gamma^{-2} - 1}} \tag{6.4}$$

Also, the attenuation curve is directly related to the damping ratio curve by:

$$A(\omega) = \zeta(\omega) k \tag{6.5}$$

Figure 6.2 shows the attenuation curve that S.A. Badsar [3] has computed using the ElastoDynamic Toolbox in Matlab and then matched by using the Q-factor method. Figure 6.3 shows the attenuation curve computed by the author using both the phase damping ratio and the half-bandwidth method. Using the phase damping ratio method the attenuation curves were calculated for all of the modes, while both in the S.A. Badsar [3] plot and the half-bandwidth method it is only computed for the fundamental mode. Overall, we see extremely good agreement in the attenuation curves and both of these methods match exactly with the plot given by [3]. Therefore, we are confident that our models work and we can implement them in an inversion technique.

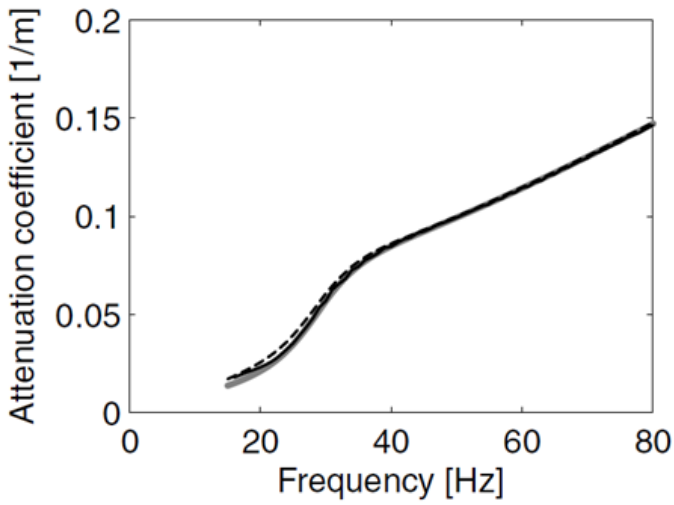

Figure 6.2: S.A. Badsar case 1 attenuation curve [3].

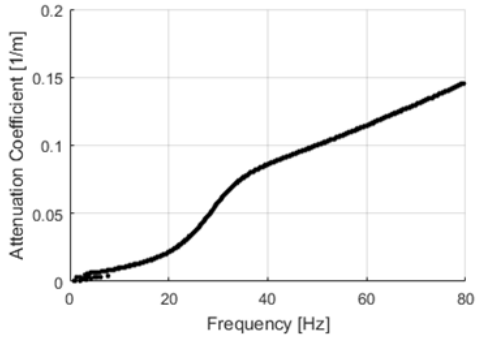

(a) Q-factor method computation of theoretical modal damping curve of fundamental mode.

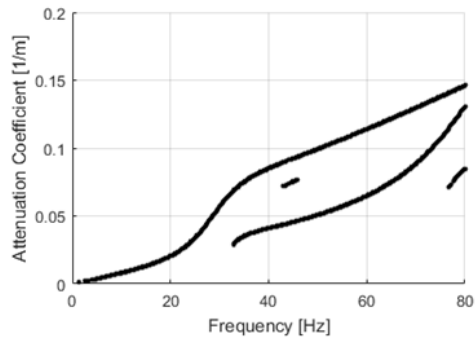

(b) Phase damping ratio computation of theoretical modal damping curve of multiple modes.

Figure 6.3: Verification of both modal damping curve computation methods.

6.3 Damping Inversion Method

The damping inversion process assumes that the stiffness profile versus depth has already been determined. The theoretical candidate that results from the stiffness inversion should have the roots lining up on the peaks of the measured response if the inversion is successful. At the very least the modes should line up with the peaks where the attenuation curve is measured for the damping inversion. The inversion will be conducted using the attenuation curve measured from the fundamental mode of the measured response spectra. Later, higher modes can also be incorporated. The undamped, elastic roots of the soil profile are calculated and the points corresponding to the fundamental mode are selected. This corresponds to the starting guess for the complex root finding algorithm in order to ensure that only the fundamental mode is used. The inversion process uses the same genetic algorithm as was used for the stiffness inversion method. The complex roots of the fundamental mode are found for each of the members of the population. The modal damping curve is calculated using the phase damping ratio method. Then, the objective function is the difference between these two curves given by equation 6.6.

$$Error = \frac{1}{N}\sum_{i=1}^{N}|D_i - D_{i,meas}| \tag{6.6}$$

Figure 6.4 shows the modal damping curves from the first three population members. The measurement algorithm will measure the distance between the measured and theoretical curves and in this case the blue curve of the second member of the population provides the best fit. Of course the population is much larger and more profiles are considered, but this is shown for illustrative purposes.

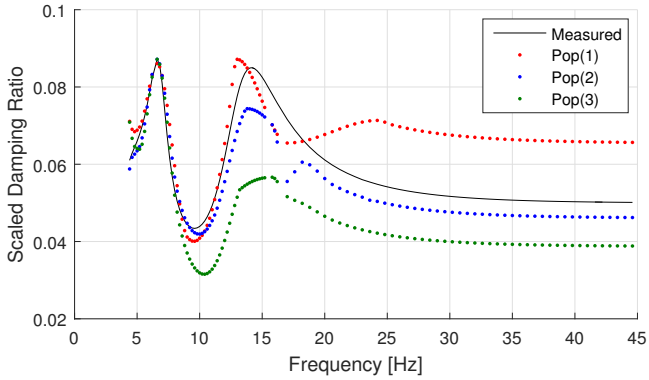

Figure 6.4: Three genetic population instances of the fundamental mode damping curves of the TC3 profile.

The theoretical curves are computed on the same frequency grid points as the measured modal damping curve in order to allow a direct comparison. In case there is an error with the root finding algorithm and any points are lost, then the damping ratio at the lost points is interpolated. For a densely sampled curve the error of losing some points is very minimal, while for a sparsely sampled curve this will introduce more errors. The interpolated curve will have a higher misfit error than the true curve for the given soil profile. This provides a soft way to discourage soil profiles that are numerically challenging while still providing a solution which is useful and can allow the inversion to proceed towards the global minimum.

When the objective function is minimized, the modal damping curve should line up exactly on the measured curve. The half-bandwidth damping inversion method proposed by [3] uses the modal attenuation curve. However, as shown by equation 6.5, this provides a linear scaling of the damping ratio curve with wavenumber. This is equivalent to providing a higher weighting of higher wavenumber points if the error function is the distance. This would increase the sensitivity of the solution to the near surface damping ratio. Hence, this inversion process will use the modal damping ratio curves as this provides a more balanced comparison.

Due to the use of the complex root finder(discussed in section 3.1.2), it is both faster and more robust to compute the complex roots at small values of damping. It was verified that scaling the entire profile with the multiplication of a scalar provides an equal scalar multiplication to the phase damping ratio curve. Therefore, a curve that is calculated with a $\zeta = 1\%$ is simply $\frac{1}{5}$ of the magnitude of a modal damping curve computed at 5%. This also means that the shape of the modal damping curve only depends on the stiffness profile (which is already fixed) and the shape of the damping profile vs depth. Figure 6.5 shows that this approximation is reasonable up to 10%. The shape of the damping ratio curves remains the same and if these curves are normalized by the maximum magnitude, they almost line up on top of each other. This linear assumption is not expected to be a good assumption at high damping ratios.

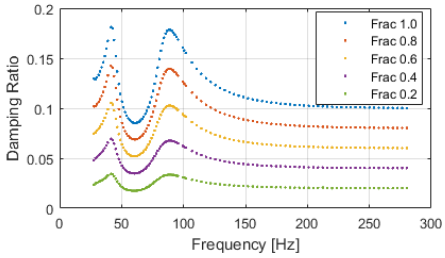

(a) Absolute damping ratio curves for multiplication of the entire damping profile by a scalar ratio.

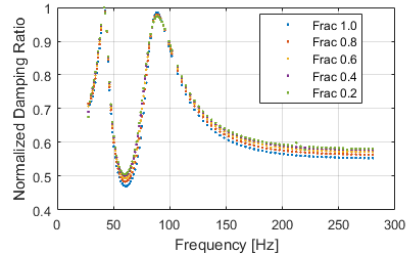

(b) Curves normalized by maximum value

Figure 6.5: Normalized Damping Ratio curves almost line up, showing the linear approximation is reasonable up to 10% damping ratio.

6.3.1 Method Testing and Adjustments

Initial runs with the genetic inversion technique indicated two major difficulties. Firstly, the suitability is very sensitive to the near surface layers. Secondly, the damping inversion is significantly slower than the stiffness inversion since the complex root finding problem is computationally much more intensive. Although the linearization assumption speeds the root finding up significantly, the process is still rather slow. An inversion with 50 generations and 60 population or 3000 candidates and only 4 soil layers takes 13 hours. For systems with more layers, the system

matrix is much larger and computational time increases rapidly with size of the matrix, meaning damping inversion of the finely discretized soil profiles determined in Chapter 5 are computationally impractical without moving to high performance computing systems.

Testing indicated that the damping inversion problem has a more unique solution with less local minima than the stiffness inversion problem. It is possible that the problem is convex, such that a local search technique, such as gradient based optimization, could be successful. A gradient solution is less computationally intensive since it progresses towards the minimum in a smart way as opposed to a genetic algorithm that randomly guesses its way to the solution and contains much more variability. A partial visualization of the objective function was performed, by varying only two variables at a time from the reference profile given in Table 6.3.

Table 6.3: TC3 soil profile with varied damping.

Layer	Thickness [m]	Cp [m/s]	Cs [m/s]	Dp	Ds	$\rho[Mg/m^3]$
Water	5	1500	0	0	0	1.0
1	3	1500	100	0.05	0.05	1.8
2	3	1500	200	0.035	0.035	2.2
3	3	1500	100	0.02	0.02	1.8
Half-space	∞	1500	400	0.01	0.01	2.3

Figure 6.6 shows the objective function value when the damping is varied in the top layer and in the halfspace, while the other two layers have their true value. In this case the objective function is the most sensitive to the first layer and second most sensitive to the halfspace. The figure shows that there is a very large difference in the gradient, or sensitivity, in the two layers. This characteristic that the objective function is significantly more sensitive to the damping in the first layer also holds for other soil systems. It can be easily rationalized that this is valid, since all waves, short and long, must interact with the first layer. It also appears that, at least for these two parameters, there is only one local minimum which is also the global minimum.

A brief summary will be given for the relatively unsuccessful local optimization inversion methods that were attempted, before introducing what was found to be an acceptable solution. This first attempt used a steepest-descent gradient method with a fixed and then with a decreasing step size. It was found that they could predict the damping of the first layer well but not retrieve the damping in the other layers. The first layer damping would oscillate around the correct value while other layers would not necessarily even have the gradient pointing in the correct direction, indicating

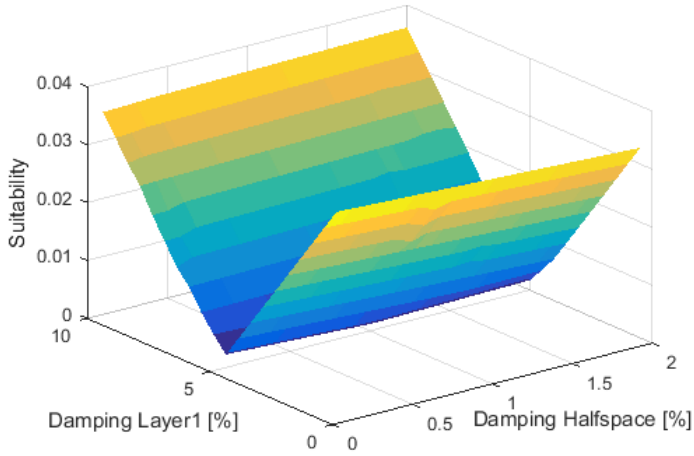

Figure 6.6: Objective function for TC3 showing high sensitivity to top soil layer.

a solution stuck in a global minimum. The next attempt was to use an optimal step size for the direction vector. This is the first step towards a conjugate gradient approach. Here the gradient vector is found while at every step an optimization is performed in order to determine the length of step in the steepest direction that gives the minimum objective function value. This was more successful, but still not satisfactory. A conjugate gradient approach was implemented next, in which the direction vector is relaxed to include some of the previous iteration direction vector. The β value, or gradient relaxation factor, was computed via the Fletcher-Reeves method [34], [24]. Strangely, the conjugate gradient method was found to give worse performance, although theoretically it should be superior or equal to the steepest descent method. This could be because the theoretical conditions on the A matrix for the use of the conjugate-gradient method are not satisfied. In our case, we do not have an A matrix to map the unknown damping profile to a set of measurements via $Ax = b$. Rather it is a process of finding and measuring roots which gives a non-linear relationship between parameters and measurements. Nonetheless, the technique was used in a similar scenario [34].

The last local optimization approach that was attempted was a very simple and 'crude' method, but was the most successful. This involves estimating the damping one layer at a time starting with the top layer and working to progressively deeper

layers. A step change is made to the damping in a layer and if the resulting objective function is lower, the new profile is kept. The step size halves with each iteration, until the algorithm moves on to the next layer. This process is in a loop, so that after all the layers have been estimated, it starts from the top layer again. This couples the layers, ensuring that errors are reduced and the solution converges towards the global minima. A slight improvement to this process was found by estimating the layers in order of most sensitive to least sensitive, which was found to be top layer and then stiffest to softest. The best result of the local optimization, obtained by this looping strategy, is shown in Figure 6.7. The damping ratio curve of the best estimate profile already matches very closely with the 'measured' damping ratio curve. The estimated profile is shown in Table 6.4. Even though the the curve visually matches very well and the first layer is estimated accurately, there is still a substantial error in the estimate of the damping in the lower soil layers.

Table 6.4: Damping profile of the best local optimization strategy.

Layer	$\zeta_{ref}[\%]$	$\zeta_{inversion}[\%]$	Error $[\%]$
Water	0	0	-
1	5	5.04	0.8
2	3.5	2.90	-17.1
3	2	2.52	26.0
∞	1	1.68	68.0

This local optimization fails because close to the global solution the change in suitability due to changes in deeper layers is very small and in the discrete calculations can act like local minima. Additionally, local minima are occurring, where is has been observed that changing the damping in the 'wrong' direction in a layer maybe decrease the fit error if there is an error in the damping in the other layers. The figure 6.8a is created by varying layers 2 and 3, with a small $+2\%$ error in the damping in layer one. It can be seen that the objective function minima is in the 'wrong' place, and that a small error in the estimation of the damping in the first layer could lead to a relatively large error for the lower layers. This is compounded if the root positions cannot be refined in the root finding tool. Then the suitability function becomes much more rough exhibiting misplaced local minima. This is shown in figure 6.8b.

The visualizations were made to understand the poor success of the local optimization strategies. The problem, appeared at first sight to be convex, but fails to converge on the correct values. This is attributed to the fact that the sensitivity is drastically different for the different layers. Although the first layer is predicted well,

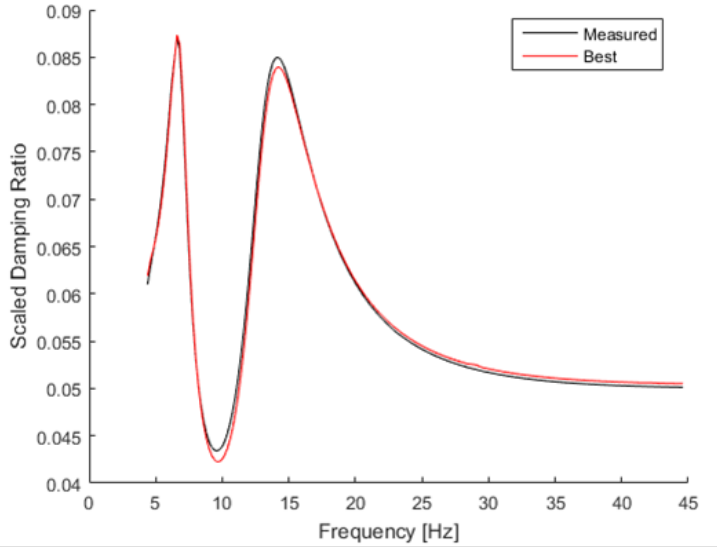

Figure 6.7: The synthetic and estimated damping ratio curves match closely even though there is significant error in the estimated soil profile.

the other layers are not resolved because there is not enough sensitivity to reach the correct solution. Perhaps the local schemes would have worked effectively if optimization toolbox licenses had been available, but time was insufficient to make this determination. Therefore, a solution should be found that addresses both the high sensitivity of the first layer dominating the solution and the long runtime of the genetic inversion.

6.3.2 Wavelet Compression

The challenges with the damping inversion process can be summarized into two core problems. Firstly, the solution is highly sensitive to the first layer damping ratio and poorly sensitive to the damping ratios of the lower layers. Secondly, the inversion process takes a long time due to the computationally expensive root finding process.

From figure 6.7 we see that there is still some small error at the peaks and troughs. These are the points that must be matched exactly if we are to find the correct profile. The problem is that there is too many additional points and so the small distance error at these relatively few but crucial points is hardly noticeable in

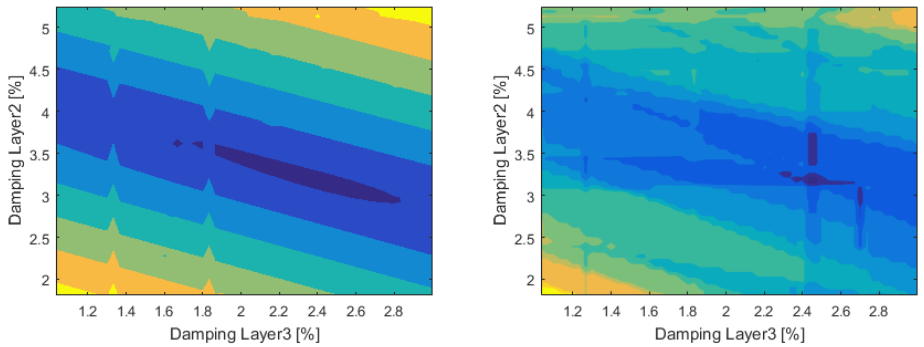

(a) Objective function shows local minima.

(b) Objective function without root refinement optimization is more chaotic, with more local minima.

Figure 6.8: Partial visualization of the objective function with $+2\%$ error in Layer 1

the average misfit value. If a smarter selection of points is used, then we can retain only the points that are crucial to the solution. These are the points near positions of high curvature. This reduces the number of points computed, speeding up the computation, and makes the objective function more balanced, because changes in the deeper layers are represented by a relatively bigger fraction of the points.

The wavelet compression scheme [16] is used to select an intelligent subset of the points where the resolution is needed because there is high curvature. The scheme starts with the full grid, as shown in figure 6.9a and removes every odd point (blue points). An intermediate compression resolution level is shown in Figure 6.9b. The linear approximation between the remaining even points, shown in black in Figure 6.9b, is used to compute the approximation at the x-axis location of the odd points. If the distance between the approximation and the actual point is below a specified distance tolerance, the points are discarded (blue, no circle). If the distance is greater than the tolerance, then those points are kept (blue, red circle). In this way the points are kept where the linear approximation cannot match the original curve within the tolerance (red circles). The even points become the new grid on the coarser resolution level and this process repeats until the coarsest resolution is reached with only two or three points in the even grid. All the points that were marked for keeping are kept along with the final even grid. This becomes the compressed subset. For this application the data for reconstructing the original curve is

discarded and only the reduced points are kept. This compression is done on the theoretical model with uniform material damping for the phase damping ratio vs frequency. By doing it on the model, instead of on the measured curve, this ensures that we capture the controlling points where the model is sensitive and must be matched to the measured data. The real wavenumbers corresponding to the kept frequencies are kept and these form the elastic root guess.

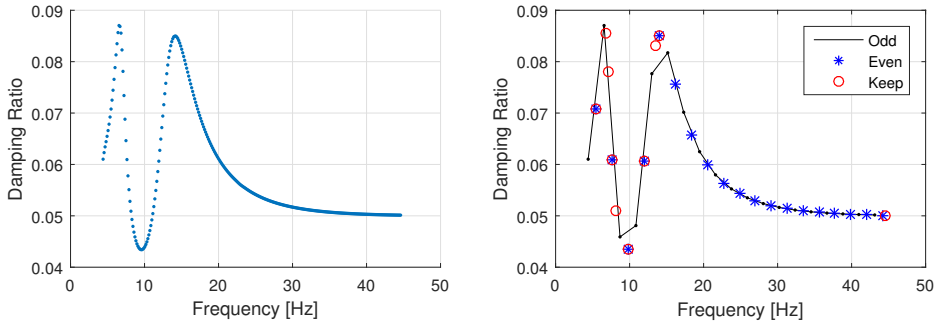

(a) Original damping ratio curve with full resolution.

(b) Intermediate resolution level of compression.

Figure 6.9: Wavelet compression on TC3 damping ratio curve.

The success of this strategy will be discussed by considering two synthetic inversion cases in the next section.

6.4 Synthetic Inversion

In this section two case studies are considered. It is shown that the damping inversion technique can accurately estimate the damping profile for the synthetic cases.

6.4.1 TC3 Damping Inversion

It was chosen to perform a synthetic inversion for the TC3 profile, with a damping profile that decreases with depth. Table 6.3 on page 125 summarizes the properties.

The genetic algorithm is the same as was used for the stiffness inversion and is described in Chapter 5. The dynamic re-ranging is not possible in a simple way due

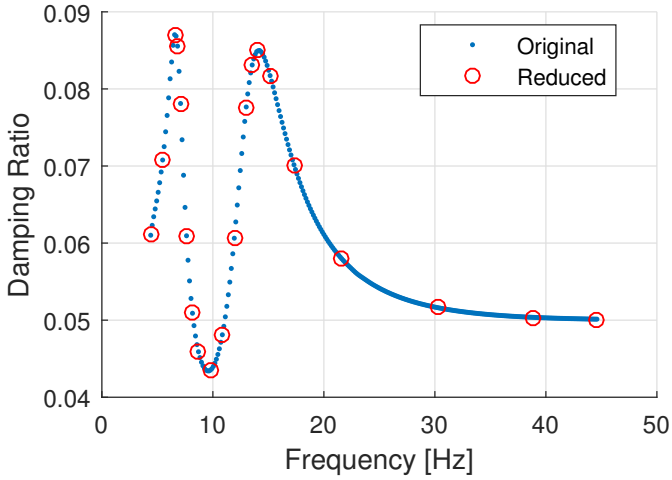

Figure 6.10: Modal damping ratio curve before and after full wavelet compression reduction.

to the linearisation assumption on computing the damping profiles. The inversion settings that are used are summarized in table 6.5.

Table 6.5: Damping inversion settings for the synthetic TC3 profile.

N_{gen}	N_{Pop}	N_{Dad}	N_{Con}	p_{FM}
100	240	80	35	0.25

The rootset contains 20 points that were obtained using the wavelet compression technique and corresponds exactly to the red circles shown in figure 6.10. The inversion resulted in a good estimate of the true damping profile. Figure 6.11 shows that the two modal damping ratio curves match very well. Figure 6.12 shows some statistics related to the estimation population. The maximum, minimum and mean values of the top 15% of the population are shown with the true and best profiles as well. It can be seen that the estimation range for the top layer is very small while it increases slightly for the lower layers, indicating a larger uncertainty or a lack of convergence. It could still be beneficial to use a larger population size in order to generate more consistency among the top population. Although the best profile has a very small prediction error in all the layers, this is not true for all the top 5

candidates and a different run may not always be so lucky with the best candidate. Table 6.6 shows the numeric values for some of the results, both in the absolute value of damping and in a percentage error to the reference profile.

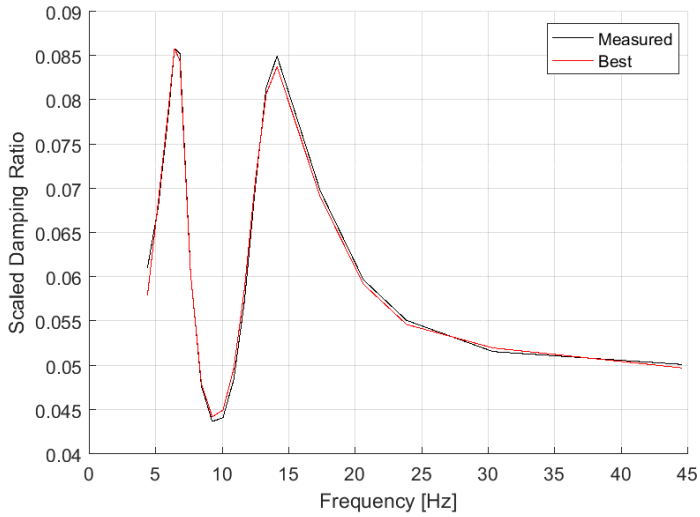

Figure 6.11: Modal damping curve of estimated damping profile shows excellent agreement with the synthetic damping ratio curve.

6.4.2 TC5 Damping Inversion

The next test case considers a new profile, test case 5 (TC5). The profile summary is given in table 6.7. This is a typical dispersive soil profile where the soil stiffness increases with depth. An unusual damping profile is assumed for the reference profile to determine if the algorithm can also estimate a staggered damping profile

The wavelet compression scheme was used on the theoretical rootset to reduce it to 20 points. Otherwise the same settings were used as for the previous damping inversion and are shown in table 6.5.

This inversion had a clear issue, where one of the starting root points consistently led to incorrectly computed modal damping ratio for one of the points in the curve. This is seen in the discontinuous dip in the modal damping ratio curve, which is shown in figure 6.13. The rest of the curve for the best profile matches very well, but near this error the fit is poor. Since the incorrect value is lower than it should

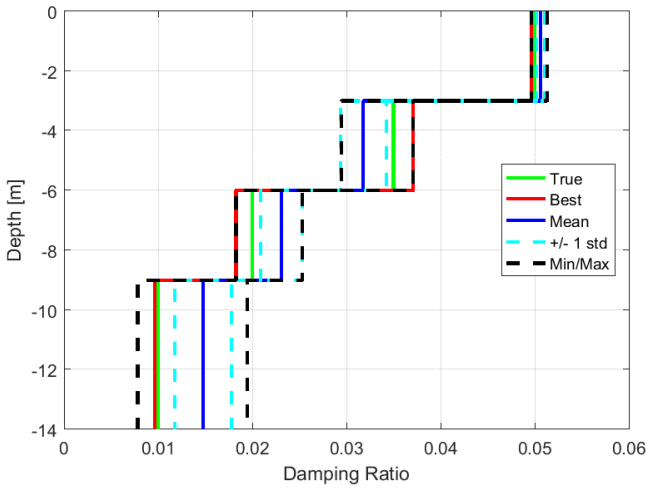

Figure 6.12: Summary of damping profile estimates for the inversion of the TC3 profile.

Table 6.6: Summary of 5 best damping inversion profiles for the synthetic TC3 inversion.

Damping Profiles of Best 5 Candidates						
	True	Top(1)	Top(2)	Top(3)	Top(4)	Top(5)
Layer 1	5.0	5.0	5.0	5.0	5.1	5.1
Layer 2	3.5	3.7	3.6	3.3	3.1	3.1
Layer 3	2.0	1.8	2.0	2.1	2.4	2.4
Halfspace	1.0	1.0	0.8	1.4	1.6	1.6

Percentage Error of Best 5 Candidates						
	True	Top(1)	Top(2)	Top(3)	Top(4)	Top(5)
Layer 1	-	-0.8	0.7	0.7	1.7	1.7
Layer 2	-	6.0	3.3	-4.8	-12.0	-12.0
Layer 3	-	-8.6	0.4	6.3	18.7	18.7
Halfspace	-	-3.5	-21.6	42.0	63.8	63.8

be, it forces the theoretical estimate to have a higher damping in the lowest layers

Table 6.7: Parameters for the TC5 profile with variable damping.

Layer	Thickness [m]	Cp [m]	Cs [m]	ζ_p	ζ_s	$\rho[Mg/m^3]$
Water	5	1500	0	0	0	1.0
1	3	1500	100	0.05	0.05	1.8
2	3	1500	200	0.035	0.035	2.2
3	3	1500	100	0.02	0.02	1.8
Half-space	∞	1500	400	0.01	0.01	2.3

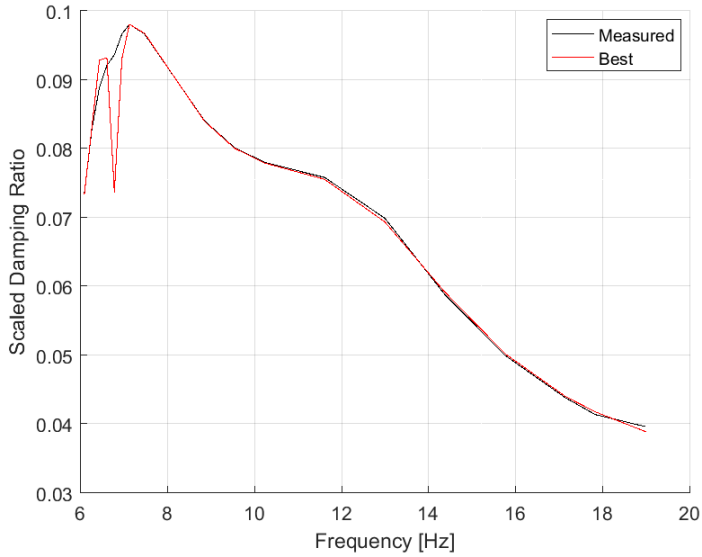

Figure 6.13: Modal damping curve of estimated damping profile shows good agreement with the synthetic damping ratio curve except for the single outlier point.

than it should.

Figure 6.14 shows that even with this error the first layer damping estimate is extremely close. The lower layer, especially the halfspace, has a very incorrect damping value. This is due to the easily noticeable error.

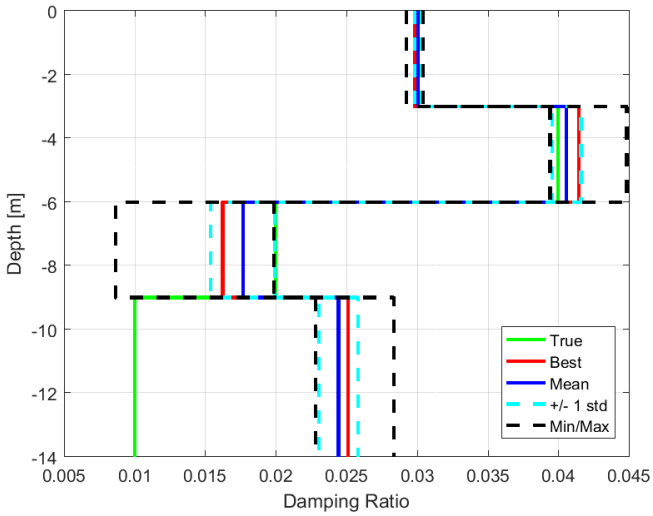

Figure 6.14: Summary of damping profile estimates for the inversion of the TC5 profile.

Table 6.8: TC5 Synthetic Damping Inversion Results.

Damping Profiles of Best 5 Candidates						
	True	Top(1)	Top(2)	Top(3)	Top(4)	Top(5)
Layer 1	3.0	3.0	2.9	3.0	3.0	3.0
Layer 2	4.0	4.2	4.5	4.1	4.2	4.1
Layer 3	2.0	1.6	0.9	1.6	1.6	1.6
Halfspace	1.0	2.5	2.8	2.5	2.6	2.5
Percentage Error of Best 5 Candidates						
	True	Top(1)	Top(2)	Top(3)	Top(4)	Top(5)
Layer 1	-	-0.6	-2.5	-0.3	-0.9	0.4
Layer 2	-	3.6	12.1	3.0	4.3	2.4
Layer 3	-	-18.8	-56.8	-18.4	-22.2	-19.0
Halfspace	-	151.3	183.7	154.0	158.0	153.6

6.5 Gjøa Damping Inversion

Some preliminary modal damping curves have been extracted from the f-k spectrum using the half-bandwidth method. The f-k spectrum was made with FFT and discrete Hankel transformation (DHT) for time and space respectively. There is a lot of noise in the spectrum, which leads to a large scatter in the extracted datapoints. Hence, the curves are taken as a smoothed version of the raw datapoints.

The removal of the windowing effect, as performed [3], via a frequency dependent exponential window has not been performed yet. Therefore, the modal damping curves are not directly comparable to the theoretical curves and may overestimate the damping. The modal damping values are very high, especially for the low frequency content in the modes. This could be due to the signal to noise ratio degrading since this occurs where the visibility of the modes are disappearing in the spectrum due to a lack of energy at the lowest frequencies. However, theoretical modal damping curves for soil profiles with approximately linear increase in stiffness do exhibit the same type of shape with a large increase in the modal damping ratio near the low frequency portion of the curve. Therefore, the curves are very reasonable and match the shape we expect for the estimated Gjøa stiffness profile.

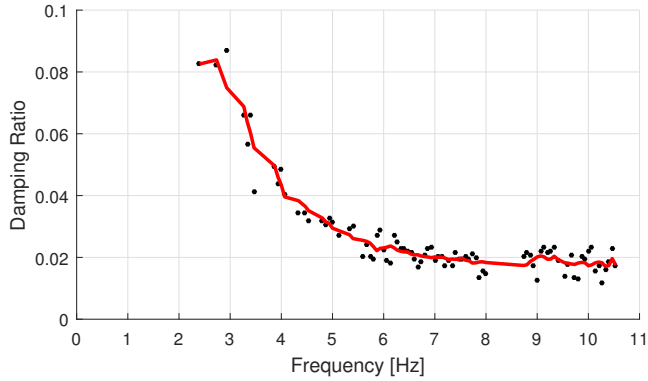

Figure 6.15: Extracted modal damping curve for Gjøa fundamental mode .

The best estimate of the Gjøa stiffness profile, shown in Table 5.11, was used as the soil profile for the damping inversion. Initially, the method is to compute the modal damping curve from a uniform damping. The shape should already roughly match the shape of the measured modal damping curve. Then, this theoretical modal damping curve is compressed using the wavelet compression technique described in

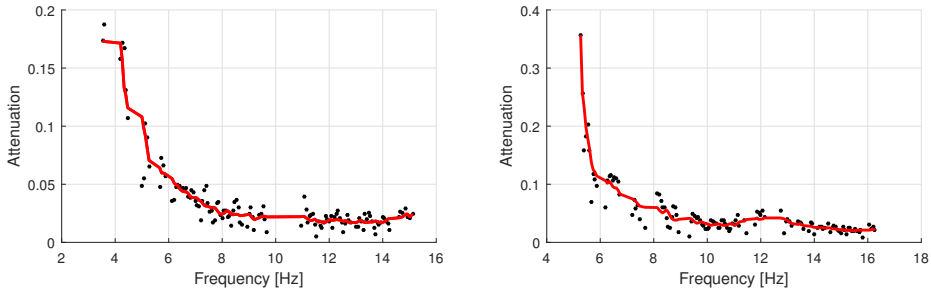

(a) Modal damping of first higher mode. **(b)** Modal damping of second higher mode.

Figure 6.16: Modal damping curves for higher Gjøa Modes.

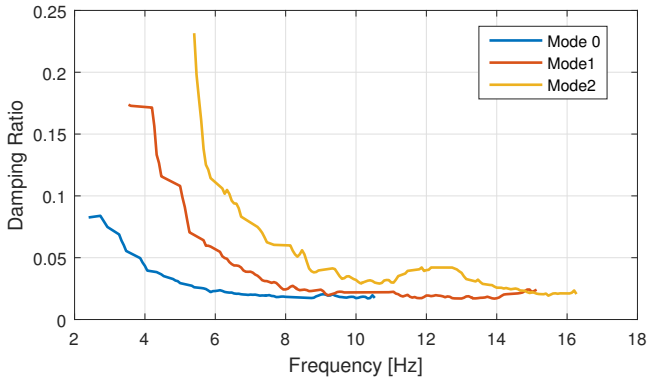

Figure 6.17: Extracted modal damping curves for Gjøa site.

section 6.3.2. The reduced set of points is then used for the damping inversion using the genetic algorithm.

Unfortunately, it was not possible to give an estimate for the Gjøa damping profile due to a failure of the root finding tool meaning that the complex roots could not be reliably determined. As an example, the 'found roots' of the uniformly damped profile are shown in Figure 6.18. These correspond to using the best and the mean soil profiles from the final stiffness inversion, as shown in Table 5.11. The discontinuous behaviour is clearly not correct and these theoretical modal damping curves do not match our expectations. The reason for the failure of the complex root finding

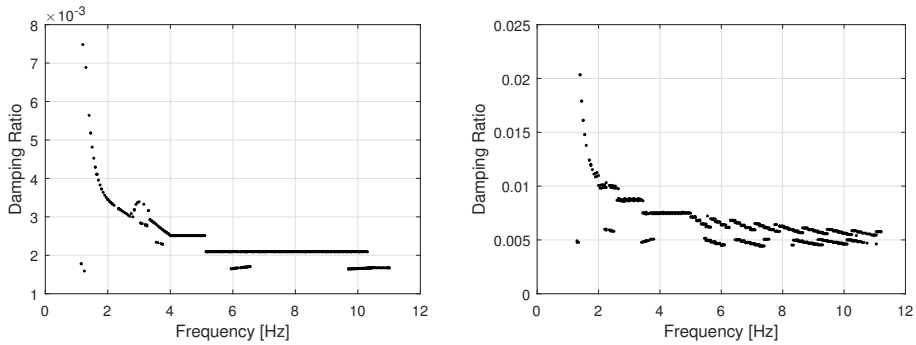

(a) Fundamental mode damping ratio curve for best stiffness profile.

(b) Fundamental mode damping ratio curve for mean stiffness profile.

Figure 6.18: Erroneous modal damping curves for fundamental Gjøa mode

tool could not be located in the time available. It is possible it is located to having a soil system with more layers, as all of the test cases, on which it worked without problems, had a few number of layers.

6.6 IJsselmeer Damping Inversion

A damping estimation from the IJsselmeer data will be difficult. Only a small portion of the fundamental mode is clean enough that it is plausible to extract the modal damping ratio curve. The result of a preliminary extraction is shown in Figure 6.19. The exponential windowing should still be applied, so the damping ratio shown here is likely to be somewhat overestimated. However, the scaling and windowing decrease the width of the peaks in the spectrum and decrease the measured damping, so these effects may counteract each other.

It is noticeable that the modal damping ratio is very high. It is considered likely that the soil damping for this site is indeed quite high. However, it would be too early to make any judgements about the amount of damping, since the material damping (soil property) values are not directly related to the modal damping values. The frequency range of the extracted modal damping curve may correspond to a location of the theoretical damping ratio curve where the damping is significantly amplified compared to material damping values. This can easily be seen by considering the low frequency portion of the curves in Figure 6.17.

A successful damping inversion should first be performed on the Gjøa data in order to verify that the damping inversion method also works on real measured data. Then an attempt can be made to estimate the damping from the IJsselmeer site.

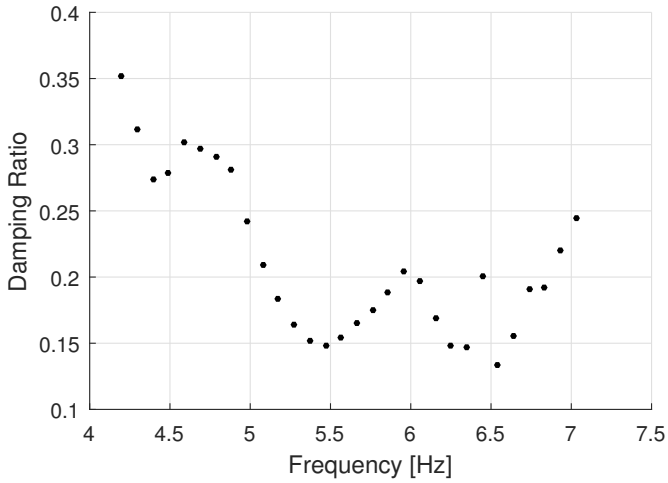

Figure 6.19: IJsselmeer fundamental mode extracted modal damping ratio.

Chapter 7

Conclusions

An analytical forward model was used to test the sensitivity of dispersion curves to various factors including damping and model discretization. A modal surface wave inversion technique was developed and used to estimate the soil stiffness profile from the Westermeerwind offshore wind farm in the IJsselmeer and the Norwegian sector of the North Sea at the Gjøa site. A damping inversion method is developed which performs well in retrieving the soil damping profile from synthetic measurements. From these results, the following is concluded:

Model studies

- The thickness of the layers in the theoretical soil model must be fine enough to accurately capture the dispersion behaviour for the range of wavelengths that are modelled. The thickness of the shallowest layers in the model should be at least $2-4$ times smaller than the smallest wavelength which is considered.

- Damping has a predictable impact, causing a smooth shift in the modal root locations. For damping up to 10%, the shift in the real part of the wavenumber is a decrease of approximately 2%. This is considered to be acceptably small in order to use a decoupled inversion approach. If damping inversion indicates a high level of damping, an iteration or correction to the soil stiffness profile could be performed in order to achieve more accurate results.

- The dispersion curves are highly sensitive to the shear wave velocity, especially near the surface. This is beneficial for identification of the shear wave velocity.

However, it is also fairly sensitive to the chosen layer thicknesses and an incorrect a-priori choice may be a confounding parameter for a stiffness inversion. Therefore, it may be unwise to estimate the layer thicknesses from the CPT measurements, since the surface wave array samples a much larger section of the soil and the thicknesses which are estimated from the CPT may not be representative of the layering in the entire array, especially if there is significant lateral variability.

- Soil deposits which have a continuous variation of the shear stiffness with depth exhibit smooth dispersion curves. Sharp bends or kinks in the dispersion curves are indicative of a layered soil deposit with sharp transitions or jumps in the shear wave velocity profile.

Stiffness inversion

- The objective function of the genetic algorithm is formulated based on the determinant of the soil coefficient matrix. Since the determinant can vary by many orders of magnitude, a normalization was developed for the determinant which makes the values more comparable, and all within the same order of magnitude. This allows a wide velocity range to be specified in the inversion. This normalization is based on finding the characteristic relationship between the value of the determinant and the phase velocity for every soil profile.

- The modal surface wave inversion method, which uses the genetic algorithm, is shown to have excellent performance in predicting the stiffness profile from synthetic measurements. Layer stripping is found to improve the estimate for the synthetic inversions.

- Modal surface wave inversion results in a reasonable, valid prediction for data collected from the Westermeerwind offshore wind farm in the IJsselmeer. This validity of the estimated profile is shown with the predicted dispersion curves and spectrum agreeing reasonably well with the measured roots and spectrum. This stiffness profile agrees well with a published SCPT estimate for the same site, although there is a different profile predicted for the first 7m. The inversion is also subject to some non-unique character and the estimated profile has a relatively large range within which it could lie. This could be indicative of high lateral variability at the site or could be due to insufficient quality of the measured data.

- The modal surface wave inversion method results in an excellent prediction of the soil stiffness profile at the Gjøa site, with a high degree of certainty for

the first 15m of soil. The validity of the estimated profile is shown by the very good match between the fundamental mode of the measured and predicted dispersion curves, although the higher modes do not directly correspond. The stiffness profile predictions agree well with already published stiffness inversions for the same site.

Damping inversion

- A method was developed which is successful at retrieving the soil damping profile from a synthetic measurement. This method uses a modified half-power bandwidth method to calculate the modal damping curve from the measured response spectrum. An inversion problem is then solved to determine the damping profile which matches this modal damping curve. The theoretical modal damping curves of the trial candidates are computed by finding the complex roots and using the phase damping ratio relationship.
- The damping inversion problem was found to have an high sensitivity to the damping in the shallowest layer. This degraded the ability to predict the damping of the lower layers. In order to improve the sensitivity of the objective function to the lower layers, a wavelet compression is performed on the modal damping curve. This captures the shape of the modal damping curve efficiently and retains the points where the highest change occurs. This also makes the inversion algorithm significantly more efficient as only $5 - 10\%$ of the points in the original curve are retained, so the computation time is similarly reduced to $5 - 10\%$ of the time it would otherwise take.
- Two synthetic damping inversions are performed. The first case led to an accurate retrieval of the damping profile, especially for the shallowest layers. The second case suffered from a visually obvious outlier in the theoretical modal damping curve, which caused a systematic error in the estimation of the damping in the lower layers. The damping in the upper layers was still well estimated and the technique would probably also lead to a good estimation if the outlier was removed.
- Modal damping curves were extracted for the Gjøa and IJsselmeer sites. However, a damping inversion could not be performed for either site because the complex root finding tool was not robust enough to produce accurate theoretical modal damping curves.

Chapter 8

Recommendations

The stiffness inversion obtains good estimates of stiffness profiles from measured data while the damping inversion method shown is very promising based on synthetic inversions. However, both the stiffness and damping inversion processes can be improved. Certainly, a more robust approach is needed for finding the complex dispersion curves, in order to allow for the estimation of the damping from the Gjøa and IJsselmeer locations. This chapter summarizes some improvements which can be made.

Stiffness inversion

- Systematic testing of all the inversion algorithm settings should be performed. There are a lot of factors and settings which go into the inversion and can have an effect on the level of success achieved by the inversion. This includes the probability of mutation, the number of generations run, the number of population members, the number of contestants, dynamic re-ranging, layer stripping and many other settings. In order to extract the most from the inversion and ensure that the best settings are chosen, a series of systematic tests need to be performed to assess the actual impact that each setting has.
- The best settings should be found for the normalization of the determinant. Currently, the smoothing is performed over 5 samples (a small number) because testing found this to produce a normalized determinant with the most similar magnitude throughout the f-k grid. However, having more variation in the normalized determinant may actually also improve the ability of the objective function to distinguish between close and further away candidates. This may lead to a better fit of the dispersion curves, especially for higher modes.

Therefore, the settings for normalizing the determinant should be tested, especially for the number of samples over which the moving average is taken. It is also possible that the inversion will perform better if the normalization takes place at fixed radial locations, for example $25, 50, 75\%$ of R_{max} rather than three random locations within the $25 - 100\%$ range.

- The classic misfit function discussed in section 3.3.1 should be implemented. This could either be used as a comparison to the determinant misfit function or in a combined hybrid approach in order to improve the fit of the higher modes. Fitting the higher modes is required in order to perform a multi-modal damping inversion.

- The uncertainty level, once is it reduced as far as possible, should be characterized. It is difficult to characterize the uncertainty [10] because there are many non-linear steps in the inversion process. For example, how is does the subjective picking of the roots or the settings used for normalizing the determinant affect the error? A bayesian inversion approach could be performed in which uses some a priori assumptions about the errors to determine a posterior distribution of errors. However, it may be difficult to make these a priori assumptions about the error and as in the case of the IJsselmeer, it is not even clear what the sources of error could be. Errors can be either aleatory (related to uncertainty in measurements) or epistemic (related to modelling errors) [10]. Suffice to say, accurately characterizing the uncertainty will be a significant challenge but also provides a lot of value in terms of allowing these measurements to be certified and used for design applications.

Damping inversion

The damping inversion method is promising and work should continue in order to estimate the damping profiles for the Gjøa and IJsselmeer sites.

- The complex root finding strategy must be improved. The current root finding tool is not robust enough to allow inversion of the damping. This could be done in a couple ways:
  - The current root finding strategy could be 'fixed' and kept. The linear property of the modal damping curve, shown in Figure 6.5, can be incorporated to define a better estimated search region in the complex plane, leading to a speed-up of the method. This is perhaps the most tempting approach, especially if an easy 'fix' can be found. However, this is not recommended since it is eventually expected to lead to errors or simply an

inefficient process. Instead the time should be taken to find a new, more elegant method for identifying the roots of arbitrary soil systems.

- The equations in the soil system or coefficient matrix could be linearized around the appropriate point. These linearized equations can be solved more easily to identify the approximate complex root locations which are valid for small values of damping [14].
- The method proposed by [14] which is based on the Cauchy residue theorem of complex analysis could be implemented. This method is valid for arbitrary (including very high) values of the soil damping. Hence, in soils with large amounts of damping this will provide more accuracy than the linearization approach.

Of these three options, it is recommended to uses the residue theorem, if the mathematics is manageable. Otherwise, the linearization approach should be used.

- Sensitivity studies should be performed to test the effect of various disturbing factors on the inversion results. For example, what is the effect of an identification error in the stiffness profile and how does this affect the estimated damping? These are important questions to answer if the process is to be used for estimating real measurements which are subject to modelling and measurement errors.

- Additional processing could be performed on the Gjøa data in order to remove the noise in the f-k spectrum. This would improve the quality of the extracted modal damping curves and give more certainty in the inversion process. Exponential windowing should be applied in order to reduce or remove the effect of the apparent increase in damping due to the spectral leakage caused by the rectangular window.

- Once the damping inversion process works reliably for the Gjøa site fundamental mode, the approach should be extended to perform inversion for the higher modes. The Gjøa dataset is remarkably good with many modes clearly visible in the response spectrum. Having this data affords the opportunity to identify the actual frequency dependency of the damping. To the knowledge of the author, the frequency dependency of damping has never been identified from surface wave measurements, so this would offer a unique and very interesting contribution to research if it could be done.

- The damping profile should be estimated for the IJsselmeer site. This will be tricky due to the lower quality of the data as compared with the Gjøa data, so this should only be attempted if the Gjøa damping inversions are considered successful. It may be required to try other damping inversion methods in order to successfully estimate the damping profile. It may also be possible that a successful inversion is not possible due to the data quality and that new measurements should be taken with a more appropriate experimental setup.
- As with the stiffness inversion, the uncertainty or error associated with the damping profile should be characterized. Since an inversion has not been successfully completed on real measurements, it is too early to discuss the methods for characterizing the uncertainty. However, it is again not expected to be a trivial task, although, it is certainly important for the long term adoption of this method for industry use.

Appendix A

Complex Stiffness and Damping Ratio

Single Degree of Freedom

We can derive a damping ratio for a soil system with an analogy to a single degree of freedom mass spring damper system. In a single degree of freedom we have the well known governing equation

$$m\ddot{u} + c\dot{u} + ku = F \tag{A.1}$$

If a harmonic load is considered, then it can be shown that such a system has a harmonic response which is out of phase with the input but occurs with the same frequency. The assumed forms for the force and displacement are then given as:

$$F = F_o e^{i\omega t} \qquad u = u_o e^{i\omega t - \phi} \qquad \dot{u} = u_o i\omega e^{i\omega t - \phi} \qquad \ddot{u} = -u_o \omega^2 e^{i\omega t - \phi} \tag{A.2}$$

The work done per cycle is the closed loop integral of the force over the cycle.

$$\Delta W = \oint_c F du = \int_0^T F \frac{du}{dt} dt = \int_0^T (m\ddot{u} + c\dot{u} + ku)\dot{u} dt \tag{A.3}$$

The displacement and its derivatives in A.2 are substituted into A.3.

$$\Delta W = \int_o^T ((k - \omega^2 m) + i\omega c)(u_o e^{i\omega t - \phi})(i\omega u_o e^{i\omega t - \phi}) dt \tag{A.4}$$

The mass and stiffness terms integrate to zero, which is expected as they do not remove energy from the system. This is shown by considering that the integral of two orthogonal harmonics over one cycle is zero.

$$\oint sin(\omega t)cos(\omega t)dt = 0 \text{ and hence also } \oint e^{i\omega t}ie^{i\omega t} = 0 \tag{A.5}$$

Thus

$$\Delta W = -\omega^2 c u_o^2 \int_0^T e^{i\omega t-\phi}e^{i\omega t-\phi}dt \tag{A.6}$$

The integral of a squared harmonic over its period is known to be

$$\int_0^T cos^2(\omega t)dt = \int_0^T e^{2(i\omega t)}dt = \frac{T}{2} \tag{A.7}$$

Hence, equation A.6 becomes A.8 which is the work energy lost due to damping in one cycle.

$$\Delta W = -\omega^2 c u_o^2 \frac{T}{2} = -\pi c u_o^2 \omega \tag{A.8}$$

The maximum energy stored in one cycle is given by:

$$W = \frac{1}{2}k u_o^2 \tag{A.9}$$

$$\frac{\Delta W}{W} = \frac{\pi c u_o^2 \omega}{\frac{1}{2}k u_o^2} = \frac{4\pi\omega^2 m}{k}\frac{c}{2\omega m} = 4\pi\zeta = 4\pi D \tag{A.10}$$

Hence, we can see that the damping ratio, ζ, for a single degree of freedom system is given by:

$$\zeta = \frac{1}{4\pi}\frac{\Delta W}{W} \tag{A.11}$$

Soil system

The soil system damping ratio is derived in the same way, using the knowledge of equation A.11. The derivation below shows hysteretic damping using the complex stiffness principle where the loss factor η defines the ratio of the imaginary stiffness (ie damping) to the real stiffness and the shear strain is given by $\gamma = \gamma_o e^{i\omega t-\phi}$.

$$\tau = \tau_o e^{i\omega t} = \mu^* \gamma_o e^{i\omega t-\phi} \text{ where } \mu^* = \mu + i\mu = \mu(1+i\eta) \tag{A.12}$$

The work extracted per cycle

$$\begin{aligned}\Delta W &= \oint_c \tau du = \int_0^T \tau \dot{u} dt = \int_0^T \mu(1+i\eta)(\gamma_o e^{i\omega t-\phi})(i\omega\gamma_o e^{i\omega t-\phi}) \\ &= -\mu\eta\omega\gamma_o^2 \int_0^T e^{2(i\omega t)} dt = -\mu\eta\omega\gamma_o^2 \frac{T}{2} = -\mu\eta\pi\gamma_o^2\end{aligned} \tag{A.13}$$

The maximum energy stored per cycle

$$W = \frac{1}{2}\mu\gamma_o^2 \tag{A.14}$$

The damping ratio

$$D = \zeta = \frac{1}{4\pi}\frac{\Delta W}{W} = \frac{\eta\pi\mu\gamma_o^2}{4\pi\frac{1}{2}}\mu\gamma_o^2 = \frac{\eta}{2} \tag{A.15}$$

Hence, we see that the loss factor (or complex stiffness ratio) is directly related to the soil damping ratio.

$$D = \zeta = \frac{\eta}{2} \tag{A.16}$$

Appendix B

Modified Half Power Bandwidth Derivation

This Appendix shows the derivation of the half-power bandwidth method, including the modification for the amplitude ratio at which the spectral width is measured. It is also derived for hysteretic damping. The symbolic computations were performed using Maple.

The half-power bandwidth or Q-factor method is a method for determining the damping ratio of a dynamic system. The damping ratio of the system is directly related to the width of the energy spectrum and is measured at half the height of the peak or at $\frac{1}{\sqrt{2}}$ for the amplitude spectra since energy is proportional to the square of the amplitude.

First, the half power bandwidth method will be derived for a single degree of freedom mass-spring-damper system with viscous damping. Then, the modification will be performed for the relationship not at the half-power height. Finally, the derivation will be extended to use hysteretic damping instead of viscous damping. Although the shape of the theoretical response spectra are different, it is shown that viscous and hysteretic damping have the same Q-factor formulation.

Half-power bandwidth

A single degree of freedom mass-spring-damper system with viscous damping

has governing equation given by

$$m\ddot{x} + c\dot{x} + kx = F \tag{B.1}$$

The amplitude response function is squared to give the power spectrum function

$$E = \frac{F^2}{(-\Omega^2 + \omega_o^2)^2 + 4\Omega^2\omega_o^2\zeta^2} \tag{B.2}$$

This can be differentiated, in order to find the peak

$$\frac{dE}{d\Omega} = -\frac{F^2(-4(-\Omega^2 + \omega_o^2)\Omega + 8\Omega\omega_o^2\zeta^2)}{((-\Omega^2 + \omega_o^2)^2 + 4\Omega^2\omega_o^2\zeta^2)^2} \tag{B.3}$$

We find the value of the resonant frequency solving where B.3 is equal to zero and take the positive root:

$$\Omega = \sqrt{-2\zeta^2 + 1}\,\omega_o = \omega_{res} \tag{B.4}$$

The peak energy is then

$$E_{max} = \frac{F^2}{(-(-2\zeta^2 + 1)\omega_o^2 + \omega_o^2)^2 + (4(-2\zeta^2 + 1))\omega_o^4\zeta^2} \tag{B.5}$$

We then solve the Ω at which $E = \frac{1}{2}E_{max}$ and get two positive roots

$$\Omega = \sqrt{-2\zeta^2 + 1 - 2\sqrt{-\zeta^4 + \zeta^2}}\,\omega_o\,,\ \sqrt{-2\zeta^2 + 1 + 2\sqrt{-\zeta^4 + \zeta^2}}\,\omega_o \tag{B.6}$$

Then we can compute the Q-factor

$$Q = \frac{\omega_{res}}{\Delta\omega} = \frac{\sqrt{-2\zeta^2 + 1}}{\sqrt{-2\zeta^2 + 1 + 2\sqrt{-\zeta^4 + \zeta^2}} - \sqrt{-2\zeta^2 + 1 - 2\sqrt{-\zeta^4 + \zeta^2}}} \tag{B.7}$$

We can then solve the relationship between the damping ratio and the Q-factor. We ensure that the correct root is chosen by taking the root which is positive and has Q decreasing as ζ increases.

$$\zeta = \frac{\sqrt{\frac{\sqrt{-Q^4+4Q^2+4}-2}{\sqrt{-Q^4+4Q^2+4}}}}{\sqrt{2}} \tag{B.8}$$

If the Q-factor is small then using a series expansion around $Q = 0$ we can approximate this as

$$\zeta = \frac{1}{2Q} = \frac{\Delta\omega}{2\omega} \tag{B.9}$$

Amplitude γ

The derivation is very similar, except we consider that the ratio of the amplitude where the width is measured to the height of the peak is left as an undetermined parameter γ so that an analytic expression can be derived for the relation of the damping ratio and the width for an arbitrary height. We derive it with the energy spectrum using γ_E but should note that we may prefer to evaluate the damping from the amplitude response spectra and use γ_A.

$$\gamma_E = \frac{E}{E_{max}} \quad \text{and} \quad \gamma_A = \frac{A}{A_{max}} \quad \text{such that} \quad \gamma_E = \gamma_A^2$$

We recompute B.6 instead substituting in $E = \gamma_E E_{max}$ and we get

$$\Omega = \begin{matrix} \dfrac{\sqrt{\gamma_E(-2\gamma_E\zeta^2 + 2\sqrt{\gamma_E^2\zeta^4 - \gamma_E\zeta^4 - \gamma_E^2\zeta^2 + \gamma_E\zeta^2} + \gamma_E)}}{\gamma_E}\,\omega_o\,, \\ \dfrac{\sqrt{-\gamma_E(2\gamma_E\zeta^2 + 2\sqrt{\gamma_E^2\zeta^4 - \gamma_E\zeta^4 - \gamma_E^2\zeta^2 + \gamma_E\zeta^2} - \gamma_E)}}{\gamma_E}\,\omega_o \end{matrix} \tag{B.10}$$

We calculate the Q-factor just as we did in equation B.7, although now the Q-factor has a different meaning since it needs the accompanying amplitude correction. Solving for ζ results in an extremely long expression which is not shown here. However, the series simplification becomes:

$$D = \zeta = \frac{\sqrt{\gamma_E}}{2Q\sqrt{-\gamma_E + 1}} = \frac{1}{2Q}\frac{1}{\sqrt{\gamma_E^{-1} - 1}} = \frac{1}{2Q}\frac{1}{\sqrt{\gamma_A^{-2} - 1}} \tag{B.11}$$

Hysteretic

If we instead represent the damping of the system as a complex stiffness or hysteretic damping then the governing equation changes to

$$m\ddot{x} + k(1 + i\eta)x = F \tag{B.12}$$

The power spectrum is then

$$E = \frac{F^2}{(-\Omega^2 + \omega_o^2)^2 + 4\omega_o^2\zeta^2} \tag{B.13}$$

This can be differentiated, in order to find the peak

$$\frac{dE}{d\Omega} = -\frac{4F^2(-\Omega^2 + \omega_o^2)\Omega}{((-\Omega^2 + \omega_o^2)^2 + 4\omega_o^2\zeta^2)^2} \tag{B.14}$$

We solve where B.14 is equal to zero and find that the resonant frequency is the natural frequency. This should not be that surprising since the damping is frequency independent.

$$\Omega = \omega_o = \omega_{res} \tag{B.15}$$

The peak energy is then

$$E_{max} = \frac{1}{4}\frac{F^2}{\omega_o^4\zeta} \tag{B.16}$$

We then solve the Ω at which the $E = \gamma_E E_{max}$ and get two roots

$$\begin{aligned} \Omega = & \frac{\sqrt{\gamma_E(\gamma_E + 2\sqrt{-\gamma_E^2\zeta^2 + \gamma_E\zeta^2})}}{\gamma_E}\omega_o\,, \\ & \frac{\sqrt{-\gamma_E(-\gamma_E + 2\sqrt{-\gamma_E^2\zeta^2 + \gamma_E\zeta^2})}}{\gamma_E}\omega_o \end{aligned} \tag{B.17}$$

Then we can compute the Q-factor

$$Q = \frac{\omega_{res}}{\Delta\omega} = \frac{\sqrt{-\gamma_E(-\gamma_E + 2\sqrt{-\gamma_E^2\zeta^2 + \gamma_E\zeta^2})}}{\gamma_E} - \frac{\sqrt{\gamma_E(\gamma_E + 2\sqrt{-\gamma_E^2\zeta^2 + \gamma_E\zeta^2})}}{\gamma_E} \tag{B.18}$$

We then solve the relationship between the damping ratio and the Q-factor and we can use a series expansion to approximate it as

$$D = \zeta = \frac{\sqrt{\gamma_E}}{2Q\sqrt{-\gamma_E + 1}} = \frac{1}{2Q}\frac{1}{\sqrt{\gamma_E^{-1} - 1}} = \frac{1}{2Q}\frac{1}{\sqrt{\gamma_A^{-2} - 1}} \tag{B.19}$$

Hence, we see that although the formulations are different for hysteretic and viscous damping, the amplitude correction terms for the Q-factor relationship remains the same for both cases.

Appendix C

Hankel Transformations

The derivation given in Chapter 2 is continued here in order to show the detailed steps of the Hankel Transformation of the displacement, stress and the governing equations.

Throughout this appendix, it is assumed that a few basic rules for integrating and differentiating Bessel functions are known. d_x denotes a differentiation operation with respect to x, full written out as $\frac{d()}{dx}$. This is similarly related to the partial differentiation with respect to x, which is $\partial_x = \frac{\partial()}{\partial x}$. The differentiation rules for Bessel functions are [28]:

$$d_x(x^n J_n(x)) = x^n J_{n-1}(x)$$

$$d_x(x^{-n} J_n(x)) = -x^{-n} J_{n+1}(x)$$

Note also, that since the Bessel function in the integrand of the Hankel transformation uses $k_r r$ we must also apply the chain rule:

$$\frac{\partial f}{\partial r} = \frac{\partial f}{\partial x}\frac{\partial x}{\partial r} \quad \text{where} \quad x = k_r r \quad \text{so} \quad \frac{\partial x}{\partial r} = k_r$$

Hence, it logically follows

$$d_r(r^n J_n(k_r r)) = k_r r^n J_{n-1}(k_r r)$$

$$d_r(r^{-n} J_n(k_r r)) = -k_r r^{-n} J_{n+1}(k_r r)$$

To be specific and absolutely clear, we can show that the first expression is used for transforming from J_1 to J_0 while the second is used for transforming from J_0 to J_1.

$$d_r(rJ_n(k_r r)) = k_r r J_0(k_r r)$$

$$d_r(r^0 J_n(k_r r)) = d_r(J_n(k_r r)) = -k_r J_1(k_r r)$$

C.1 Displacement

The displacement equation 2.53 is shown below.

$$\begin{pmatrix} u_r \\ u_\theta \\ u_z \end{pmatrix} = \begin{pmatrix} \partial_r \phi - \partial_z \psi \\ 0 \\ \partial_z \phi + \frac{1}{r}\partial_r(r\psi) \end{pmatrix} \tag{C.1}$$

Since there is no time dependence in the displacement equations the Fourier transformation does not add any additional terms

$$\begin{pmatrix} \tilde{u_r} \\ \tilde{u_z} \end{pmatrix} = \int_0^\infty \begin{pmatrix} \partial_r \phi - \partial_z \psi \\ \partial_z \phi + \frac{1}{r}\partial_r(r\psi) \end{pmatrix} e^{i(\omega t - k_1 x_1)} dt = \begin{pmatrix} \partial_r \tilde{\phi} - \partial_z \tilde{\psi} \\ \partial_z \tilde{\phi} + \frac{1}{r}\partial_r(r\tilde{\psi}) \end{pmatrix} \tag{C.2}$$

Notice that the vertical displacement contains a $\frac{1}{r}$ term while the radial displacement does not. In order to get the simplest form of the final equations u_r will be transformed with first order Hankel transformation while u_z will be transformed with a zero order Hankel transformation.

Radial Displacement

$$\tilde{u}_r^{H_1} = \int_0^\infty \partial_r \tilde{\phi} r J_1(r k_r) dr - \int_0^\infty \partial_z \tilde{\psi} r J_1(r k_r) dr \tag{C.3}$$

The integral contains two terms. The first must be integrated by parts using the chain rule while the second can be directly integrated.

$$\int_0^\infty \partial_z \tilde{\psi} r J_1(r k_r) dr = \partial_z \tilde{\psi}^{H_1} \tag{C.4}$$

$$\int_0^\infty (\partial_r \tilde{\phi}) r J_1(r k_r) dr = \tilde{\phi} r J_1(k_r r)\Big|_0^\infty - \int_0^\infty \tilde{\phi}(k_r r J_0(k_r r) dr) \tag{C.5}$$

The first term is zero at $r = 0$ and $r = \infty$. Hence equation C.5 becomes

$$EqC.5 = -k_r \tilde{\phi}^{H_0}$$

Recombining this gives

$$\tilde{u}_r^{H1} = -k_r \tilde{\phi}^{H_0} - \partial_z \tilde{\psi}^{H_1} \tag{C.6}$$

Vertical Displacement

The vertical displacement can be similarly transformed, but with the zero order Hankel transform.

$$\tilde{u}_z^{H_0} = \partial_z \int_0^\infty \tilde{\phi} r J_0(r k_r) dr + \int_0^\infty \frac{1}{r} \partial_r (r\tilde{\psi}) r J_0(r k_r) dr \tag{C.7}$$

The first term is directly integrable, while the second must be integrated by parts.

$$\begin{aligned} \tilde{u}_z^{H_1} &= \partial_z \tilde{\phi}^{H_0} + r\tilde{\psi} J_0(k_r r)\Big|_0^\infty - \int_0^\infty r\tilde{\psi}(-k_r J_1(k_r r)) dr \\ &= \partial_z \tilde{\phi}^{H_0} + k_r \tilde{\psi}^{H_1} \end{aligned} \tag{C.8}$$

C.2 Stress

The stresses from equation 2.57 are shown below.

$$\begin{aligned} \sigma_{zz} &= (\lambda + 2\mu)\partial_z(\partial_z \phi + \frac{1}{r}\partial_r(r\psi)) + \frac{\lambda}{r}\partial_r(r(\partial_r \phi - \partial_z \psi)) \\ \tau_{zr} &= \mu \partial_z(\partial_r \phi - \partial_z \psi) + \partial_z(\partial_z \phi + \frac{1}{r}\partial_r(r\psi)) \end{aligned} \tag{C.9}$$

The compressive stress is transformed using the zero order Hankel transformation while the shear stress is transformed using the first order Hankel transformation.

Compressive Stress

The zero order Hankel transformation of the compressive stress is expanded into four separate terms:

$$\begin{aligned}\tilde{\sigma}_{zz}^{H_0} =&(\lambda+2\mu)\partial_z^2\int_0^\infty \tilde{\phi} r J_0(rk_r)dr + (\lambda+2\mu)\int_0^\infty \frac{1}{r}\partial_r(r\tilde{\psi})rJ_0(rk_r)dr \\ &+\lambda\int_0^\infty \frac{1}{r}\partial_r(r\partial_r\tilde{\phi})rJ_0(rk_r)dr - \lambda\partial_z\int_0^\infty \frac{1}{r}\partial_r(r\tilde{\psi})rJ_0(rk_r)dr\end{aligned} \tag{C.10}$$

The first term is a simple integral, following the Hankel transformation definition. The integration of the second term and fourth term are the same integral and have already been shown with equations C.8 and C.9. The third term must be integrated by parts twice.

$$\begin{aligned}\int_0^\infty \frac{1}{r}\partial_r(r\partial_r\tilde{\phi})rJ_0(rk_r)dr &= r\partial_r\tilde{\phi}J_1(k_r r)\phi\Big|_0^\infty - \int_0^\infty r\partial_r\tilde{\phi}(-k_r J_1(k_r))dr \\ &= k_r\int_0^\infty \partial_r\tilde{\phi}rJ_0(rk_r)dr \quad \text{by parts again} \\ &= k_r r J_1(k_r r)\tilde{\phi}\Big|_0^\infty - k_r\int_0^\infty \tilde{\phi}k_r rJ_0(k_r r)dr \\ &= -k_r^2\tilde{\phi}^{H_0}\end{aligned} \tag{C.11}$$

Both of the terms which are evaluated at zero and infinity are zero and are discarded. Therefore, combining the four terms, the compressive stress equation is:

$$\tilde{\sigma}_{zz}^{H_0} = (\lambda+2\mu)(\partial_z^2\tilde{\phi}^{H_0} + k_r\partial_z\tilde{\psi}^{H_1}) - \lambda(k_r\partial_z\tilde{\psi}^{H_1} + k_r^2\tilde{\phi}^{H_0}) \tag{C.12}$$

This is the compressive stress equation in the wavenumber domain. In order to show it in a form more consistent with literature we assume the solution

$$\tilde{\phi}^{H_0} = Ae^{-q_p x_3} + Be^{q_p x_3} \quad \text{where} \quad q_p = \sqrt{k_r^2 - k_p^2} > 0 \tag{C.13}$$

then

$$\partial_z^2\tilde{\phi}^{H_0} = qp^2\tilde{\phi}^{H_0} = (k_r^2 - k_p^2)\tilde{\phi}^{H_0} \tag{C.14}$$

$$\begin{aligned}\tilde{\sigma}_{zz}^{H_0} &= (\lambda+2\mu)((k_r^2-k_p^2)\tilde{\phi}^{H_0} + k_r\partial_z\tilde{\psi}^{H_1}) - \lambda(k_r\partial_z\tilde{\psi}^{H_1} + k_r^2\tilde{\phi}^{H_0}) \\ &= -(\lambda+2\mu)k_p^2\tilde{\phi}^{H_0} + 2\mu(k_r^2\tilde{\phi}^{H_0} + k_r\partial_z\tilde{\psi}^{H_1})\end{aligned} \tag{C.15}$$

Also, recalling $Cp^2 = \frac{(\lambda+2\mu)}{\rho}$, $k_p = \frac{\omega}{Cp}$ and $Cs^2 = \frac{\mu}{\rho}$

$$\begin{aligned}\tilde{\sigma}_{zz}^{H_0} &= -\rho\omega^2\tilde{\phi}^{H_0} + 2\mu(k_r^2\tilde{\phi}^{H_0} + k_r\partial_z\tilde{\psi}^{H_1}) \quad * \\ &= \mu(-k_s^2\tilde{\phi}^{H_0} + 2k_r^2\tilde{\phi}^{H_0} + 2k_r\partial_z\tilde{\psi}^{H_1}) \\ &= \mu((2k_r^2 - k_s^2)\tilde{\phi}^{H_0} + 2k_r\partial_z\tilde{\psi}^{H_1})\end{aligned} \tag{C.16}$$

Note also that we can manipulate the isotropic stress to only be a function of the shear modulus μ. This seems strange but is valid as long as we don't erroneously use this for an acoustic layer where the shear modulus is zero. Instead we should use the equation C.16 line marked by an asterix.

$$\tilde{\sigma}_{zz}^{H_0} = -\rho\omega^2\tilde{\phi}^{H_0} \quad \text{(acoustic)} \tag{C.17}$$

Shear Stress

The shear stress equations are transformed by the first order Hankel transformation.

$$\begin{aligned}\tilde{\tau}_{zr} =&\mu\Big(\partial_z\int_0^\infty(\partial_r\tilde{\phi})rJ_0(rk_r)dr - \partial_z^2\int_0^\infty(\tilde{\psi})rJ_0(rk_r)dr \\ &+ \partial_z\int_0^\infty(\partial_r\tilde{\phi})rJ_0(rk_r)dr + \int_0^\infty\partial_r(\frac{1}{r}\partial_r(r\tilde{\psi}))rJ_0(rk_r)dr\Big)\end{aligned} \tag{C.18}$$

The first and third integrals are the same, and have been previously shown in equation C.11. The second term is directly integrable while the final term must be integrated by parts.

$$\begin{aligned}\int_0^\infty\partial_r(\frac{1}{r}\partial_r(r\tilde{\psi}))rJ_0(rk_r)dr &= rJ_1\frac{1}{r}\partial_r(r\tilde{\psi}))\Big|_0^\infty - \int_0^\infty\frac{1}{r}\partial_r(r\tilde{\psi}))k_rrJ_0(rk_r)dr \\ &= -k_r\int_0^\infty\frac{1}{r}\partial_r(r\tilde{\psi}))rJ_0(rk_r)dr\end{aligned} \tag{C.19}$$

Now the integral in equation C.19 is the same as the integral in equation C.7 and we can combine all the known integrals into:

$$\begin{aligned}\tilde{\tau}_{zr} &= \mu\Big(-2k_r\partial_z\tilde{\phi}^{H_0} - \partial_z^2\tilde{\psi}^{H_1} - k_r^2\tilde{\psi}^{H_1}\Big) \\ &= -\mu\Big(2k_r\partial_z\tilde{\phi}^{H_0} + (2k_r^2 - k_s^2)\tilde{\psi}^{H_1}\Big)\end{aligned} \tag{C.20}$$

C.3 Governing Equations

The governing wave equation given in equations 2.62 are shown here. This must also be transformed. The first equation will be transformed with the zero order Hankel transform while the second equation will be transformed with the first order Hankel transform. Both have already been transformed from time to frequency domain with the Fourier transformation.

$$\begin{aligned} -\frac{\omega^2}{C_p^2}\tilde{\phi} &= \partial_r^2\tilde{\phi} + \frac{1}{r}\partial_r\tilde{\phi} + \partial_z^2\tilde{\phi} \\ -\frac{\omega^2}{C_s^2}\tilde{\psi} &= \partial_r^2\tilde{\psi} + \partial_z^2\tilde{\psi} + \frac{1}{r}\partial_r\tilde{\psi} - \frac{\tilde{\psi}}{r^2} \end{aligned} \tag{C.21}$$

$$\begin{aligned} \int_0^\infty (-k_p^2\tilde{\phi})rJ_0(rk_r)dr = &\int_0^\infty (\partial_r^2\tilde{\phi})rJ_0(rk_r)dr + \int_0^\infty (\frac{1}{r}\partial_r\tilde{\phi})rJ_0(rk_r)dr \\ &+ \int_0^\infty (\partial_z^2\tilde{\phi})rJ_0(rk_r)dr \end{aligned} \tag{C.22}$$

Two terms are combined by recognizing the equivalent forms which can be proven using the chain rule

$$\frac{1}{r}\partial_r\tilde{\phi} + \partial_r^2\tilde{\phi} = \frac{1}{r}\partial_r(r\partial_r\tilde{\phi}) \tag{C.23}$$

The resulting integrand has already been computed by parts in equation C.8. The first and last term in equation C.22 can be computed directly, which together results in:

$$-k_p^2\tilde{\phi}^{H_0} = \partial_z^2\tilde{\phi}^{H_0} - k_r^2\tilde{\phi}^{H_0} \tag{C.24}$$

Rearranging we notices this wave equation has the same form as the 2D derived wave equation

$$\partial_z^2\tilde{\phi}^{H_0} - (k_r^2 - k_p^2)\tilde{\phi}^{H_0} = 0$$

$$\partial_z^2\tilde{\phi}^{H_0} - q_p^2\tilde{\phi}^{H_0} = 0 \tag{C.25}$$

Since the derivations are a bit repetitive, or simply because the author cannot demonstrate the last one without further struggling, then it will just be given that when first order Hankel transformation is used the final equation becomes:

$$\partial_z^2 \tilde{\psi}^{H_1} - (k_r^2 - k_s^2)\tilde{\psi}^{H_1} = 0$$

$$\partial_z^2 \tilde{\psi}^{H_1} - q_s^2 \tilde{\psi}^{H_1} = 0 \tag{C.26}$$

Bibliography

[1] J.D. Achenbach. *Wave Propagation in Elastic Solids*. Applied Mathematics and Mechanics vol.16. Ed. by H.A. Lauwerier and W.T. Koiter. North-Holland Publishing Company, 1973. Chap. 7. ISBN: 9780720403251.

[2] Michael Armstrong. "Seismic Inversion for Identification of Near-Surface Soil Properties for Offshore Wind Turbines - Preparation Project". Dec. 2015.

[3] S.A. Badsar et al. "Determination of the material damping ratio in the soil from SASW tests using the half-power bandwidth method". In: *Geophysical Journal International* 182.3 (2010), pp. 1493–1508.

[4] Ingmar Bolderink. "Identification of dynamic soil properties relevant for offshore wind turbines through full waveform inversion of in situ measured seismic data". MSc Thesis Report. TU Delft, Seimens, Sept. 2015.

[5] J.H.A Bosch. *Formatie van Appelscha*. DINOloket. 2003. URL: https://www.dinoloket.nl/formatie-van-appelscha.

[6] José M Carcione, Dan Kosloff, and Ronnie Kosloff. "Wave propagation simulation in a linear viscoelastic medium". In: *Geophysical Journal International* 95.3 (1988), pp. 597–611.

[7] *Cost Reduction options for Offshore wind in the Netherlands FID 2010-2020*. Tech. rep. TKI Wind Op Zee, 2015. URL: http://tki-windopzee.eu/nieuwsbericht/target-cost-reduction-for-offshore-wind-energy-of-40-is-within-reach.

[8] Karel N. van Dalen. *Lecture Notes CIE5340 Soil Dynamics, part B: Body waves in an elastic continuum and Rayleigh waves at the free surface*. June 2015. 2015.

[9] Karel N van Dalen. *Multi-component acoustic characterization of porous media*. Springer Science & Business Media, 2013.

[10] Sebastiano Foti et al. *Surface Wave Methods for Near Surface Site Characterization*. CRC Press, 2015.

[11] Eduardo Kausel. "Number and location of zero-group-velocity modes". In: *The Journal of the Acoustical Society of America* 131.5 (2012), pp. 3601–3610.

[12] Luc Knockaert. "Fast Hankel transform by fast sine and cosine transforms: the Mellin connection". In: *IEEE Transactions on Signal processing* 48.6 (2000), pp. 1695–1701.

[13] Steve L. Kramer. *Geotechnical Earthquake Engineering*. Prentice-Hall, Inc, 1996. Chap. 6. ISBN: 0-13-374943-6.

[14] Carlo G Lai and Glenn J Rix. "Solution of the Rayleigh eigenproblem in viscoelastic media". In: *Bulletin of the Seismological Society of America* 92.6 (2002), pp. 2297–2309.

[15] Carlo G Lai and Krzysztof Wilmanski. *Surface waves in geomechanics: Direct and inverse modelling for soils and rocks*. Vol. 481. Springer Science & Business Media, 2007, pp. 178–179.

[16] Adam Lichtl and Stephen Jones. "Full Scale Simulation of SpaceX's Mars Rocket Engine". Presentation. 16:00-21:00 min. 2015. URL: http://on-demand.gputechconf.com/gtc/2015/video/S5398.html.

[17] Margherita Maraschini et al. "A new misfit function for multimodal inversion of surface waves". In: *Geophysics* 75.4 (2010), G31–G43.

[18] Amr S Misbah and Claudio L Strobbia. "Joint estimation of modal attenuation and velocity from multichannel surface wave data". In: *Geophysics* 79.3 (2014), EN25–EN38.

[19] Steinar Nordal. *Lecture Notes PHD Course at NTNU BA8305 Geodynamics*. August 2015.

[20] MIT OpenCourseWare, ed. *Basic Relationships in Elasticity Theory*. 2006. URL: http://ocw.mit.edu/courses/nuclear-engineering/22-314j-structural-mechanics-in-nuclear-power-technology-fall-2006/readings/elsticty_thry.pdf.

[21] Pabloruiz. *Surface stresses 3*. Licensed under Public Domain via Wikiversity. URL: https://en.wikiversity.org/wiki/File:Surface_stresses_3.png#/media/File:Surface_stresses_3.png.

[22] M. Costa Ros. "Managing Risk and Standardization". EWEA 2015 Paris Conference. Nov. 2015.

[23] Berry Schoenmaker. *Personal Communication*. Fugro, May 11, 2016.

[24] Jonathan Richard Shewchuk. *An introduction to the conjugate gradient method without the agonizing pain*. 1994.

[25] Valentina L Socco et al. "On the use of the Norwegian Geotechnical Institute's prototype seabed-coupled shear wave vibrator for shallow soil characterization-II. Joint inversion of multimodal Love and Scholte surface waves". In: *Geophysical Journal International* 185.1 (2011), pp. 237–252.

[26] Massachusetts Institute of Technology Department of Mechanical Engineering. "Sampling and the Discrete Fourier Transform". In: *MIT OpenCourseWare* (2008).

[27] Daniel Trad, Tadeusz Ulrych, and Mauricio Sacchi. "Latest views of the sparse Radon transform". In: *Geophysics* 68.1 (2003), pp. 386–399.

[28] San Diego University of California, ed. *Bessel Functions*. URL: `http://flyingv.ucsd.edu/krstic/teaching/287/bess.pdf`.

[29] Maarten Vanneste et al. "On the use of the Norwegian Geotechnical Institute's prototype seabed-coupled shear wave vibrator for shallow soil characterization–I. Acquisition and processing of multimodal surface waves". In: *Geophysical Journal International* 185.1 (2011), pp. 221–236.

[30] W. G Versteijlen et al. "Assessing the small-strain soil stiffness for offshore wind turbines based on in situ seismic measurements". In: *Journal of Physics: Conference Series*. Vol. 524. 1. 9th International Conference on Structural Dynamics. IOP Publishing. 2014, p. 012088.

[31] W.G. Versteijlen, A.V. Metrikine, and K.N. van Dalen. "A method for identification of an effective Winkler foundation for large-diameter offshore wind turbine support structures based on in-situ measured small-strain soil response and 3D modelling". In: *Engineering Structures* 124 (2016), pp. 221–236.

[32] Wikipedia. *Aliasing*. URL: `https://en.wikipedia.org/wiki/Aliasing`.

[33] Wikipedia. *Spectral Leakage*. URL: `https://en.wikipedia.org/wiki/Spectral_leakage`.

[34] Corine de Winter. "Inversion of near surface seismic measurements to estimate soil stiffness relevant for offshore wind turbines". MSc Thesis Report. TU Delft, Seimens, Oct. 2014.

[35] Wolfram. *Cylindrical Coordinates*. URL: `http://mathworld.wolfram.com/CylindricalCoordinates.html`.

TU Delft Delft University of Technology

SIEMENS

NTNU